UNIVERSIDADE FEDERAL DO RIO GRANDE DO SUL
GRADUATE PROGRAM IN PHYSICS
PhD THESIS

Murilo Sodré Marques

Molecular Modeling of Fluids: Colloids, Water, Alcohols and their Mixtures [1]

Modelagem Molecular de Fluidos: Colóides, Água, Álcoois e suas Misturas

Porto Alegre

2021

---

[1] Project sponsored by two brazilian agencies: Conselho Nacional de Desenvolvimento Científico e Tecnológico (CNPq) and Coordenação de Aperfeiçoamento de Pessoal de Nível Superior (CAPES).

Murilo Sodré Marques

Molecular Modeling of Fluids: Colloids, Water, Alcohols and their Mixtures

Thesis submitted to the Universidade Federal do Rio Grande do Sul in partial fulfillment of the requirements for the degree of Doctor in Sciences under the supervision of Profa. Dra. Marcia C. B. Barbosa (Institute of Physics - UFRGS) and co-supervision of Prof. Dr. José R. Bordin (Department of Physics - UFPel).

Porto Alegre

2021

Abstract

Core-softened fluids comprise a large number of systems whose molecular constituents have competitive interactions. The most prominent example is water whose molecules tend to form hydrogen bonds. The competition between these two conformations leads to a series of anomalous behaviors which can manifest themselves both in colloids and in mixtures of water and short-chain alcohols. The successful description of colloidal systems by two-length-scale potentials is related to the composition of these systems, usually made up of molecular subunits forming a compact central agglomeration and a less dense peripheral area with a prevalence of entropic effects. This core-corona structure can be described by a hard core and a soft corona that well represents the competition between enthalpy and entropic effects. Alcohol molecules bring even more competition to this complex scenario, since the majority do not have spherical symmetry, therefore incorporating anisotropic effects, and because they carry, in addition to the nonpolar carbonic part, hydrophilic hydroxyl groups, capable of forming hydrogen bonds, giving them a high degree of miscibility with water.

This thesis focuses on the intricate molecular mechanisms that underlie the behavior of these complex fluids. To this end, we perfom large-scale Molecular Dynamics simulations of distinct systems. First, we analyzed the behavior of a two-dimensional system of polymer-grafted nanoparticles. Effective core-softened potentials were obtained from coarse-grained simulations for two cases: one in which the polymers are free to rotate around the nanoparticle core and a second in which the polymers are fixed, with a 90° angle between them. Due to the competition in the system we observe waterlike anomalies, such as the temperature of maximum density (TMD) and the diffusion anomaly. We observe that for the fixed polymers case the waterlike anomalies originate in the competition between the characteristic length scales in the potential, while for the freely rotating case, the anomalies arise due to a smaller region of stability in the phase diagram, with no competition between scales. Subsequently, we propose a two-site model of tert-butanol in which the interactions involving hydrogen bonding are represented by a Stillinger-Weber potential. The potential model is optimized to yield a reasonable description of experimental excess enthalpies and volumes over the whole composition range of the mixture. This model is able to reproduce the maximum in the change of the temperature of maximum density for very low alcohol mole fractions, followed by a considerable decrease until the density anomaly itself disappears. We have correlated this behavior with changes in the local structure of water and compared it with the results of all-atom simulations of water/tert-butanol mixtures. The third studied system was a core-softened representation of water-alcohol mixtures. This approach allowed us to explore the connection between the spontaneous crystallization observed in the supercooled regime in the vicinity of the liquid-liquid phase transition (LLPT), and the density anomaly by performing extensive Molecular Dynamics simulations of a model mixture of core-softened water and methanol. Our results illustrate the relation between the vanishing of the density anomaly and an increase in the temperature of spontaneous crystallization. This peculiar feature illustrates how fine-tuning the competitive interactions determines the anomalous behavior of water/alcohol mixtures. Finally, we explored the supercooled regime of pure water and mixtures of water and short-chain alcohols (methanol, ethanol and propanol) using core-softened potential models. Our aim is to understand the influence of chain size on the density anomaly, the liquid-liquid phase transition and on the polymorphism observed in these models.

Keywords: Polymer-Grafted Nanoparticles. Phase Diagram. Thermodynamic Anomalies. Molecular Dynamics. Water.

Resumo

Fluidos modelados por potenciais de caroço amolecido compreendem um grande número de sistemas cujos constituintes moleculares têm interações competitivas. O exemplo mais proeminente é a água, cujas moléculas tendem a formar ligações de hidrogênio ou interagir por ligações covalentes. A competição entre essas duas conformações leva a uma série de comportamentos anômalos os quais podem se manifestar tanto em colóides quanto em misturas de água e álcoois de cadeia curta. A descrição bem sucedida de sistemas coloidas por potenciais de duas escalas está relacionada à composição de tais colóides, geralmente feitos de subunidades moleculares formando uma aglomeração central compactada e uma área periférica, menos densa e mais entrópica. Esta estrutura núcleo-coroa pode ser descrita por um núcleo duro e uma coroa macia que representa bem a competição entre efeitos entálpicos e entrópicos. As moléculas de álcoois trazem ainda mais competição para esse cenário complexo, já que a maioria não possui simetria esférica, incorporando, portanto, efeitos anisotrópicos aos sistemas, e são portadores, além da parte carbônica apolar, de grupos hidroxila hidrofílicos, capazes de formar ligações de hidrogênio, o que lhes confere um alto grau de miscibilidade em água. Esta tese foca nos mecanismos moleculares que descrevem o comportamento destes fluidos complexos. Para tanto, realizamos simulações de Dinâmica Molecular de quatro sistemas distintos. Primeiramente, analisamos o comportamento do sistema bidimensional de nanopartículas enxertadas com polímeros, onde potenciais atenuados de núcleo efetivos foram obtidos a partir de simulações de *coarse-grained* para dois casos: o primeiro caso onde os polímeros são livres para girar em torno do núcleo da nanopartícula, e um segundo onde os polímeros são fixos, com um ângulo de 90° entre eles. Devido à competição no sistema, observamos a presença de anomalias semelhantes às da água, como a temperatura de máxima densidade (TMD) e a anomalia na difusão. Observamos que, para o caso dos polímeros fixos, as anomalias do tipo água são originadas pela competição entre as escalas características potenciais, enquanto para o caso livre para girar as anomalias surgem devido a uma menor região de estabilidade no diagrama de fase sem competição entre as escalas. Depois, foi proposto um modelo de terc-butanol de dois sítios, no qual as interações envolvendo ligações de hidrogênio são representadas por um potencial de três corpos (Stillinger-Weber). O modelo foi otimizado para produzir uma descrição razoável da grandezas de excesso (entalpia e volume) experimentais em toda a faixa de composição da mistura, sendo capaz de reproduzir a presença de um máximo na variação da temperatura de máxima densidade no regime super diluído (frações molares de terbutanol muito baixas), seguido por uma diminuição considerável até o desaparecimento da TMD. Correlacionamos esse comportamento com mudanças na estrutura local da água e comparamos com os resultados de simulações *all-atom* de misturas de água/terc-butanol. O terceiro sistema estudado foi uma mistura de água e álcool na qual as interações entre ambas as moléculas foram representadas por potenciais de caroço atenuado. A abordagem nos permitiu explorar a conexão entre a cristalização espontânea, observada no regime super-resfriado na vizinhança da transição de fase líquido-líquido (LLPT), e a anomalia na densidade, realizando extensas simulações de Dinâmica Molecular. Nossos resultados ilustram a relação entre o desaparecimento da anomalia de densidade e um aumento na temperatura de cristalização espontânea. Esta característica peculiar ilustra como o ajuste fino das interações competitivas determinam o comportamento anômalo das misturas de água e metanol. Por fim, exploramos o regime super-resfriado de água pura e misturas de água e álcoois de cadeia curta (metanol, etanol e propanol) usando modelos de potenciais de duas escalas. Nosso objetivo foi compreender a influência do tamanho da cadeia carbônica na anomalia de densidade, na transição de fase líquido-líquido e no polimorfismo observado nestes modelos.

Palavras-chave: Nanopartículas Enxertadas com Polímeros. Diagramas de Fase. Anomalias Termodinâmicas. Dinâmica Molecular. Água.

Publications and submissions

This work is based on the following publications and preprints which are reprinted in Appendix.

Waterlike anomalies in hard core-soft shell nanoparticles using a effective potential approach: pinned vs adsorbed polymers
Murilo S. Marques, Thiago P. O. Nogueira, Márcia C. Barbosa and J. R. Bordin
Journal of Applied Physics 127(5):054701, DOI: 10.1063/1.5128938

Competing interactions near the liquid-liquid phase transition of core-softened water/methanol mixtures
Murilo S. Marques, Vinícuis F. Hernandes, E. Lomba and J. R. Bordin
Journal of Molecular Liquids Volume 320, Part B, 15 December 2020, 114420
DOI: 10.1016/j.molliq.2020.114420

Modeling the temperature of maximum density of aqueous tert-butanol solutions
Murilo S. Marques, E. Lomba, Eva G. Noya, D. González-Salgado and Marcia Barbosa
arXiv:2008.02306

Core-softened water-alcohol mixtures: the solute-size effects
Murilo S. Marques, Vinícuis F. Hernandes and J. R. Bordin
arXiv:2102.09485

Contents

Chapter 1

The Modeling of Fluids: from Newton to computers

1.1 Historical Overview

The birth of the intermolecular force law

The problem of understanding the forces that hold matter together was first tackled seriously by Isaac Newton [1]. He extended the idea of "action at a distance" from planets to atoms, and joined for the first time the concepts of force and atom into a single hypothesis. Newton began by looking at the physical evidence, such as the cohesion of solids, surface tension and viscosity, which led him to conclude that a strong attraction must exist among atoms.

In 1758, Boscovich published Philosophiae Naturalis Theoria [2], which can be considered the cornerstone of modern theories of atomic forces. The primary elements of matter were for Boscovich indivisible, non-extended points. In contrast with Newton's hypothesis, direct contact of these points is not allowed because for impenetrable particles this would imply a discontinous change in velocity at the moment of contact. Thus particles actually never meet: at very short distances the mutual force between them is repulsive, and increases indefinitely as the distance is diminished. At great distances, particles attract through the gravitational force.

Over the intermediate range the force is alternatively attractive and repulsive, with one or more oscillations. Boscovich represented his theory graphically through a force–distance curve: forces above the horizontal axis are repulsive, those below it are attractive (Fig. 1-1). Although Boscovich's theory was entirely qualitative, it did include some modern concepts of intermolecular interactions, such as the infinite repulsion between molecules at very short distances, and it invoked the necessary interplay between attractive and repulsive forces to explain the properties of matter. His law of interaction can be considered as the first interatomic model [3].

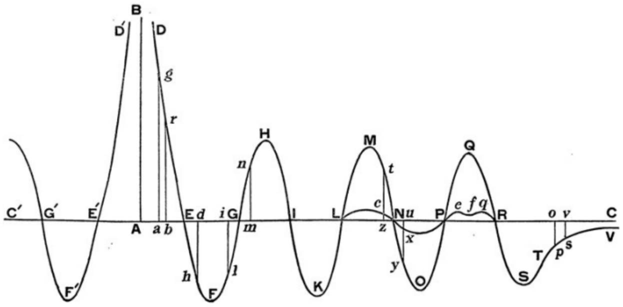

Figure 1-1: Boscovich force–distance curve from the dissertation *De viribus vivis*, published in 1745 [2].

About 50 years later, Giuseppe Belli, professor of physics at Pavia, considered in detail the problem of molecular attraction. In a paper published in 1814, Belli [4] analysed known experimental facts to conclude that molecular attraction is not equivalent to gravitational attraction and its intensity is proportional to $1/r^n$,where r is the particle distance, with n lying between 4 and 6.

The dawn of the 19th century brought new ways of observing phenomena at the molecular level [5].The work of crystallographers and chemists elucidated the arrangement of atoms within matter and laid the foundation of our present knowledge.This story, familiar to every physicist, was written by Maxwell [6], Van der Waals [7], Reinganum [8], Debye [9] and, finally, London [10, 11], who developed a rigorous quantum mechanical description of intermolecular forces. These forces result from electromagnetic interactions between the electrons and nuclei forming the molecules, and thus their calculation requires solving the Schrödinger equation for a system of interacting particles [5].

Liquid Theory in the 20th century

The study of the liquid state of matter has a rich history, from both the theoretical and experimental standpoints, and the application of statistical mechanics to the study of fluids over the past ninety years or more has progressed through a series of problems of gradually increasing difficulty. From early observations of Brownian motion to recent neutron-scattering experiments, experimentalists have worked to improve the understanding of the structure and particle dynamics that characterize liquids. At the same time, theoreticians have tried to construct simple models which explain how liquids behave [12]. The first and most elementary calculations were for the thermodynamic functions (heat capacities, entropies, free energies, etc) of ideal gases [13]. Having sucessfully treated the perfect gas, it was natural to consider gases of moderate density, where intermolecular force begin to have an effect, by expanding the thermodynamic functions in a power series (or virial series) in density. Although the mathematical basis for a theoretical treatment of this series was laid by Ursell in 1927 [14], it was not exploited until ten years later, when Mayer re-examined the problem [15]. Since that time a great deal of effort has been put into evaluating the virial coefficients that appear in the series for a variety of intermolecular force models.

While the theory of dillute gases at equilibrium is essentially complete , this is far from being the case for all dense gases and liquids. The virial series cannot be applied directly to liquids [16]. Early models of liquids [17] involved the physical manipulation and analysis of the packing of a large number of gelatine balls, representing the molecules; this resulted in a surprisingly good three-dimensional picture of the structure of a liquid, or perhaps a random glass, and later applications of the technique have been described [18]. Alternative approachs include analytical methods, as:

- Integral equation methods (initiated by Kirkwood and Yvon in the 1930s) [19]: one starts by writing down an exact equation for the molecular distribution function of interest, usually the pair function, and then introduces one or more approximations to describe a solution. These approximations are often motivated by considerations of mathematical simplicity, so that their validity depends on a posterior agreement with computer simulation or experiment.

- Thermodynamic perturbation theories (in early 1950s until late 1960s) [20]: the properties of the fluid of interest, in wich the intermolecular potential energy is U say, are related to those for a reference fluid with potential U_0 through a suitable expansion. One attempts to choose a reference system that is some sense close to the real system, and whose properties are well known (e.g. through computer simulation studies or an integral equation theory).

and numerical methods, computational simulation studies that we will discuss next.

1.2 Properties of liquids

At low pressures, matter usually exists either as a dense solid or as a dilute vapour. For each of these states there is an ideal model which is a good approximation to reality and forms the basis for theoretical discussion. These are the ideal crystal lattice and the ideal gas models, respectively: in the former, emphasis is on structural order modified slightly by the thermal motion of the atoms while the latter model describes the thermal motion of the atoms on the basis of random atomic positions and motions [21]. At higher pressures a third state of matter appears - the liquid state. This state occurs over a temperature range that separates the regions occupied by the solid and vapour states. At present there is no ideal model which gives a good approximation to the liquid state. If such a model is found it would (in contrast to the crystal and gas models) need to cover structural and thermal properties with equal emphasis [22].

The microscopic description of the liquid is formulated here by treating the individual microscopic units in terms of the laws of classical physics. The justification of the classical approximation depends on the value of the thermal de Broglie wavelength ($\Lambda_0 = h/\sqrt{2\pi m k_B T}$) corresponding to the average momentum of the liquid particles (of mass m) at a temperature T, where $h = 6.63 \times 10^{-34}\ J.s$ is the Planck constant and $k_B = 1.38 \times 10^{-23}\ J.K^{-1}$ is the Boltzmann constant, such that $k_B T = 1/\beta$ is the thermal energy. If the mean nearest-neighbor separation of the liquid particles ${a \simeq \rho_0}^{-1/3}$ is such that $\Lambda_0/a \ll 1$, then the classical description is justified [23]. Some results for a variety of atomic and simple molecular liquids are shown in Table 1.1; hydrogen and neon apart, quantum effects should be small for all the systems listed. In the case of time-dependent processes it is necessary in addition that the time scale involved be much longer than $\beta\hbar$, where $\hbar = h/(2\pi)$, which at room temperature, for example, means for times $t \ll 10^{-14}s$. This second condition is somewhat more restrictive than the first, but where translational motion is concerned the problem is again severe only in extreme cases such as hydrogen [24].

Liquid	$\mathbf{T_t}(K)$	$\mathbf{\Lambda}$(Å)	$\mathbf{\Lambda/a}$
$\mathbf{H_2}$	14.1	3.3	0.97
Ne	24.5	0.78	0.26
$\mathbf{CH_4}$	91	0.46	0.12
$\mathbf{N_2}$	63	0.42	0.11
Li	454	0.31	0.11
Ar	84	0.30	0.083
HCl	159	0.23	0.063
Na	371	0.19	0.054
Kr	116	0.18	0.046
$\mathbf{CCl_4}$	250	0.9	0.017

Table 1.1: Test of the classical hypothesis [24]. $a = \rho^{-1/3}$.

.

In the classical approximation the contributions to the thermodynamic properties from the kinetic and interaction parts of the Hamiltonian can be obtained separately. If R_e represents the absolute value of the ratio of the kinetic and potential parts of the total energy of the system of particles, then $R_e \sim 1$ corresponds to the liquid state. On the other hand, for the gaseous and solid states we have $R_e \gg 1$ and $R_e \ll 1$, respectively. The liquid state thus represents an intermediate between two extremes. Indeed, the intermediate nature of the liquid state makes it particularly difficult to develop a quantitatively accurate model for its thermodynamic or dynamic properties at high densities. Both for dilute gases and for low-density solids the corresponding idealized model, namely the perfect gas and the harmonic solid, can be treated exactly. Such a reference state is lacking for a high-density liquid [23].

At ambient temperatures, the solid states of matter are generally associated with the mineral world, while 'soft' matter, and in particular the liquid state, are more intimately related to life sciences. In fact it is generally accepted that life took its origin in the primordial oceans, thus underlining the importance of a full quantitative understanding of liquids. The distinction between the spatial arrangements of molecules in gases, liquids and solids is illustrated very schematically in figure 1-2. It shows 'snapshots' of typical configurations of disc-like molecules in two-dimensional counterparts of the three phases. A quantitative measure of the local order on the molecular scale is provided by the radial (or pair) distribution function $g(r)$, which characterizes the modulation of the local density $\rho(r)$ around a given molecule, as a function of the distance r from that molecule. For more complex substances, generally made up of highly anisotropic molecules or of flexible macromolecules, the liquid state itself exhibits a rich variety of structures and phases, often referred to as complex fluids [25].

It's also possible to conceptualize a liquid as a very disordered solid. The structure of a liquid is governed by the statistical distribution of the centers of gravity of the atoms or molecules. Of course the latter keep moving, but we can ask about the atomic distributions if one could perform a snapshot of the atomic arrangements. The average statistics of such snapshots is what we call the (static) structure of the liquid [26]. Theories of the liquid state based on an approach involving disordered solids were pursued from the 1930s to the 1960s but did not meet with much success. On the other hand, the liquid may be regarded as an extremely imperfect gas. In this approach, which has been quite successful, the statistical mechanical techniques used to describe the properties of non-ideal gases are extended to liquids [27].

So we know that the liquid state is much more complex than either the gaseous or solid states. In view of the characteristics of the liquid state - the strong interaction of

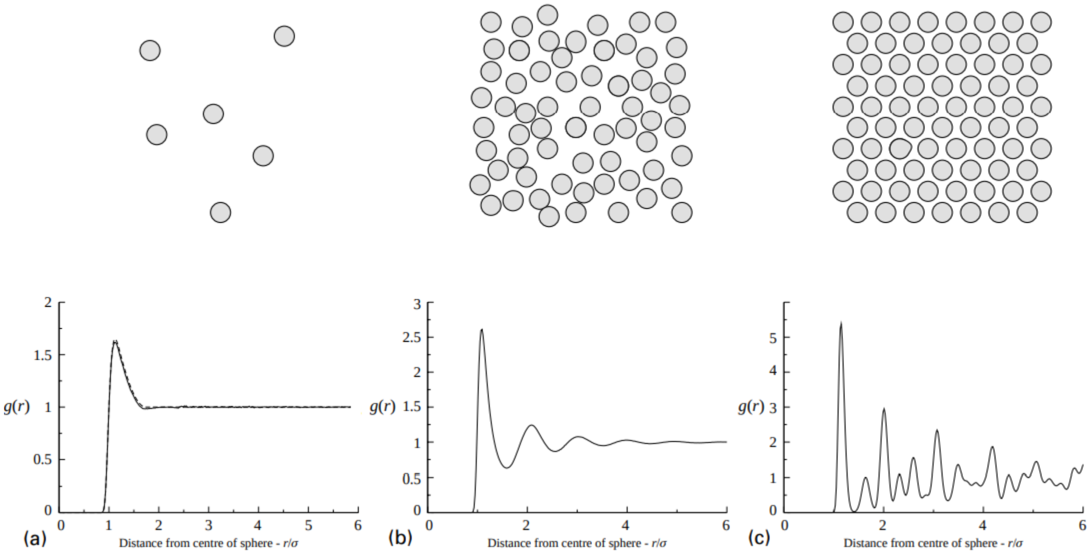

Figure 1-2: top:typical atomic configurations in a gas(left), liquid (middle) and crystalline solid (right). Bottom: Typical pair distribution functions for (a) a gas, (b) a liquid and (c) a solid [25].

particles and their state of great disorder - which greatly complicate the theoretical analysis of the problem, it can be said that liquids represent the state of matter most frequently studied by computational simulation methods [28], among which Molecular Dynamics (the thechnique employed in this work), which are aimed to generate the system's trajectory in phase space, i.e. the time evaluation (by use of finite-difference methods) of the positions and momenta of the particles. Thereby, the thermodynamical properties of the system are determined at regular time intervals, so that their time averages can be estimated according to the ergodic hypothesis [29]: If $A(q,p)$ is any observable of the system, e.g., the total energy $H(q,p)$ or the angular momentum $L(q,p)$, the time average $\overline{A(q,p)}$ and the ensemble average $\langle A(q,p)\rangle$ for a closed system at a giver energy would certaintly be identical if during its time evolution the phase-space trajectory passed through each point of the energy surface an equal number of times (e.g., once - sufficient condition) [30].

1.3 Computational Modeling

Computer simulations of many-body systems have nearly as long history as modern computers. They are by now an established tool in many branches of science, and has as its focus predicting macroscopic properties on the basis of fundamental interactions between the constituent particles of the system. One of the main motivations for computer simulations of physical systems is that one eliminates approximations usually made when we treat the problem analytically (for example, a mean-field-type) [31]. It's notorious that the thermodynamic properties of a many-particle system in equilibrium can be found as an ensemble average. Nevertheless, experimental systems are so large that it is impossible to determine this ensemble average by summing over all the accessible states in a computer. There are many methods for determining these physical quantities as statistical averages over a restricted set of states, among which the most known are Molecular Dynamics (deterministic) and Monte Carlo (stochastic) methods [32]. These various methods can be arranged, as in figure 1-3, according to the degree of determinism used in generating molecular positions [33].

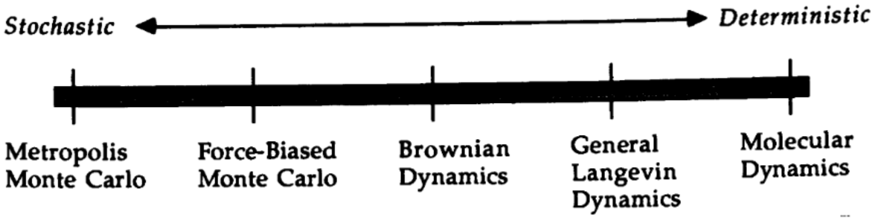

Figure 1-3: Relative degree of determinism in various molecular simulation methods [33].

Imagine that we have a random sample of, for example, 10^7 system configurations which are all compatible with the values of the system parameters. For such a large number we expect averages of physical quantities over the sample to be rather close to the real ensemble average. It is unfortunately impossible to generate such a random sample; however, we can generate a sample consisting of a large number of configurations which are determined successively from each other and are hence correlated. This is done in the Molecular Dynamics and Monte Carlo methods. With a computer simulation we can study systems not yet tractable with analytical methods, although they seem to have two drawbacks [34]:

- The description of the interaction between a large number of particles as a sum of pair potentials neglects many-body interactions;
- The description of pair potentials in a simplified way is computationally necessary and conceptually desirable, but it represents an approximation. The accuracy of the approximation can be judged by the results.

In the early 1950s, scientists at Los Alamos National Laboratories in the United States built an electronic digital computer, called MANIAC I (Mathematical Analyzer, Numerator, Integrator, and Computer), which was very similar to the first computer, ENIAC. Many important numerical studies, including Monte Carlo simulation of classical liquids (the first computer simulation of a liquid) [35], were performed on MANIAC I, which was at that time one of the most powerful computing machine available in the world. All these research-intensive activities accomplished in the 1950s showed that computation was no longer just a supporting tool for scientific research but rather an actual means of probing scientific problems and predicting new scientific phenomena. A new branch of science, *computational science*, was born [36]. It is a measure of the continuing rapid advance in computer technology that handheld devices of comparable power are now available to all at modest cost. Rapid development of computer hardware means that computing power continues to increase at an astonishing rate. Using modern parallel computer architectures, we can enjoy exaflop computing nowadays (an exaflop is 10^{18} floating-point operations per second). This is matched by the enormous increases in data storage available to researchers and the general public [12]. It is quite possible that computer development will prove to be one of humanity's greatest technological achievements. The computer may still be next to the use of fire, the discovery of the wheel and the harnessing of electricity. These earlier advances exploited basic forces: the computer exploits its own intelligence [37].

Along with the rapid development in the computer technology, the molecular computer simulations and,particularly, the classical Molecular Dynamics (MD) methods, treating the atoms and the molecules as classical particles, have developed in the last decades to an important discipline to obtain information about thermodynamics, structure and dynamical properties in condensed matter from pure simple liquids to studies of complex biomolecular systems in solution [31, 38]. Most of the early MD studies were directed at the problem of liquid structure, as is the content of major part of this thesis. Therefore, MD is the technique that will be described in more depth.

Molecular Dynamics

Molecular Dynamics simulation is a technique to computing the equilibrium and transport properties of classical many-body systems. In this context, the word classical means that the motion of the constituent particles obeys the laws of classical mechanics. This is an excellent approximation for a wide range of materials, but has its limitations – as all theoretical approaches. When we consider the translational or rotational motion of light atoms or molecules (He, H_2, D_2) or vibrational motion with a frequency ν such that $h\nu > k_B T$ we should worry about quantum effects and use quantum mechanical based methods [39].

Under the influence of a continuous potential (as is the case in all topics covered by this thesis), the motion of all particles are coupled, giving rise to a many-body problem that cannot be solved analytically. Under such circunstances, the equations of movement are integrated using a finite difference method where the integration is broken down into many small stages, each one separated in time by a fixed time step δt, and the total force on each particle in the configuration at the time t is calculated as the vector sum of its interactions with other particles. From the force we can determine the acelerations of the particles, which are then combined with the positions and velocities at the time t to get the positions and velocities at a time $t + \delta t$. The force is assumed to be constant during the time step as $\delta t \to 0$. The forces on the particles in their new positions are then determined, leading to new positions and velocities at time $t + 2\delta t$, and so on [40]. The integration method used here was the Velocity-Verlet algorithm, probably the most widely used finite-difference method today by two reasons which are crucial for the long-time stability of numerical solvers[41]: (i) time-reversibility (a fundamental symmetry of Hamilton's equations), and (ii) the symplectic property (a corollary of this is Liouville's theorem, which states that on a Hamiltonian system, the phase-space volume of a closed surface is preserved under time evolution), and whose scheme is illustrated in Fig. 1-4.

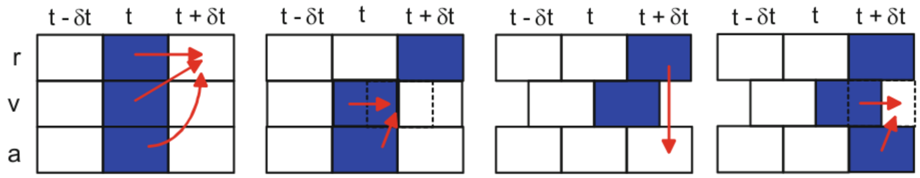

Figure 1-4: Illustration of the Velocity Verlet algorithm [29]: current positions $\mathbf{r_i(t)}$, velocities $\mathbf{v_i(t)}$ and accelerations $\mathbf{a_i(t)}$ are used to estimate the new positions $\mathbf{r_i(t + \delta t)}$; the $\mathbf{v_i(t)}$ and $\mathbf{a_i(t)}$ values are then also used to forward the velocities to $\mathbf{v_i(t + 1/2\delta t)}$. Accelerations $\mathbf{a_i(t + \delta t)}$ are derived in the new positions $\mathbf{r_i(t + \delta t)}$, which then together with the $\mathbf{v_i(t + 1/2\delta t)}$ give the new velocities $\mathbf{v_i(t + \delta t)}$.

In many aspects, Molecular Dynamics simulations are similar to real experiments. When we perform a real experiment, we proceed as follows. We prepare a sample of the material that we wish to study. We connect this sample to a measuring instrument (e.g., a thermometer, manometer, or viscosimeter), and then we measure the property of interest during a certain time interval. If our measurements are subject to statistical noise (as most measurements are), then the longer we average, the more accurate our measurement becomes. In a Molecular Dynamics simulation, we follow the same approach. First, we prepare a sample: we select a model system consisting of N particles and we solve Newton's equations of motion for this system until the properties of the system no longer change with time (we equilibrate the system). After equilibration, we perform the actual measurement [39].

Newton's equations of motion lead naturally to the microcanonical (NVE) ensemble since energy is conserved. Extending Molecular Dynamics to the other ensembles requires some artificial tampering with the equations of motion. A canonical (NVT) ensemble can be obtained by either using velocity scaling or explicity adapting the equations of motion [42, 43] - the called thermostats. Andersen (1980) formulated an isobaric-isoenthalpic (NPH) and isobaric-isothermic (NPT) Molecular Dynamics algorithms by introducing additional degrees of fredom which are coupled to the particle coordinates [44]. This work has been extended rigorously leading to many thermostats and barostats.

1.4 Multi-scale Methods

The term multiscale modeling is widely used to describe a hierarchy of simulation approaches to treat systems across different scales. For a given scale of interest, one picks a simulation method capable of simulating systems at the length and time scales of interest. A common way of viewing this approach is a multiscale diagram, as depicted in the figure 1-5. When one moves to larger scales, a coarse-grained model is required to enable simulations. One challenge and ongoing area of research is linking simulations of detailed models with simulations of coarse-grained ones, such that the behavior of the system can be resolved at multiple scales and the interactions at different scales inform each other [45]. There are two ways that this information can be propagated:

- **bottom-up** – fundamental physical principles at the more detailed scale are used to parametrize a model at a coarse-grained scale. One example is when atomistic simulations are used to calculate fluid transport coefficients that can then be used in continuum simulations of the fluid transport equations (e.g., fluid dynamics, diffusion);

- **top-down** – the behavior at larger scales is used to inform the interactions at more detailed scales. An example might be that bulk, continuum electrostatic calculations on a large system could be used to parameterize the electric field in atomistic simulations. Or, input from experiments- such as molecular structures - could guide the development of molecular models.

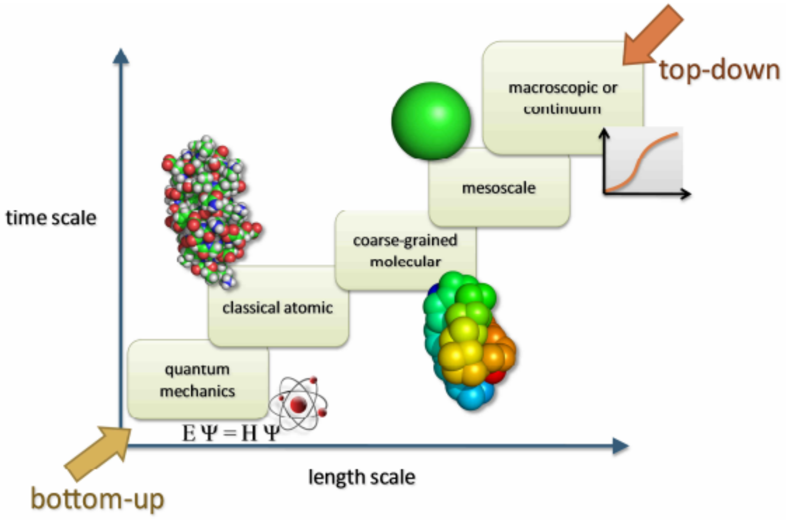

Figure 1-5: different simulations aproaches. Extracted from Ref.[45].

1.5 Coarse-graining techniques

For polymers, this "multiscale problem" is particularly severe, since a single flexible macromolecule already exhibits structure on many length scales (Fig. 1-6), and is a slowly relaxing object [46, 47]. In addition, one often wishes to consider systems with multiple constituents (concentrated polymer solutions or blends, mixtures of homopolymers and block copolymers or polymers of different architecture) which exist in several phases, and then the scales of length and time that are of physical interest truly extend from the subatomic scale (relevant for the electronic structure of polymers, their chemical reactions, excited states, etc.) to the macroscopic scale (e.g., phase separated domains of the scale of micrometers or larger, glassy relaxation on the scale of seconds or hours, etc.) [48, 49].

Since there is no hope of treating all these scales equally well in a single type of computer simulation, the idea of "coarse-graining" has emerged [50, 51]. It has been shown that by simplifying the molecular description, thus reducing the degrees of freedom, MD simulations are able to afford a considerable computational speed-up, opening the way to extended simulation studies in time and lengthscales never covered before [52–55]. This computational speed-up is a consequence of the many effects of the coarse- graining (CG) procedure on the potential, which are complex and some-

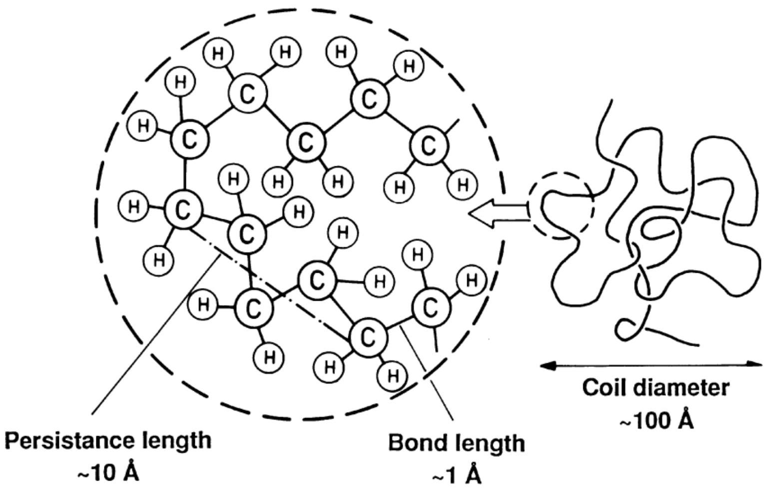

Figure 1-6: Schematic illustration of the various length scales of a macromolecule. Polyethylene is used as an example. Extracted from Ref. [46].

times competing [56]. By eliminating (or, more formally, integrating out) atomistic details that are considered "unnecessary", these models may provide three or more orders of magnitude greater efficiency than atomically detailed models [57]. Because human imagination and computational demands both significantly out-pace Moore's law, the popularity of CG models continues to grow rapidly, despite tremendous recent advances in simulation methods, atomically detailed models, and computational resources [58].

When constructing a particle-based model for a specific system, one must first define the particles that are used to represent the system. In the case of an atomically detailed model, these particles simply correspond to the atoms in the system. In contrast, the particles in a CG model, which we shall refer to as sites, correspond to groups of one or more atoms (fig. 1-7). We shall refer to the procedure for transforming an atomically detailed structure into a CG representation of the same structure as the “CG mapping.” Clearly, one may tailor the mapping to precisely capture the key features of a specific system or phenomenon of interest, while simultaneously eliminating atomic details that are considered “unimportant.” This flexibility in designing the mapping provides one of the greatest advantages of CG models [59].

Just like polymers, complex fluids also exhibit multiple length and time scales. Therefore, simulation methods across scales are required in order to study such sys-

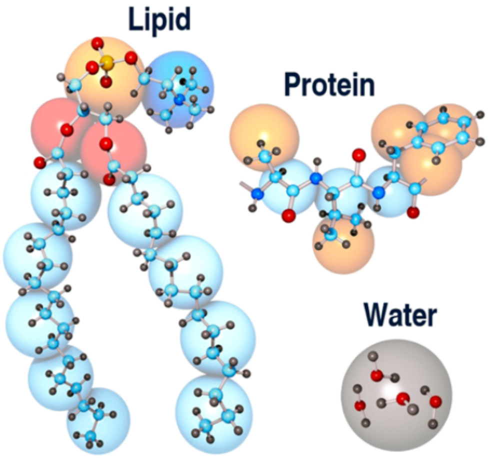

Figure 1-7: All-atom versus coarse-grained representation in the MARTINI model. Extracted from Ref. [60].

tems. On the all-atom-level description, classical atomistic models have successfully been used in order to quantitatively predict the properties of molecular systems over a considerable range of different thermodynamic conditions [12, 39]. However, due to the broad spectrum of characteristic lengths and times involved in complex molecular systems, it is desirable to reduce the required computational cost by describing the system through a small number of degrees of freedom. Thus, coarse-grained (CG) models have been used in order to increase the length and time scales accessible by simulations [49, 53, 61–63].

While coarse-graining invariably aims at reducing the complexity of the underlying system, it is nonetheless important that a mesoscopic description correctly reproduces thermodynamic properties of the real system [64]. Many coarse-graining methods have been developed in recent years [65–68] with a vast majority of them being numerical, meaning that the effective pair potential is numerically optimized to reproduce some particular property calculated from a more detailed-level simulation. For example, a widely used procedure is the Iterative Boltzmann Inversion (IBI) technique [52], where an initial guess of the effective potential, $v_0(r)$, usually taken as the potential of mean force [$v_0(r) = -k_B T ln g(r)$] is used in a trial simulation, yielding a new radial distribution function, $g_0(r)$, which is different from the target $g(r)$. This provides a correction term to the pair potential by Boltzmann inversion of the difference in the radial distribution functions, $k_B T ln[g_0(r)/g(r)]$. This procedure is then iterated until the effective pair potential reproduces the correct target radial distribution function (RDF) as measured in an atomistic simulation. Examples of other structure-based approaches include the inverse Monte Carlo method [1] [69–71], the multiscale coarse-graining (MS-CG) approach, which is based on a force-matching procedure [62], and the structure-based method of Kremer and co-workers [48, 53, 67, 72]. Another approach of Nielsen, et al. optimizes coarse-grained potentials to match experimental bulk density and surface tension values [73], while a coarse-grained model for DNA has been proposed for which the force field parameters are obtained through an iterative procedure to match experimental melting temperatures [74].

The overall schematic of the coarse-graining procedure is represented by Figure 1-8. First as an approximate model of the atomistic picture, we represent the actual polymer chain as a Gaussian thread. The parameters from this level of description enter the coarse-graining model, where individual chains are represented as soft colloidal particles, or point particles with a long-range, soft effective interaction.

Figure 1-8: Schematic description of the coarse-graining process. Extracted from Ref.[64].

In short, the simulation of complex fluids naturally involves widely different length scales. Integrating out parts of the microscopic degrees of freedom leads to the concept of effective interactions and provides a "coarse-grained" picture which can be simulated much more efficiently than a full microscopic model. This approach bridges length scales in complex fluids.

---

[1] In contrast to IBI, IMC is an exact Newton method and aims to directly fit g_{ij} rather than lng_{ij}.

Model systems and interaction potentials

The most important feature of the pair potential between atoms or molecules is the harsh repulsion that appears at short range and has its origin in the overlap of the outer electron shells. The effect of these strongly repulsive forces is to create the short-range order that is characteristic of the liquid state. The attractive forces, which act at long range, vary much more smoothly with the distance between particles and play only a minor role in determining the structure of the liquid. They provide, instead, an essentially uniform, attractive background and give rise to the cohesive energy that is required to stabilize the liquid [24].

The potential energy V contains the interesting information regarding intermolecular interactions: assuming that V is fairly sensibly behaved, it will be possible to construct an equation of motion (in Hamiltonian, Lagrangian, or Newtonian form) which governs the entire time-evolution of the system and all its mechanical properties [75]. Solution of this equation will generally involve calculating, from V, the forces $\mathbf{f}_i$ and torques τ_i acting on the molecules. The Hamiltonian H also dictates the equilibrium distribution function for molecular positions and momenta. Thus, generally, it is H (or V) which is the basic input to a computer simulation program. The approach used almost universally in computer simulation is to separate the potential energy into terms involving pairs, triplets, etc. of molecules (atomic systems):

$$U(r) = \sum_i v_1(\mathbf{r}_i) + \sum_i \sum_{j>i} v_2(\mathbf{r}_i, \mathbf{r}_j) + \sum_i \sum_{j>i} \sum_{k>j} v_3(\mathbf{r}_i, \mathbf{r}_j, \mathbf{r}_k) + ... \qquad (1.1)$$

The notation indicates a summation over all distinct pairs (or triplets) i and j (and k) without counting any pair twice. The first term in eqn 1.1, $v_1(\mathbf{r}_i)$, represents the effect of an external field (including, e.g. the container walls) on the system. The remaining terms represent particle interactions. The second term, v_2 , the pair potential, is the most important. The pair potential depends only on the magnitude of the pair separation r_{ij}, so it may be written $v_2(\mathbf{r}_{ij})$.

The v_3 term in eqn 1.1, involving triplets of molecules, is undoubtedly significant at liquid densities. It is found that up to 10 % of the lattice energy of argon (and more in the case of more polarizable species) may be due to these non-additive terms in the potential; we may expect the same order of magnitude to hold in the liquid phase. Four-body (and higher) terms are expected to be small in comparison with v_2 and v_3.

Despite the size of three-body terms in the potential, they are only rarely included in computer simulations [76, 77]. This is because the calculation of any quantity involving a sum over triplets of molecules will be very time-consuming on a computer. In most cases, the pairwise approximation gives a remarkably good description of liquid properties because the average three-body effects can be partially included by defining an 'effective' pair potential. To do this, we rewrite eqn 1.1 in the form:

$$U(r) \approx \sum_i v_1(\mathbf{r}_i) + \sum_i \sum_{j>i} v_2^{eff}(\mathbf{r}_i, \mathbf{r}_j). \tag{1.2}$$

The pair potentials appearing in computer simulations are generally to be regarded as effective pair potentials of this kind, representing all the many-body effects.

A typical intermolecular potential, averaged over the orientations of the molecule, operates over three ranges: short distances, where interaction is harshly repulsive because of overlapping electronic shells; long distances, where forces are essentially attractive (Van der Waals forces) and decrease gradually with distance, the dominant contribution coming from multipole dispersion interactions; intermediate distances with a minimum determined from the balance of repulsive and attractive forces. Such behaviour is illustrated by the Lennard - Jones potential (fig 1-9) ,which models fairly well interactions in argon-like fluids. Substances interacting through this potential exhibit the 'standard' phase diagram with two fluid phases (gas and liquid) below the critical point and a solid phase at high densities [25].

Core-softened potentials

The most rudimentary microscopic model for a substance capable of existing in any of the three most familiar states of matter - solid, liquid and gas - is based on

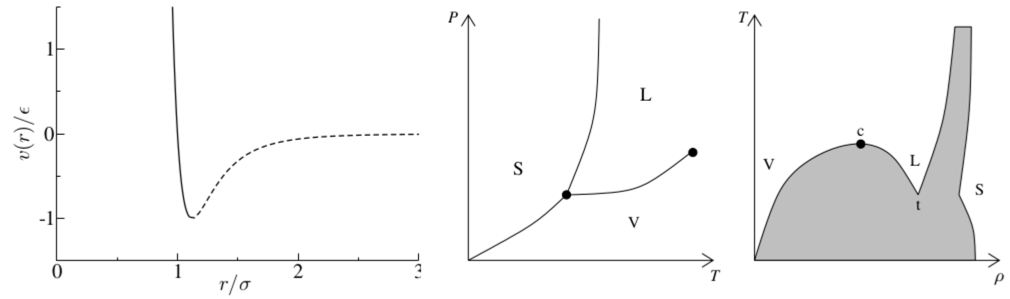

Figure 1-9: left: the Lennard-Jones potential as a function of interatomic distance. middle and right: schematic phase diagrams of a simple one-component substance in the temperature (T) - pressure (P) and density (ρ) -T planes. The shaded area in the right panel indicate regions of two-phase coexistence [25].

spherical particles that interact with one another; the best known of these potentials, originally proposed for liquid argon, is the Lennard-Jones (LJ) potential (fig. 1-9) [28].

For the purposes of investigating general properties of liquids, and for comparison with theory, highly idealized pair potentials may be of value. Studies have been directed towards the determination of the phase behavior of identical particles interacting through different model potentials. It was shown, for instance, that the usual solid-liquid-gas phase diagram of particles interacting through a hard core repulsion plus a long-range attraction is modified when the range of the attraction is decreased [78, 79]. More precisely, the liquid-gas coexistence curve disappears if the range of the attractive potential is lower than about 30% of the hard core radius. More interestingly, when the range of the attractive potential is reduced below about 8% of the repulsive range, a coexistence curve separating two isostructural solid phases appears [80].

The phase behaviour of single component systems as particles interacting via the so-called core-softened (CS) potentials has received a lot of attention recently. The first studies in core-softened (CS) potentials were done by Stell and Hemmer [81, 82], who concluded that for a system in which the pair potential has a hard core plus a negative part (fig 1-10), softening the hard core can produce a second transition if a first has already occured (in order to explain the isostructural solid–solid transition

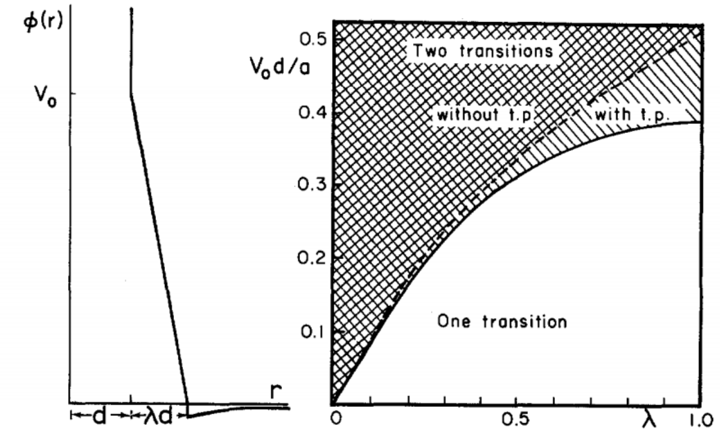

Figure 1-10: The one-dimensional potential and the range of potential parameters for which two transitions exist [81].

ending in a critical point). This important finding implies that strong orientational interactions , such as those that exist in water and silica, are not a necessary condition for a liquid to have thermodynamic and dynamic anomalies [83].

Debenedetti et al [84], using general thermodynamic arguments, confirmed that a CS can lead to a coefficient of thermal expansion negative and consequently to density anomaly. At end of 1990's, Jagla's works [80, 85, 86] brought new elements to the discussion by analyzing how phase transitions are related to the various possibilities of attenuation of the isotropic hard core potential as well as the relationship between this softening and the water anomalies. The recently acknowledged possibility of the existence of single component systems which display coexistence between two different liquid phases has opened many interesting questions, and shed new light into the study of the anomalous properties of these systems [87]. The case of water is probably the most intensively studied, due to its ubiquity in nature. The relation between CS potential and the negative coefficient of thermal expansion, together with the increase of the thermal compressibility, has been used as an indication of the presence of two liquid phases [88, 89] which may be hidden beyond the homogeneous nucleation. The difficulty with these approaches is that continuous potentials usually lead to crystallization at the region where the critical point would be expected [90].

These potentials exhibit a repulsive core with a softening region with a shoulder or a ramp (fig 1-11). In the first case, the potential consists of a hard core, a square repulsive shoulder, and, in some cases, an attractive square well [89, 91] . In the second case, the interaction potential has two competing equilibrium distances, defined by a repulsive ramp [80, 85, 86]. By including a global term for attraction, this model displays a liquid phase with a first-order line of liquid-gas transition ending in a critical point and a liquid-liquid phase transition ending in a second critical point [92, 93].

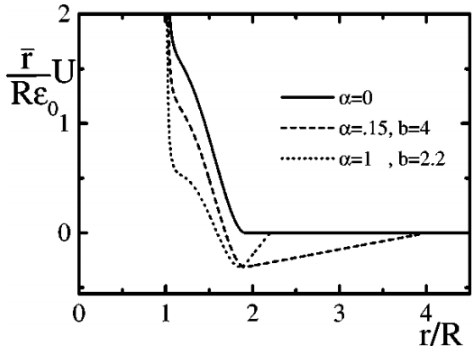

Figure 1-11: The interparticle potential U(r) without attraction (continuous line) and for two different choices of the attractive part [86].

These models originate from the desire to construct a simple two-body isotropic potential capable of describing the complicated features of systems interacting via anisotropic potentials. This procedure generates models that are analytically and computationally tractable and that one hopes are capable of retaining the qualitative features of the real complex systems. In the last decade, several other models of core-softened potentials have emerged, which describe fairly well the water-like anomalies, among which we can mention the Alan et al model [94] and the Franzese model [95], both represented in Figure 1-12. Franzese's CS model was used in this thesis to describe mixtures of water and short-chain alcohols, as we will see in chapter 4.

The remainder of this thesis is organized as follows. Chapter 2 reviews polymers and colloids and their combination in a polymer grafted-nanoparticles. Chapter 3 addresses water and tert-butanol mixtures, and in chapter 4 we will approach Water and Short-Chain Alcohol Mixtures: methanol, ethanol and 1-propanol. Chapter 5 introduces the Final Remarks of this work. In the appendices, publications and

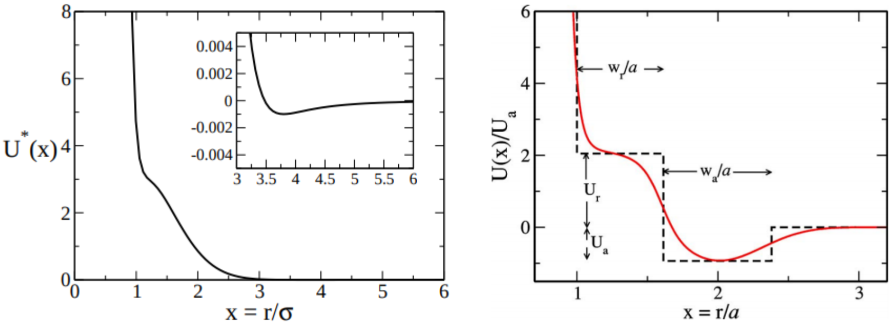

Figure 1-12: core-softened potentials with different length scales [94, 95].

submissions (with the respective electronic supplementary materials) originating from this thesis can be found.

Chapter 2

Polymer Grafted Nanoparticles

2.1 Introduction

Polymers and Nanoparticles

Polymers have been a part of life since the beginning of humankind. In the majority of their many applications, polymeric materials are not chemically or molecularly homogenous but are multicomponent systems (heterogeneous materials with at least one characteristic length scale in the nanometer range[1]). By adding fillers, such as minerals, ceramics, metals, or even air, materials scientists can generate an infinite variety of materials with unique physical properties and competitive production costs - the (Polymer) Nanocomposites [96]. In mechanical terms, nanocomposites differ from the conventional composite materials due to the high aspect ratio of the reinforcing phase and/or its exceptionally high surface to volume ratio (fig. 2-1). Since surface and surface properties are decisive in chemical and chemical interactions, a nanostructured material can have substantially improved properties than a material with the same composition and bigger-dimensional components [97].

Significant historical examples of Nanocomposites include the use of reinforcing mud walls in houses with bamboo shoots, glued laminated wood by Egyptians (1500 B.C.), and laminated metals in forging swords (A.D. 1800) [99] . They have been

---

[1] The transition from microparticles to nanoparticles of its components leads to a drastic change in the properties of the material.

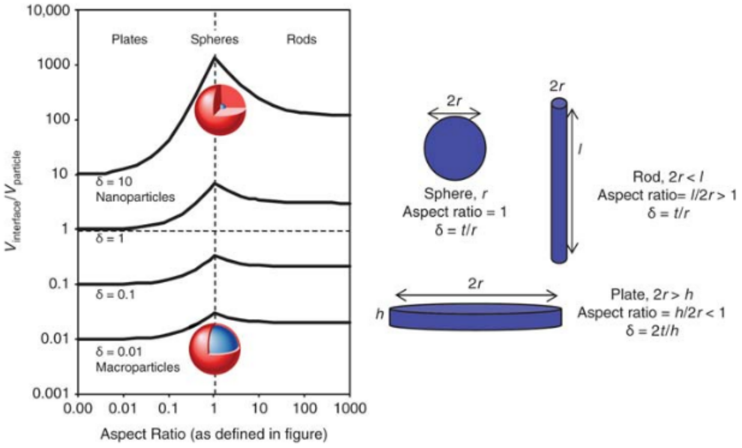

Figure 2-1: The ratio of interfacial volume to the particle volume ($V_{interface}/V_{particle}$) as a function of the particle aspect ratio and the ratio of the interfacial thickness to the particle size (δ) [98].

manufactured throughout human history scarcely, as for example Blue Mayan, an azure pigment used in paint by Mayans and Aztecs based on different clays, which conserves the tone over more than 4000 years [100].

Polymer Nanocomposites incorporate a new spectrum of fillers that extend the function and utility of polymers while maintaining the manufacturing and processing flexibility inherent to plastics, thermosets, and resins. In particular, Polymer Nanocomposites have been successful with regard to overcoming traditionally antagonistic combinations of properties. The mixing of nanoparticles with polymers to form composite materials has been practiced for decades. For example, the clay reinforced resin known as Bakelite was introduced in the early 1900's as one of the first mass-produced polymer-nanoparticle composites and fundamentally transformed the nature of practical household materials. Even before Bakelite, nano-composites were finding applications in the form of nanoparticle-toughened automobile tires prepared by blending carbon black, zinc oxide, and/or magnesium sulfate particles with vulcanized rubber[101]. From the mid-1950s nanoscale organo-clays have been used to control flow of polymer solutions (e.g. as paint viscosifiers) or the constitution of gels. However, it has been relatively soon (1970 decade) that their promises of realizing unique combinations of properties unachievable with traditional materials have caused an explosion of research in this area [102] . This surge in the field of nanotechnology has been facilitated by the appearance of the scanning tunneling microscopy and the scanning probe microscopy in the early 1980s.

Despite these early successes, the broad scientific community was not galvanized by nano-composites until the early 1990s, when reports by Toyota researchers revealed that adding mica to nylon produced a five-fold increase in the yield and tensile strength of the material [103, 104]. Subsequent developments have further contributed to the surging interest in polymer-nanoparticle composites.

The properties of polymer nanocomposite (PNCs) are determined, in part, by the chemical composition of the polymer and the type and size of nanoparticles: metallic oxides, graphene, quantum dots, nanorods, clays, fullerenes and metallic nanocrystals. However, the properties of the composite materials can be engineered through judicious selection and chemical and physical modification of nanoparticles and polymer [105].

The global market for nanocomposites totaled 2.0 billion in 2017 and is estimated to reach 7.3 billion dollars by 2022, growing at a compound annual growth rate (CAGR) of 29.5 % for the period of 2017-2022 [106]. Asia-Pacific accounted for the largest share in the global polymer nanocomposite market, owing to widespread adoption in industrial and automotive sectors in countries, like India and China [107].

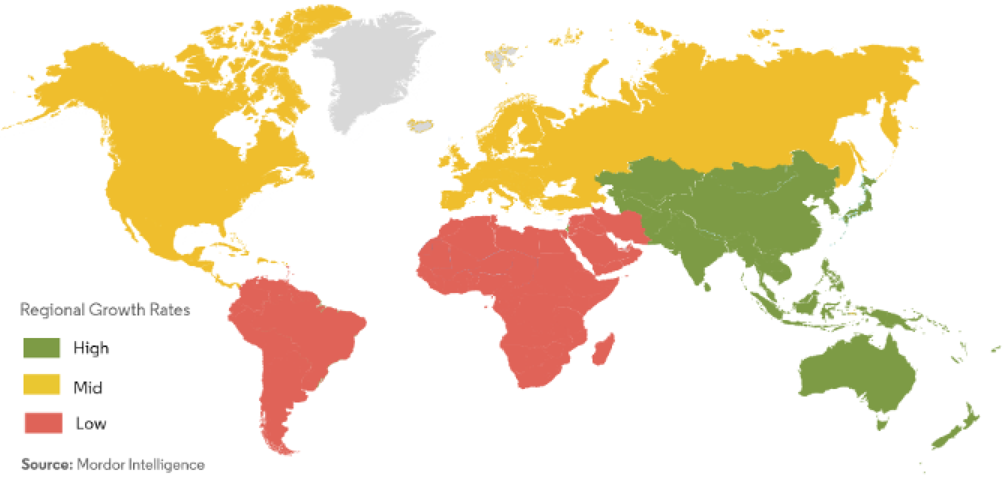

Figure 2-2: Polymer Nanocomposite market: growth rate by region. 2019-2024 [107].

Colloids

Colloidal systems of gold particles were already known many centuries ago, and their nature, being "extremely finely divided gold in a fluid, was recognized as early as 1774 by Juncher and Macquer [108]. Colloidal dispersions were first described by Selmi in 1845, who called such dispersions "pseudo-solutions" and explained the anomalous colligative properties by assuming that the "dissolved" entities or particles were much larger than the regular-sized molecules, such that at a given concentration (by mass per unit volume) the particle concentration was extremely low [109]. The year 1861 marks the beginning of systematic research in colloidal systems by the publications of Thomas Graham [110], who coined the term "colloids" (from the Greek $\kappa o\lambda\lambda\alpha$ which means glue) for particles in Selmi's pseudo-solutions. Graham distinguished between two types of solutions: solutions in which species dissolved particles are capable of diffusing through the membrane - called crystalloids, and solutions where little or no diffusion across the membrane was observed. Graham named the latter kind of solution "colloids" [111].

Prior to Graham's publications in 1827, botanist Robert Brown observed irregular movement of (colloidal-sized) pollen grains in water as a result of random collisions of solvent particles with colloidal particles [112]. The experimental work of Jean Perrin [113] confirmed Einstein's theoretical predictions in 1906 [114] and Langevin in 1908 [115] and found that colloidal particles are nothing more than "large molecules" (compared to solvent molecules, but still small enough to exhibit thermal motion) exhibiting Brownian motion. Later Onsager [116, 117], McMillan and Mayer [118] laid the foundations of statistical mechanics for the atom-colloid analogy: they pointed out that the degrees of freedom of solvent molecules in a colloidal dispersion can be eliminated, implying that the solvent can be considered a continuous background. The resulting description involves only colliding particles interacting via effective potentials, the average force potential, which takes into account the solvent effects.

Colloidal dispersions

According to IUPAC, the term colloidal refers to a state of subdivision, implying that polymolecular molecules or particles dispersed in a medium have at least in one direction an approximate size between $1nm$ and $1\mu m$, or that in a system discontinuities are found at distances of this order. This means that colloidal particles are supramolecular substances (of sizes much larger than "normal" molecules although they may be comparable in size to macromolecules) of submicron size dispersed in a medium that may be liquid or gas [109].

Colloidal solutions are commonly referred to as suspensions or dispersions, since solid material (colloidal material) is suspended (or dispersed) in the liquid phase. There are three types of dispersions, depending on the properties of colloidal particles: (i) colloidal particles are rigid entities; (ii) they are very large and flexible molecules (macromolecules), and (iii) they are clusters of small molecules that are in thermodynamic equilibrium with their environment. The medium formed by small molecules in a colloidal suspension can be considered as secondary to the colloidal size range and approximated as a continuum. From a physical point of view, colloidal particles are characterized by an observable brownian motion, originating from a thermal energy of the order of kT for each colloidal particle. Particles in a solvent are considered brownian if sedimentation can be neglected with respect to thermal agitation, which indicates that the sedimentation length, the ratio of thermal energy to gravitational force,

$$l_{sed} = \frac{kT}{m^* g}, \tag{2.1}$$

must be greater than the radius of the colloid. Here the floating mass m^* is $(4\pi/3)\Delta\rho R^3$ for a spherical colloid of radius R, where $\Delta\rho$ is the density difference between the particle and solvent [109, 119].

Just as the pressure in an atomic gas is affected by the interaction between atoms, the physical properties of a colloidal dispersion depend on the average force potential between the colloidal particles. An extended law of the corresponding states has been conjectured by stating that knowledge of the average force potential between colloidal spherical particles allows us to predict the phase diagram (topology). Therefore, we can expect similarities between phase diagrams of atomic and colloidal systems. Once the similarities are established, there are major differences between atoms and colloidal particles, as interactions between colloidal particles can be adjusted by choosing particle type, temperature, solvent, supplementing additives such as electrolytes, polymers, or colloidal particles, or by modifying the surface of the particle. Since the 1970s it has become clear that adding small particles or polymers that do not adsorb on colloids opens up a wide range of colloidal dispersion phase diagram adjustment possibilities [120].

Colloidal dispersions can be found in a wide range of products. Industrial examples include emulsions (mayonnaise), foams (shaving cream), surfactant solutions (shampoo) and latex polymer dispersions (paints). The science of colloids is important for applications ranging from drug and dairy delivery to technology covers and perforating fluids. Often, long stability of a colloidal dispersion is desirable, for example in food or paint storage, and chemically adjusting the surface of the particle or via adsorption are possibilities to ensure this stability. An example where colloid (clay) instability plays a role in nature is delta formation [121]. In foods and biological systems such as living cells, colloids and polymers are present simultaneously. When polymers are not adsorbed on the surface of colloids, the result is the so-called depletion layer, which may cause an attractive interaction between colloidal particles.

DVLO Theory

The basic understanding of colloid interactions began around 1940. So Dejarguin and Landau in the former Soviet Union [122] and Verwey and Overbeek in the Netherlands [123] pointed out that in a dispersion of charged colloids in an electrolyte solution the attraction Van de Waals' relationship between two colloidal particles is compensated by a repulsion originating from double electric layers (fig. 2-3). This rationale for colloid stability is known as the DLVO theory and has been considerably successful in explaining the results of a wide range of experiments, including direct force measurements.

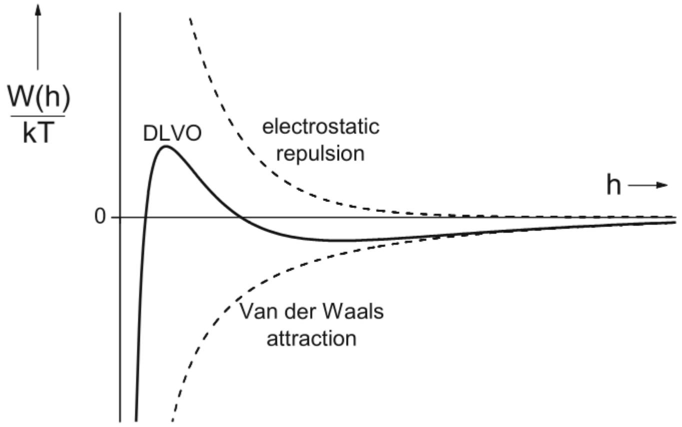

Figure 2-3: Schematic plot of a typical double layer repulsion between charged colloidal spheres (top), of the Van der Waals attraction (bottom) and their sum, which is the DLVO interaction potential [120].

Influence of grafted Polymers

Polymers, whether adsorbed or anchored on colloidal surfaces, also directly influence colloidal interactions, which are not considered in DLVO theory. In other words, colloidal dispersions can be very well stabilized by polymers grafted to their surfaces [124]. As two colloidal particles protected by grafted polymers approach each other, the local osmotic pressure increases dramatically due to the steric obstacles of the chains of both particles. This competition between chains for the same volume leads to a repulsive interaction [125].

Polymers can be attached to surfaces for example as mushrooms, brushes and absorbed chains (fig.2-4). In the case of brushes and mushrooms, chains are chemically attached to the surface at one end. Brushes are characterized by a high packing density. When polymers adsorb to the surface, many segments stick and wrap to the surface. Grafted polymers can contribute to a significant repulsive interaction between particles. If the attached polymers overlap, the osmotic pressure between the surfaces increases considerably, which leads to a repulsive interaction between the particles.

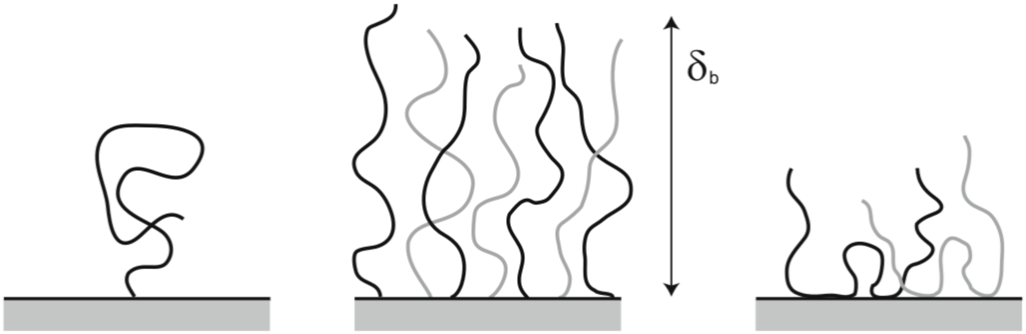

Figure 2-4: Schematic pictures of polymers attached at a surface: a mushroom (left), a brush (middle), and a layer of adsorbed polymer (right) [120].

In the figure 2-5, we see the effect of adding a polymeric brush to two colloidal spheres subject to Van der Waals attraction. If the two particles approach each other, the concentration of polymer solution within the gap increases, leading to an increase in osmotic pressure, causing a repulsive force.

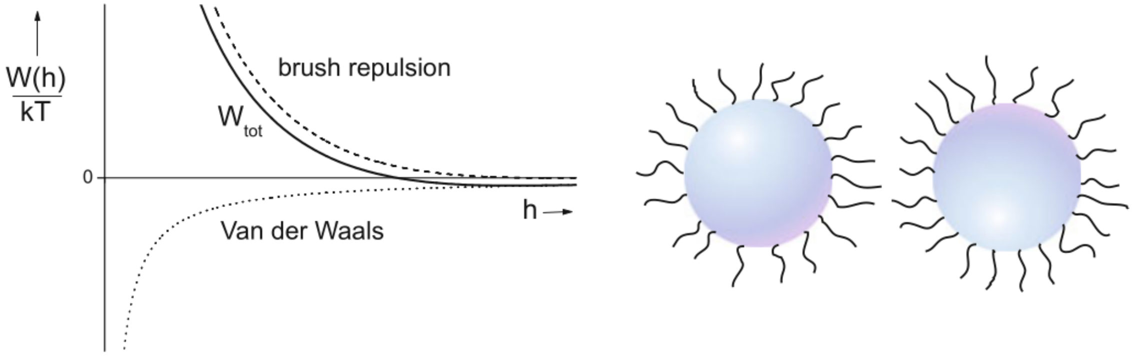

Figure 2-5: Sketch of the influence of a brush repulsion on two spheres with Van der Waals attraction [120].

It is commonly assumed that total interaction is the sum of interactions between pairs of particles:

$$W_{tot} = \sum_i W_i = W_{VdW} + W_{brush}. \tag{2.2}$$

Without the grafted polymer chains, the particles would coagulate spontaneously, as Van der Waals's attraction is too strong for small h values. However, by adding repulsion between the polymeric brushes, the total interaction (solid curve) is repulsive for a large range of h values.

Depletion Interaction

Finally, the depletion interaction arises whenever the solution contains, in addition to the suspended particles, other particles of intermediate size between the colloidal particles and the solvent. The most common case occurs when the suspension contains a dissolved polymer that does not adsorb on the surface of the particles. The situation is illustrated in figure 2-6 polymer molecules, described herein as spheres, are excluded from a region of thickness L external to the surface of the particles - the depletion zone. As the particles approach, the depletion zones overlap, with the result that there is a volume of solution between the particles in which the concentration of polymeric molecules is lower than in the rest of the solution. This means that the difference in osmotic pressure between the solution and the depletion zone leads to an attractive entropic force for most distances.

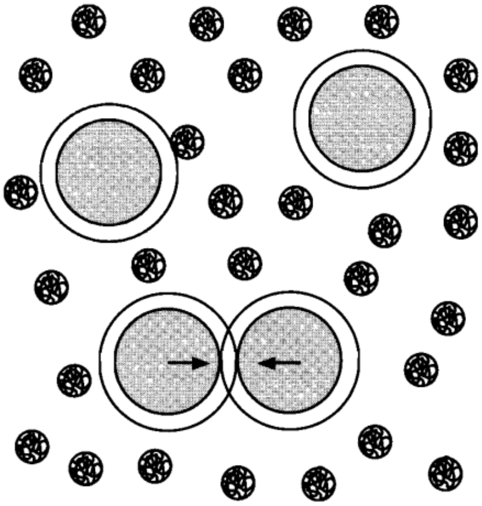

Figure 2-6: The depletion interaction [126].

In the figure 2-7, we have the influence of a depletion attraction and a brush repulsion as total interaction. The presence of brushes reduces attraction [127].

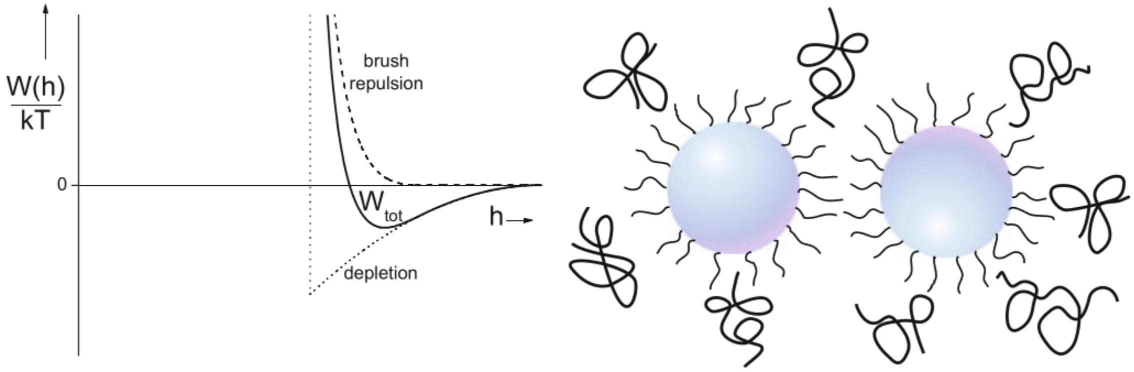

Figure 2-7: Sketch of the total interaction potential between two spheres covered with polymer brushes in a good solvent in a solution containing non-adsorbing polymer chains [120].

2.2 Polymer Nanocomposites

Polymer Grafted Nanoparticles: the "nanoparticle limit"

Polymer-grafted nanoparticles (NPs), also called hairy NPs (HNPs), are an intriguing class of nanostructured materials consisting of a layer of macromolecular chains covalently grafted on the surface of NPs, often inorganic and metallic [128, 129]. Capable of exhibiting unique, combined properties of core NPs and surface-tethered polymers, HNPs have received tremendous interest in the past two decades and have shown great promise in a variety of applications, including advanced polymer nanocomposite fabrication, drug delivery, sensing, imaging, aqueous and oil lubrication, and catalysis [130–135]. HNPs feature numerous design possibilities of combining polymers and NPs (fig. 2-8).

The core can be solid, mesoporous, or hollow, with a size ranging from a few to hundreds of nanometers [137–141]. In terms of geometry, the core NPs could have a regular shape, such as spherical, cubic, and rod-like, or an irregular shape. Compositionally, although the core NPs are often inorganic and metallic, polymers have also been employed [142, 143]. On the other hand, the surface-grafted polymers can have various chemical compositions and topologies, such as homopolymers, random copolymers, block and star copolymers, bottlebrushes, and cyclic polymers, as well as

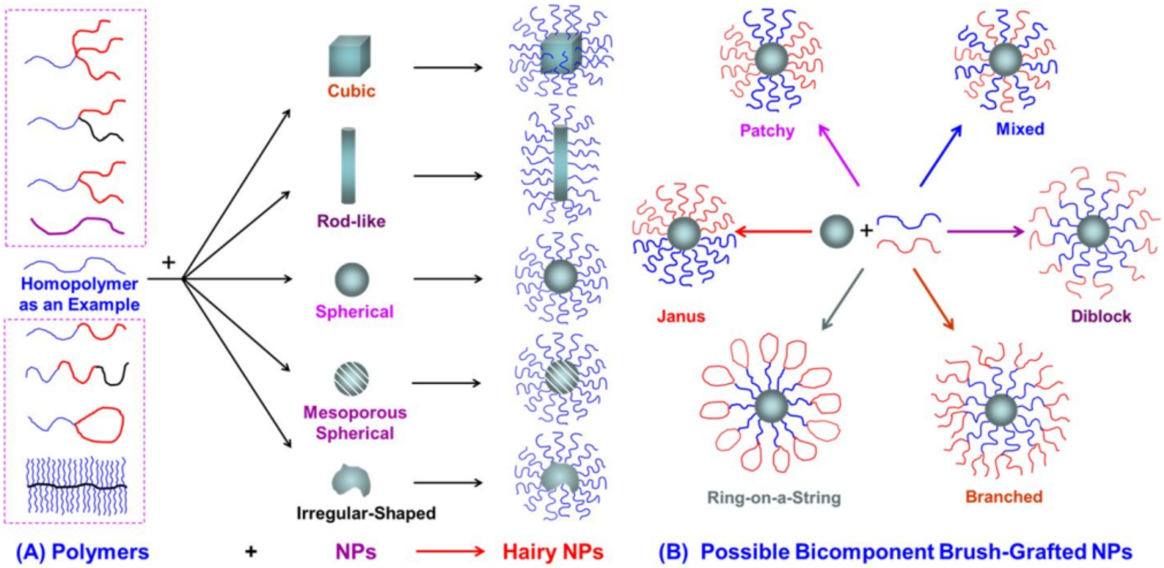

Figure 2-8: (A) Schematic Illustration of various types of Polymer-Grafted Nanoparticles by combining polymers with different architectures and NPs using a Homopolymer as an Example and (B) Examples of bicomponent brush NPs [136].

different grafting densities; possible examples of bicomponent polymer brush- grafted NPs are schematically illustrated in fig. 2-8B [144–148]. Imaginably, each combination represents a set of HNPs with unique structures and potentially interesting behavior. Despite vast possibilities of combining polymers and NPs to form HNPs, so far only a very limited set of well-defined HNPs has been synthesized and experimentally studied due to the challenges in synthesis and characterization. Figure 2-9 illustrates the various NPs chemistries, the different surface functionalization strategies adopted to date, and the fields that these NPs are expected to be relevant in [131].

Hairy nanoparticles can be dispersed in a polymer miscible for the grafting or similar, avoiding chemical incompatibilities which lead to aggregation. In general, the properties of these materials rely on the grafting; nevertheless, some entropic phenomena may occur, as autophobic dewetting which restricts dispersion in a highmolecular weight matrix[149–152] . The morphological structure of mixtures of polymer matrix with hairy nanoparticles depends on the grafting density, the chain length, the interaction between the grafted chains and between the host (polymer matrix) and grafted

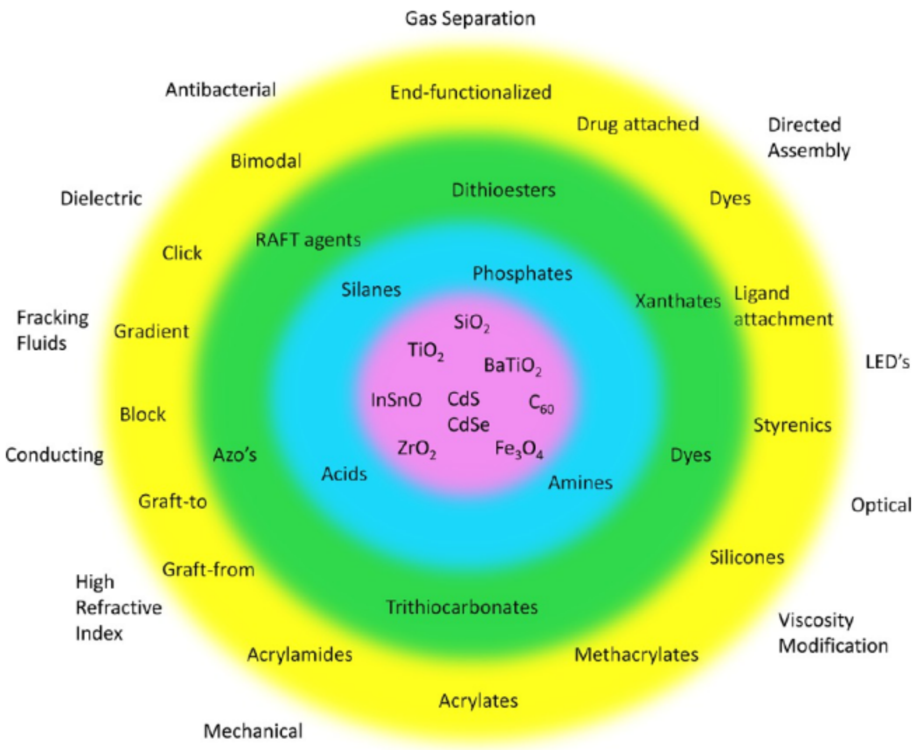

Figure 2-9: Schematic illustration of the various types of NP available, the forms of surface functionalization, and the applications that these materials can impact. [131].

chains [153]. On the other hand, changing particle size and length of grafting polymer on the fillers, all can significantly affect polymer nanocomposite properties. Other important properties to consider besides are nanoparticle curvature and the thermodynamic (Flory–Huggins) interaction parameter, χ , between the host and grafted chains [154] . However if the grafted polymer and the polymer matrix are the same, the interaction parameter should be favorable ($\chi < 0$). At very low grafting densities, the morphology of these polymer nanocomposites (PNCs) is largely determined by the attractive enthalpic interactions ($H < 0$) between the nanoparticle cores, mediated by entropic interactions with the grafted polymer chains. The entropic term comes from the fact the matrix polymer chains lose entropy when they are confined between the surfaces of two adjacent particles. Entropic effects that drive the chain interpenetration capacity scale as the inverse of the chain length, whereas enthalpic contributions are proportional to the chain length. These competing interactions have been shown to be responsible for the anisotropic organization of the nanoparticles within polymer hosts as we will see in the next sections. At high grafting densities, however, even in cases where the host chains (polymer matrix) and the grafted chains have identical chemical structure, the entropic grafted layer/free chain interactions are dominant, leading to miscibility (isotropic dispersion of the nanoparticles within the polymer host) or to microscopic and macroscopic phase separation. Summarizing, both entropic and enthalpic factors affect the miscibility between the grafted and the surrounding matrices and therefore the morphology. In order to entropically favor wetting and entanglement of the matrix chain for polymer grafted nanoparticles, the degree of polymerization (length) of the graft, N, should to be equal to, or larger than, the degree of polymerization of the matrix chains [154].

Polymer Grafted Nanoparticles: the "colloid limit"

The role of the polymer in these mixtures has traditionally been as a colloidal stabilizer or rheological modifier, and characterized by the feature that the polymer size (i.e. the length scale controlling polymer physics, denoted generically as R_g) is much smaller than the size of the particle, R [155–157]. This "colloid" limit constitutes the conventional regime for which many theoretical models and simulation approaches have been developed. At an equilibrium level, much information can be gleaned about this limit by studying the interactions between flat surfaces in polymeric media [158]. At a dynamical level, much progress can be made by modeling the polymeric matrix as a continuum non-Newtonian fuid [159]. More recent developments in nano and biotechnology applications have however moved the polymer–particle mixtures from the "colloid limit" to the "nanoparticle limit" where $R_g > R$. For instance, at the last section systems termed as polymer nanocomposites (PNCs) were adressed, in which nanoparticles of sizes $5 - 50nm$ (comparable to R_g) are routinely dispersed in polymeric matrices to enhance their properties. The above-discussed transition to the nanoparticle limit has also identified a number of new physical phenomena which have challenged the fundamental understanding of the properties of polymer–particle composites. For instance, at the equilibrium level, the curvature of the particle has been shown to play an important role in determining the interactions within the composite and the resulting phase behavior of the system [160, 161]. At a dynamical level, a number of observations have been reported where "continuum" theories seem to breakdown, leading to surprising and counter-intuitive phenomena [162, 163]. Not surprisingly, such observations have also spurred a number of theoretical and computational efforts aimed at elucidating the structure and properties of polymer nanocomposites.

It is often difficult to control the dispersion of nanoparticles into polymer matrices as inorganic particles are typically immiscible with an organic phase [160, 164]. One strategy to overcome this difficulty is to ‘shield’ the particle surface by grafting it with the same chains as the matrix polymer [150, 165]. Although this approach for particle dispersion is successful in some cases, we find instead that the particles can exhibit self-assembly into highly anisotropic structures. This process arises because the immiscible particle core and grafted polymer layer attempt to phase separate but are constrained by chain connectivity - this is evidently analogous to ‘microphase separation’ in block copolymers and other amphiphiles. Similar to these amphiphiles, these particles with a ‘polarizable’ segmental cloud can self-assemble under a broad range of conditions into a variety of superstructures. Simulations show that the competition between a short-ranged attraction and a long-ranged repulsive interaction (SALR) between nanoparticles can rationalize these experiments [166] as we can see on fig 2-10.

Compared to the atomistically detailed molecular simulations, there are many more simulation studies on systems containing polymer grafted particles using coarse-grained models:

- Meng et al. [168] have conducted molecular dynamics simulations with a generic coarse-grained model of polymer grafted nanoparticle in a polymer matrix of identical chemistry. They claim that at the single particle limit the system does not exhibit autophobic dewetting, the phenomenon where the free matrix chains increasingly dewet the grafted chains of same chemistry as the matrix chain length increases (Fig 2-11).

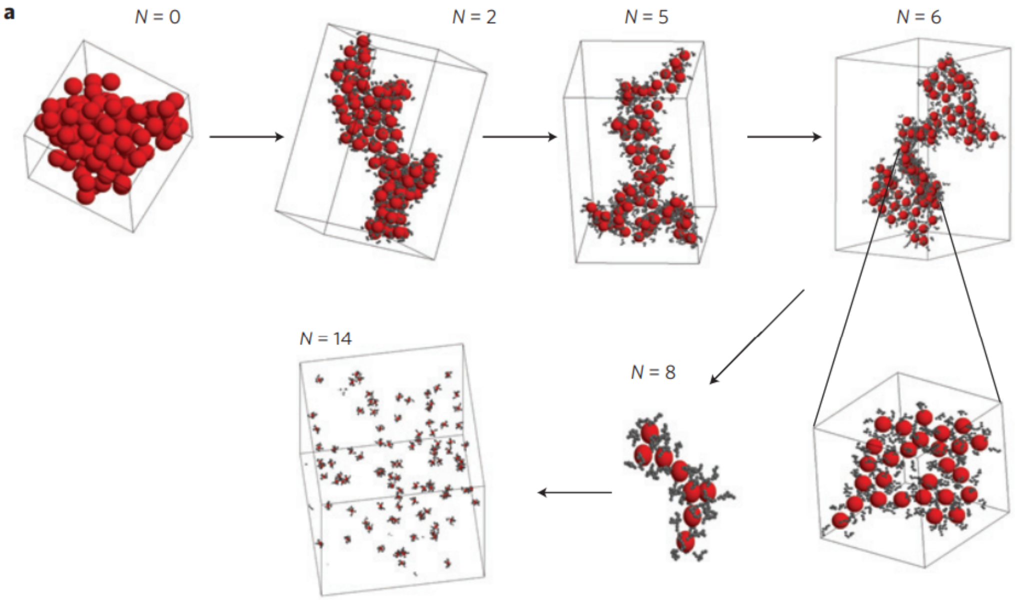

Figure 2-10: Simulation snapshots for particles with six uniformly spaced grafts, going from bare particles forming spherical aggregates, to flattened cylinders with $N = 2$; branched cylinders with thinner arms $N = 5$; sheets with $N = 6$ (sheet shown in the detail); long strings with $N = 8$ (only one string shown); short chains with $N = 10$ (not shown); and isolated particles with $N = 14$. [167]. N is the number of monomers in each chain.

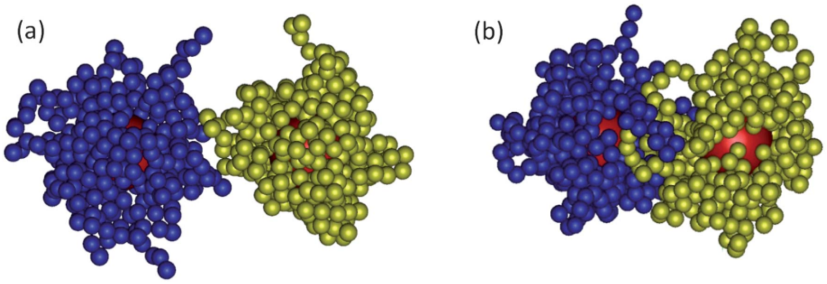

Figure 2-11: Snapshots of two grafted nanoparticles in polymer matrix at two separation distances (a) $D = 11\sigma$ and (b) $D = 8\sigma$ [168]. σ is the length unit in reduced units.

- Shen et al [169] also used coarse-grained simulations of multiple polymer grafted particles in an explicit matrix to show that in addition to the expectation that particles will aggregate when the matrix length is much greater than the graft length at high grafting density, there exists an optimum grafting density, σ_c , for observing dispersion of the grafted nanoparticles in the polymer matrix (Fig 2-12).

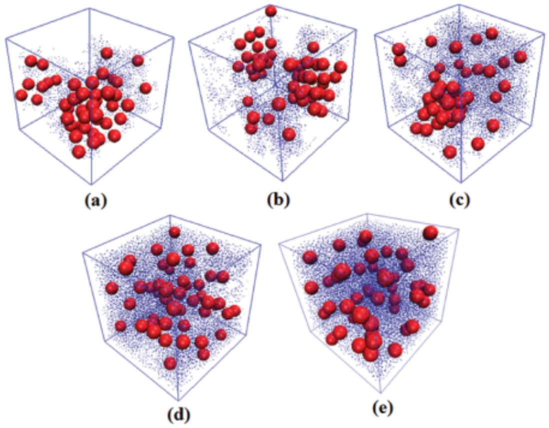

Figure 2-12: The snapshots corresponding to the following simulation systems: $N_g = 10$; $N_m = 10$; and the grafting densities (σ) vary as $0.1, 0.2, 0.4, 0.6$, and 0.8, corresponding to diagram a, b, c, d, and e, respectively. The red spheres denote the NPs, and the blue points represent the grafted chains [169]. N_g is the grafted chain length and N_m is the matrix chain length

- Chremos and Panagiotopolous [170] have used coarse-grained MD simulations to study structural transitions within a system of polymer grafted nanoparticles in the absence of a matrix polymer or a solvent (melt-like conditions), at varying grafting density and varying particle size. At high grafting density, even with a sufficiently large core, they found that the behavior of polymer grafted particles was similar to star polymers, "where the thermal expansion of the corona traps the nanoparticles and a glassy behavior is observed." In contrast, at low enough grafting density, the corona cannot prevent neighboring nanoparticles from aggregating, in agreement with prior theoretical studies.

- Goyal and Escobedo performed coarse-grained molecular dynamics simulations of polymer grafted nanoparticles in the absence and presence of a matrix consisting of a polymer melt to investigate how particle core concentration, polymer grafting density, and polymer length affected the particle mobility and viscous response [171]. They carried out constant strain-rate simulations to calculate viscosities and constant-stress simulations to calculate yield stresses. They found that in the systems of polymer grafted nanoparticles the structural order and viscosity decrease and diffusivity increases with increasing length of the grafted chains for a given core concentration or grafting density. Figure 2-13 describes their nanoparticle model.

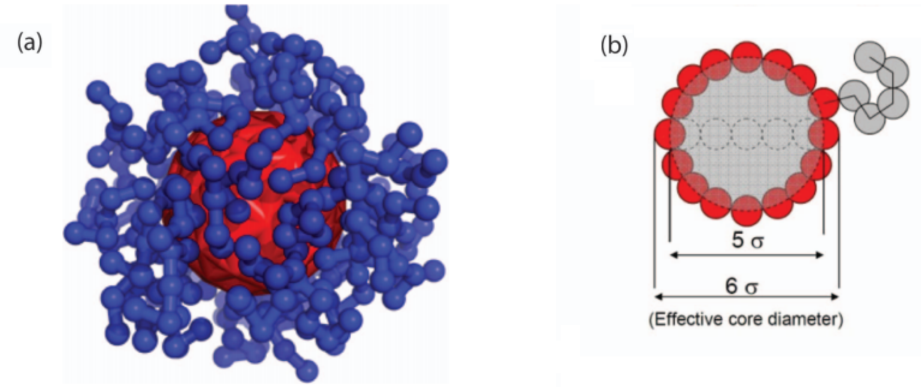

Figure 2-13: (a) Schematic of a typical PGN and (b) its aproximate dimensions [171].

- Chremos and Douglas realized that grafting of polymer chains onto the surface of spherical nanoparticles leads to a hybrid type of fluid that exhibits properties of both particle suspensions and melts of star polymers, these properties being controlled by the relative dimensions of the grafted polymer chains to the nanoparticle diameter, D, and the number of the number of chains grafted on the nanoparticle surface, f.

- Lafitte et al [172] use large-scale molecular dynamics simulations with a coarse-grained model to investigate the self-assembly of solvent-free grafted nanoparticles into thin free-standing films. The nanoparticles self-assemble into a variety of morphologies ranging from dispersed particles, finite stripes, long strings, to percolating networks. The main driving force for these morphologies is the competition between strong short-range attractions of the particle cores and long-range entropic repulsions of the grafted chains (Fig 2-14).

- Hansoge et al [173] recently (march 2021) developed a computational framework to predict the effective pairwise interparticle interactions between polymer-grafted nanoparticles with different design parameters, that is, polymer chain length, grafting density, and polymer chemistry. They found that the repulsive part of the interaction can be expressed as an exponential repulsion term,

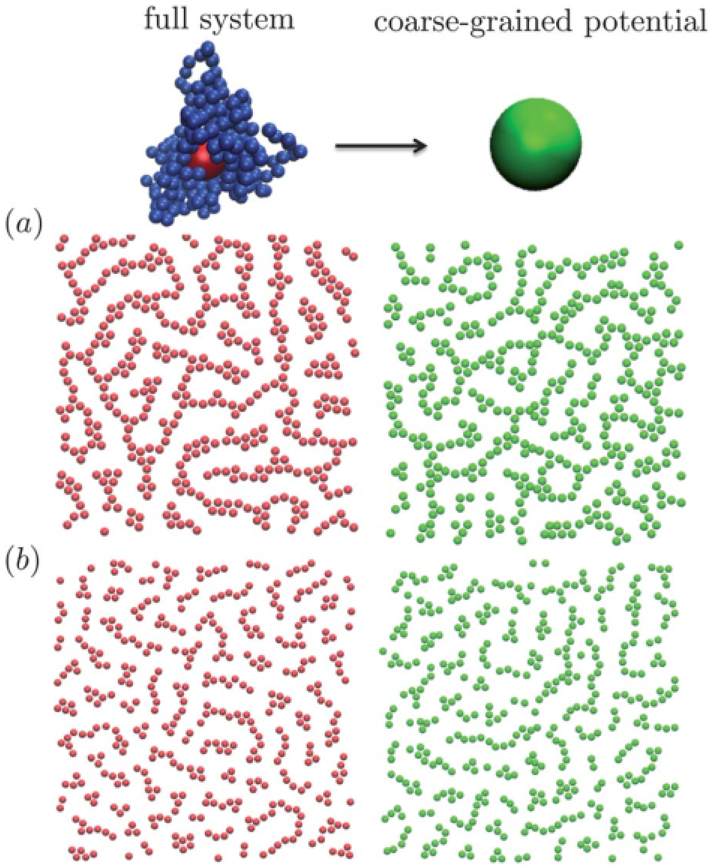

Figure 2-14: Comparison of equilibrium configurations obtained with the full model and the spherically symmetric coarse-grained potentials obtained from the inverse-Boltzmann procedure [172].

whereas the attractive part is best captured using a sigmoidal form (Fig 2-15).

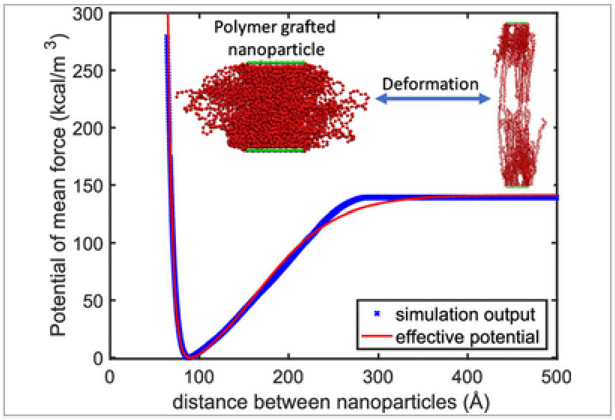

Figure 2-15: Potential of mean force in function of distance [173].

2.3 Soft Colloids

Colloidal dispersions are chemically complex systems which hold a special position in condensed matter physics, not only because of their broad technological applications, but also because they represent excellent model systems for the study of molecular interactions, including the possibility to "engineer" soft matter, once their equilibrium phase behavior can nevertheless be understood in terms of the physical concepts originally coined for the study of simple fluids. Indeed, once the solvent-mediated interactions between the colloidal particles are described in terms of an effective pair potential, the determination of the phase diagram of a complex colloidal dispersion is, in principle, not more difficult than for a simple fluid [5, 78].

Based on this analogy, the polymer grafted nanoparticle system analyzed in this work falls into the category of soft colloids (Fig.2-16) because of their size and because such systems have been studied by effective two-scale models able to reproduce well the phase diagram of these systems [169, 170, 174, 175], exhibiting the dynamic and thermodynamic anomalies common in water-type systems. Moreover, it is clear that potential isotropy is capable of generating a multitude of aggregation patterns resulting from competition between attenuated potential scales (U_{rigid} and, less pronounced U_{free}).

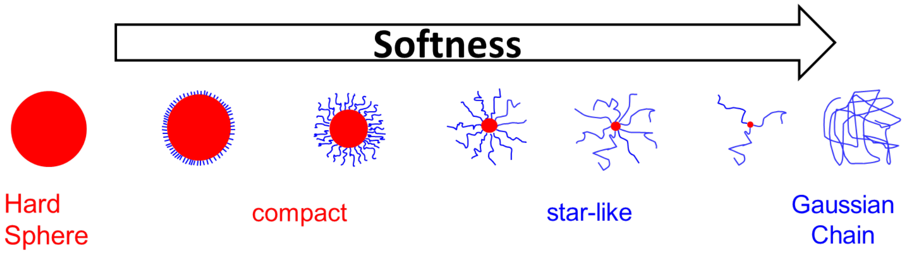

Figure 2-16: Continuous transition scale from totally hard to soft. Extracted from Ref. [176].

The systems studied - polymer grafted nanoparticles - have been characterized in recent literature as *hairy nanoparticles*, and have as cause of the different morphologies observed the competition between entropic (separation) and enthalpic (aggregation) effects [177, 178]. Then, molecular dynamics simulations with effective core-softened potentials were used to investigate the self-assembly of polymer grafted nanoparticles in two cases: one where the polymers are free to rotate around the nanoparticle core and a second where the polymers are fixed, with a 90° angle between them. The use of effective core-softened potentials allow us to explore the complete system phase space. In this way, the PT, $T\rho$ and $P\rho$ phase diagrams for each potential were obtained, with all fluid and solid phases. The plenty of morphologies ranging from dispersed particles, finite stripes and long strings were obtained. Similar to Laffite's previous case, the main driving force for these morphologies is the competition between length scales of potential, as we will see at the next sections.

2.4 Model and simulation details

The objective of our work is to analyze the structural, thermodynamic and dynamic behavior of polymer-grafted nanoparticle systems through effective potentials in light of molecular dynamics. Particularly, we are interested in how the structure and dynamics of the grafted polymers can affect the system behavior. The polymers can be adsorbed to the nanoparticle core to coat fully or partially the surface. In this case, if the polymer grafted density is low, the polymers are free to rotate along the surface. This is not the case where a polymer is grafted to the surface by a reactive group or the polymerization is initiated from a small molecule attached to the core surface, where the polymer is binded to a site and can not rotate [179]. Then a question that arises is how the polymer dynamics and the extra degree of freedom can influence the nanoparticles system properties. To answer this question we obtain an effective potential for two cases of grafted nanoparticles: one where the polymers are binded to a reactive group, and another where the polymers are grafted to the surface and are free to rotate. The effective potential allow us to explore the complete phase diagram with a low computational cost, and has been shown in the literature that it can qualitatively describe the system as well as the CG model [172]. As well, we show that the effective model can correctly predict the morphologies and dynamical behavior observed in the CG model. Also, in this first moment we are interested in 2D systems. To achieve practical applications, some grafted nanoparticles must assemble over a large 2D area. Also, the assembly in solid-liquid interfaces can be approached by 2D models [180]. Therefore, the 2D analysis is relevant for these cases.

A possible route to analyze the thermodynamical behaviour of core-softened systems (among which water) is through Polymer-Grafted nanoparticle systems. The recent advances in the study of Polymer Nanocomposites may be a healthy computational alternative to the analysis of waterlike anomalies. Here we analyze the thermodynamic and dynamic behavior of a solution of nanoparticles coated by polymers. Our task has two complementary aspects: to show the impact and feasibility of modeling and identifying a system which exhibits water-like anomalies. The first task entails to describe the complex system of polymer grafted-nanoparticle by representing the chemical and physical interactions by simple potentials creating a coarse grained model. Next, we observe that this model system presents two length scales interactions which are the building blocks for the existence of water-like anomalies.

Finally, we go on step further in our aim of creating a minimum model and we derive an effective potential for the grafted nanoparticles interactions. This potential allow us to explore the pressure versus temperature phase diagram for the system and to check the phase space for the presence water-like anomalies. The pressure versus temperature phase diagram obtained employing the effective minimum model is then checked with the phase diagram constructed for the coarse grained approach. The existence of the phases observed for both models are then confirmed with experimental data. Here we employ two complementary strategies to describe the polymer-grafted nanoparticles phase diagram: a coarse grained model and an effective core-softened potential.

The Coarse-Grained (CG) Model

We employ a two dimensional coarse-grained model proposed in previous works [167, 172, 181] to describe polymer-grafted nanoparticle interactions. Each core-shell nanoparticle is composed of a central disk with diameter σ_c with 4 linear oligomer chains attached. Each chain consists of 3 beads with diameter σ_b, connected by an harmonic bond

$$U_{bond}(r_{ij}) = k\left(r_{ij} - \sigma_b\right)^2 \tag{2.3}$$

with $k = 5000\epsilon/(\sigma_b)^2$ (reduced LJ units), to ensure tangential bonding between pairs of catenated beads. The bead-bead (bb) interaction is modeled by the standard Lennard Jones (LJ) potential

$$U_{bb}(r_{ij}) = 4\epsilon\left[\left(\frac{\sigma_b}{r_{ij}}\right)^{12} - \left(\frac{\sigma_b}{r_{ij}}\right)^{6}\right] - U_{LJ}(r_{cut}) \tag{2.4}$$

where $r_{cut} = 2.5\sigma_b$ and $\epsilon = \epsilon_c/9.0$. For the core-core (cc) interaction was used a 14-7 LJ potential,

$$U_{cc}(r_{ij}) = 4\epsilon_c\left[\left(\frac{\sigma_c}{r_{ij}}\right)^{14} - \left(\frac{\sigma_c}{r_{ij}}\right)^{7}\right] - U_{cc}(r_{cut}) \tag{2.5}$$

where $r_{cut} = 2.5\sigma_c$. Finally, the core-bead (cb) interaction is given by taking an arithmetic mean between attractive and repulsive exponents of the U_{cc} (LJ 12-6) and U_{bb} (LJ 14-7) potentials, resulting in a LJ 13-6.5 potential [172],

$$U_{cb}(r_{ij}) = 4\epsilon_{cb}\left[\left(\frac{\sigma_{cb}}{r_{ij}}\right)^{13} - \left(\frac{\sigma_{cp}}{r_{ij}}\right)^{6.5}\right] - U_{cp}(r_{cut}) \tag{2.6}$$

where σ_{cb} and ϵ_{cb} are obtained by the well-known Lorentz-Berthelot combining rules:

$$\sigma_{cb} = \frac{\sigma_b + \sigma_c}{2} \;\; ; \;\; \epsilon_{cb} = \sqrt{\epsilon_c \epsilon_b}. \tag{2.7}$$

The first bead in the polymer chain is connected to the central core by a rigid bond [182]. Two cases of grafted NP were considered. In the first one the polymers are held fixed in the core surface with a separation of 90^o by the bend cosine square bond angle potential,

$$U_{bend} = \frac{k_{bend}}{2}[cos(\phi) - \cos(\phi_0)]^2 \tag{2.8}$$

with $k_{bond} = 50$ and $\phi_0 = \pi/4$. In the second case no bending potential was applied, and the polymers are free to rotate around the central colloid. Both structures are illustrated in the Figure 2-17.

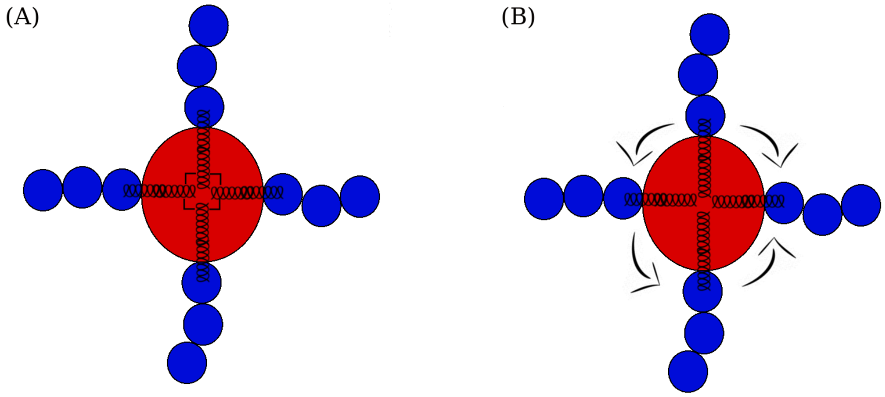

Figure 2-17: Schematic depiction of the CG nanoparticles. (A) Nanoparticles with a bend potential that prevents the polymers of slide along the core surface and (B) nanoparticles without bend potential whose polymers are free to rotate along the core surface.

In order to simulate a small silica core we use in this work $\sigma_{core} = 1.4$ nm and $\epsilon_{core}/k_b = 10179$ K, as proposed by Lafitte and co-authors [172]. The polymer beads have a diameter $\sigma_{bead} = 0.4$ nm and $\epsilon_{bead} = \epsilon_{core}/9.0$ and correspond to a ethoxy repeat unit [181]. For simplicity, in this paper all physical quantities are computed in the standard LJ units. Distance, density of particles, time, pressure and temperature are given, respectively, by

$$r^* \equiv \frac{r}{\sigma_{core}}, \quad \rho^* \equiv \rho\sigma_{core}^3, \quad t^* \equiv t\left(\frac{\epsilon_{core}}{m\sigma_{core}^2}\right)^{1/2}, \quad p^* \equiv \frac{p\sigma_{core}^3}{\epsilon_{core}}, \quad and \quad T^* \equiv \frac{k_B T}{\epsilon_{core}}. \tag{2.9}$$

Obtaining the Effective Core-Softened Potential

The effective core-softened (CS) potentials for the two polymer-grafted nanoparticles systems analyzed here were obtained as follows. Langevin Dynamics simulations using the ESPResSo package [183] were performed for the coarse-grained models (fixed and non free beads). The two systems were analyzed in the NVT ensemble for density $\rho^* = 0.25$ and temperature $T^* = 0.5$. These values were chosen to ensure that the coarse-grained models were both in the fluid state.

Then, the core-core radial distribution functions (RDF) for this state point for both fixed and free-bead systems were computed as illustrated in Figure 2-18. As

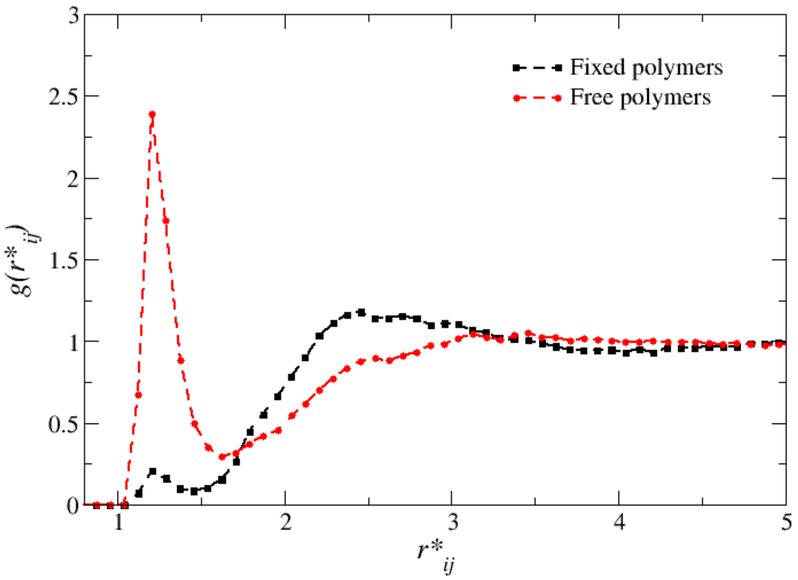

Figure 2-18: Radial distribution functions employed to obtain the effective interaction potential between NPs with polymers fixed (black squares) or free (red circles) to rotate. Both RDFs were obtained at the density of $\rho^* = 0.25$ and temperature $T^* = 0.5$.

we can see, the RDFs indicate a significant difference in occupancy of the two length scales. For the case of fixed polymers, black curve in the Figure 2-18, it is harder for the cores to remain close to each other. As consequence, this NP has a higher occupancy in the second length scale (the polymer corona) and a smaller in the first length scale - the hard core. The opposite is observed in the red curve of the Figure 2-18, corresponding to NP with polymers free to rotate, where the cores can approach one another easily, increasing the occupancy in the first length scale and decreasing in the second length scale.

From these RDFs curves, using both the solution of the Ornstein-Zernike equation [184] with integral equation approximation, the effective potentials for polymer-grafted nanoparticles with fix and non-fix beads were obtained [172, 184, 185].Briefly stated, the OZ equation

$$h(r) = c(r) + \rho \int c(\mathbf{r} - \mathbf{r}')h(\mathbf{r}')d\mathbf{r}' \ , \tag{2.10}$$

averaged over the orientational degrees of freedom, provides an exact relation between the translationally invariant radial distribution function, $h(r) = g(r) - 1$, the direct correlation function, $c(r)$, and the system density ρ [184]. With appropriately chosen closures, the OZ equation provides a relationship between an effective isotropic potential and the pair correlation functions. While the usual application of the OZ equation is to extract the RDF for a given model potential, our objective is to define the potential itself given the RDF. Next we require a closure for the OZ integral equation in order to obtain an approximation to the isotropic potential which reproduces the pair correlation function: after testing two closures(the Percus-Yevick and the Hypernetted Chain approximation), we have considered the last option. The potentials were also derived using the Iterative Boltzmann Inversion (IBI) procedure [52, 186]. In this method the effective pair interaction U_{eff} is iteratively updated to to match the pair correlation functions of a target system,

$$U_{eff}^{i+1} = U_{eff}^{i} + k_B T \ln\left(\frac{g^i(r)}{g^{target}(r)}\right) . \tag{2.11}$$

Here, $g^{target}(r)$ is the core-core RDF obtained from the CG simulations and $g^i(r)$ is the RDF obtained in the ith iteration. 50 iterations were sufficient to obtain convergence. Essentially the same potentials were obtained by both methods.

The polymer-grafted nanoparticles become represented by spherical particles interacting through these effective core-softened potentials as illustrated in Figure 2-19.

Based in previous works [184, 185, 187], our effective potentials are composed by a short-range attractive Lennard Jones potential and three Gaussian terms, each one centered in c_j, with depth h_j and width w_j:

$$U(r_{ij}) = 4\epsilon_{core}\left[\left(\frac{\sigma_{core}}{r_{ij}}\right)^{12} - \left(\frac{\sigma_{core}}{r_{ij}}\right)^{6}\right] + \sum_{j=1}^{3} h_j exp\left[-\left(\frac{r_{ij} - c_j}{w_j}\right)^2\right] , \ . \tag{2.12}$$

Here, $r_{ij} = |\vec{r}_i - \vec{r}_j|$ is the distance between two cores i and j. The resulting potentials

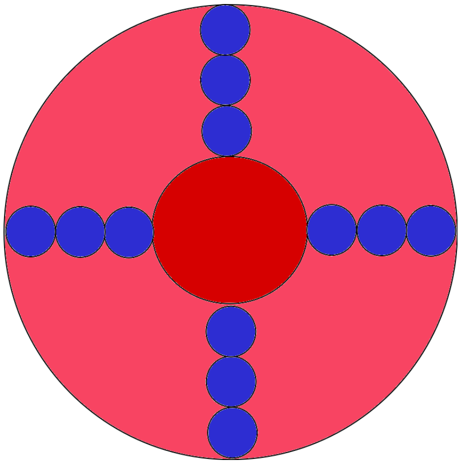

Figure 2-19: Schematic depiction of the effective nanoparticles. It has a central hard core (the red sphere) and a soft corona (the lighter red sphere).

and fittings are shown in the Figure 2-20 for case of NP with polymers fixed (U_{fixed}) or free (U_{free}) to rotate. The parameters correspondent to each case are given in the table 4.1.

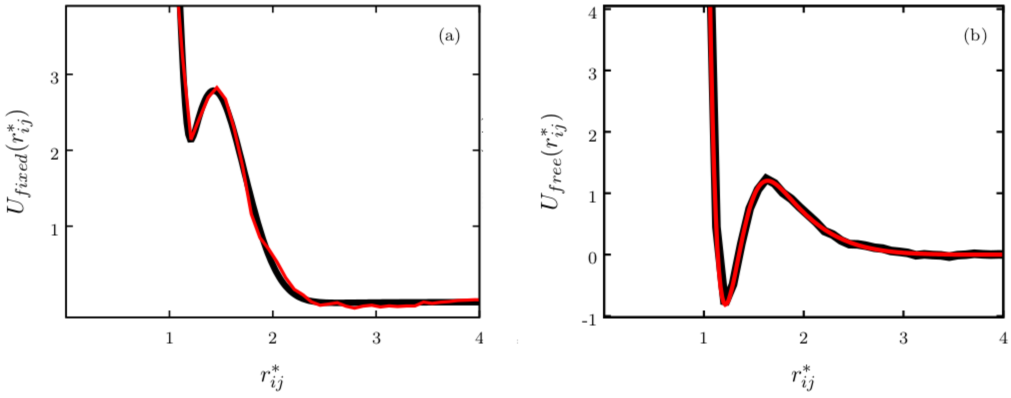

Figure 2-20: Core-softened potential for polymer-grafted nanoparticles with four monomers (a) fixed and (b) free to rotate around nanoparticle core. The red curve is the potential obtained by solving the Ornstein-Zernike equation, and the black curve is the LJ+Gaussian fit.

In the effective potentials is also clear the effect of the polymers mobility. When they are held fixed the energetic penalty for two NPs move from the further (or second) scale to the closer (or first) scale is higher than in the case when the polymers can rotate and expose one core to another. As consequence, the U_{fixed} potential has a ramp-like shape, while the U_{free} a short range attraction and a long range repulsion

$\mathbf{U_{fixed}}$ potential		**$\mathbf{U_{free}}$ potential**	
Parameter	Value	Parameter	Value
h_1	3.50803	h_1	-3.80084
c_1	1.05317	c_1	1.11192
w_1	0.0887196	w_1	0.313324
h_2	3.2397	h_2	46.1324
c_2	1.37689	c_2	0.774361
w_2	0.468399	w_2	0.191852
		h_3	6.37621
		w_3	0.192937
		c_3	1.23615

Table 2.1: Parameters of the particle-particle potentials in reduced units.

(SALR) shape.

Simulation Details for the Effective Potential

The systems consists of 800 disks with diameter $\sigma = \sigma_{core}$. Langevin Dynamics simulations were performed with a time step of $\delta t = 0.001$. Periodic boundary conditions were applied in both directions. We performed 5×10^5 steps to equilibrate the system. These steps were then followed by 2×10^6 steps for the results production stage. To ensure that the system was equilibrated, the pressure, kinetic and potential energy were analyzed as function of time. The velocity-verlet algorithm was employed to integrate the equations of motion. The NVE ensemble was employed for equilibration and NPT ensemble for the production run. The Langevin thermostat, with a damping parameter $\gamma = 1.0$, was employed to fix the system temperature and the pressure was held fixed by the Nose-Hoover barostat with a parameter $10\delta t$. The simulations of the effective model were performed using the Large-scale Atomic/Molecular Massively Parallel Simulator (LAMMPS) package [188] and the PT, $T\rho$ and $P\rho$ phase diagrams for each potential were obtained.

The dynamic anomaly was analyzed by the relation between the mean square displacement (MSD) and time, namely

$$MSD = \left\langle |\vec{r}(t) - \vec{r}(t_0)|^2 \right\rangle , \tag{2.13}$$

where $\vec{r}(t_0)$ and $\vec{r}(t)$ denote the coordinate of the particle at a time t_0 and at a later time t, respectively. The MSD is related to the diffusion coefficient D in tow dimensions by [12]

$$D = \lim_{t \to \infty} \frac{\langle \Delta r^2(t) \rangle}{4t}. \tag{2.14}$$

The structure of the fluid was analyzed using the radial distribution function (RDF) $g(r_{ij})$. In order to check if the system exhibits the density anomaly, the temperature of maximum density (TMD) was computed for different isobars in the $T-\rho$ diagram. The phase boundaries were defined analyzing the specific heat at constant pressure, C_P [12] (Fig 2-21),the system mean square displacement, the radial distribution function and the discontinuities in the density-pressure phase diagram.

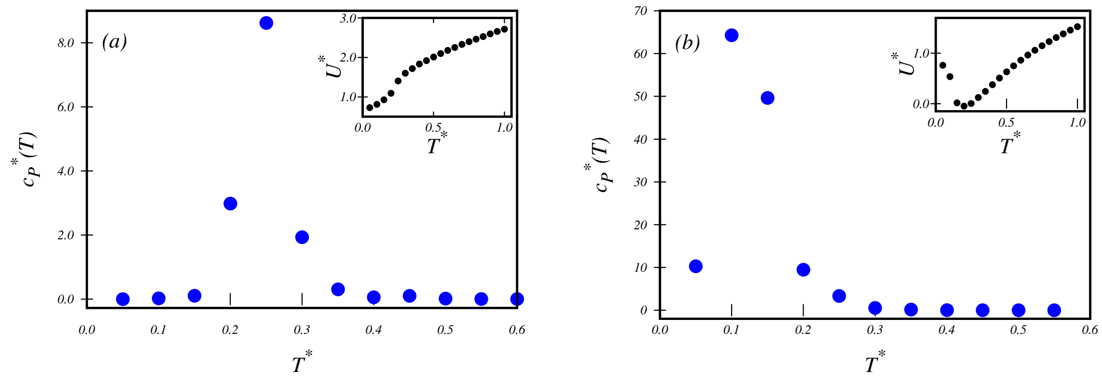

Figure 2-21: (a) Specific heat versus temperature at $P^* = 1.20$ for U_{rigid} potential. (b) Specific heat versus temperature at $P^* = 0.60$ in potential with polymers are free to rotate. In both, it's possible to see divergences.

2.5 Results and discussions

Here we analyze the thermodynamic and dynamic behavior of the system of polymer-grafted nanoparticles represented by the effective core-softened potentials generated for fixed and free beads systems.

Polymer-grafted nanoparticles with fixed polymers

The pressure versus temperature phase diagram obtained using the effective potential for the grafted nanoparticles with fixed polymers (see the potential in figure 2-20(a)) is illustrated in figure 2-22. Three solid structures were observed. At lower pressures, a hexagonal solid was obtained, as shown in the snapshot 2-22(a). Increasing the pressure the system enters in the region were the anomalous behavior is observed - the waterlike anomalies which will be discussed next. A consequence of the anomalies in the phase diagram is the presence of a reentrant liquid phase and a transition from the well defined hexagonal lattice to an amorphous stripe-like structure. This order-disorder transition was observed in previous works where particles interact through two length potentials also known as the ramp-like potentials [189–191]. In the previous works as here the anomalies arise from the competition between the two length scales. The figure 2-23 illustrated the density versus temperature for fixed pressure showing the maximum density, a water-like anomaly.

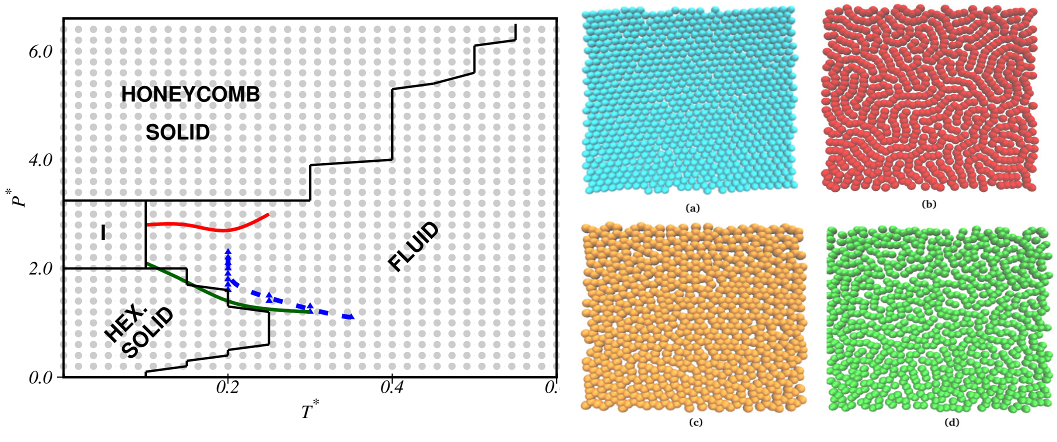

(a) (b)

Figure 2-22: (a) Pressure versus temperature phase diagram of system with fixed polymers. The gray lines are the isochores,the black lines divide the distinct phases, I represents the hexagonal solid phase, the blue line indicates the TMD, the green and red lines are the maxima and minima in diffusion coefficient. (b) System snapshots for: (a) hexagonal solid($P^* = 0.40$ and $T^* = 0.05$); (b) amorphous solid($P^* = 2.80$ and $T^* = 0.10$); (c) honeycomb solid($P^* = 5.00$ and $T^* = 0.20$); (d) fluid ($P^* = 5.00$ and $T^* = 0.80$).

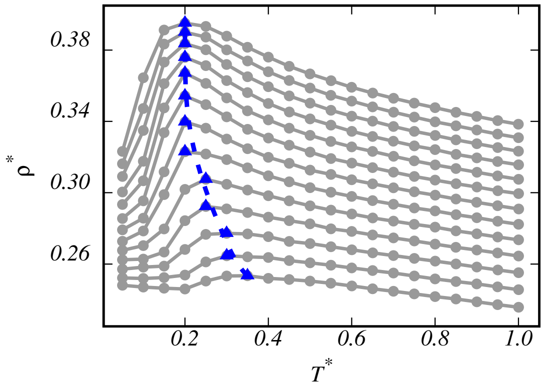

Figure 2-23: Temperature of Maxima Density for isobars between $P^* = 1.10$ and $P^* = 2.30$ from bottom to top.

The effective model is obtained from the coarse-grained system using a radial distribution function for one specific temperature and pressure. This raises the question of how reliable is this approach to describe the system for many pressures and temperatures. In order to test how robust is the effective model, we performed additional simulations for the coarse-grained description of the polymer-grafted colloidal system in the region where the anomalous behavior in the effective model was observed. Then, new NPT simulations of the CG system composed of 1000 NPs. Four points in the phase diagram were selected: (I) $T^* = 0.10$ and $P^* = 1.0$ (inside the hexagonal solid region of the effective model phase diagram), (II) $T^* = 0.10$ and $P^* = 3.0$ (inside the stripe solid region of the effective model phase diagram), (III) $T^* = 0.10$ and $P^* = 4.0$ (inside the honeycomb solid region of the effective model phase diagram) and (IV) $T^* = 0.20$ and $P^* = 2.0$ (inside the reentrant fluid phase of the effective model phase diagram). Figure 2-24 illustrates these state points. The structures are similar to the obtained using the effective model, figure 2-22. This indicates that the effective model was able to capture the proper behavior of the CG model phase diagram.

One of the characteristics of systems interacting through two length scales potential as the potentials illustrated in figure 2-20 is the presence of thermodynamic anomalies. The density anomaly is characterized by a maximum in the $\rho(T)$ curve along an isobar. For constant pressure as the temperature increases the density increases by making particles migrate from one length scale to the other. This can be

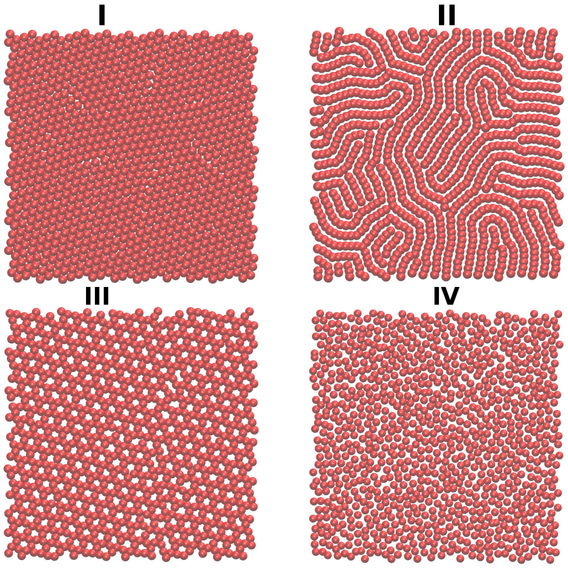

Figure 2-24: Patterns observed in the CG model, which are similar to snapshots from effective model (figure 2-22).

also observed in the radial distribution function $g(r_{ij})$ which presents two peaks: one at the closest scale, r_1, and another at the furthest scale, r_2. Recently it has been suggested that a signature of the presence of TMD line would be given by the radial distribution function as follows: at fixed temperature, as the density is increased, the radial distribution function of the closest scale, g(r_1), would increase its value, while the radial distribution function of the furthest scale, g(r_2), would decrease [192]. This can also be represented by the rule [95, 193]:

$$\Pi_{12} = \frac{\partial g(r)}{\partial \rho}\ |_{r_1} \times \frac{\partial g(r)}{\partial \rho}\ |_{r_2} < 0\ . \tag{2.15}$$

The physical picture behind this condition is that, for a fixed pressure, as the temperature increases, particles that are located at the attractive scale, r_2, move to the repulsive scale, r_1 - the thermal effects, which occur up to a certain pressure threshold $P^*_{min} = 0.90$. For pressures in range $0.90 < P^* < 3.00$, for a fixed temperature, as the pressure increases, particles exhibit the same offset between the potential length scales r_1 and r_2 - the pressure effects. Figure 2-25 illustrate a typical radial distribution functions at fixed T^* as P^* is varied [(a) and (b)] and vice-verse [(c) and (d)].

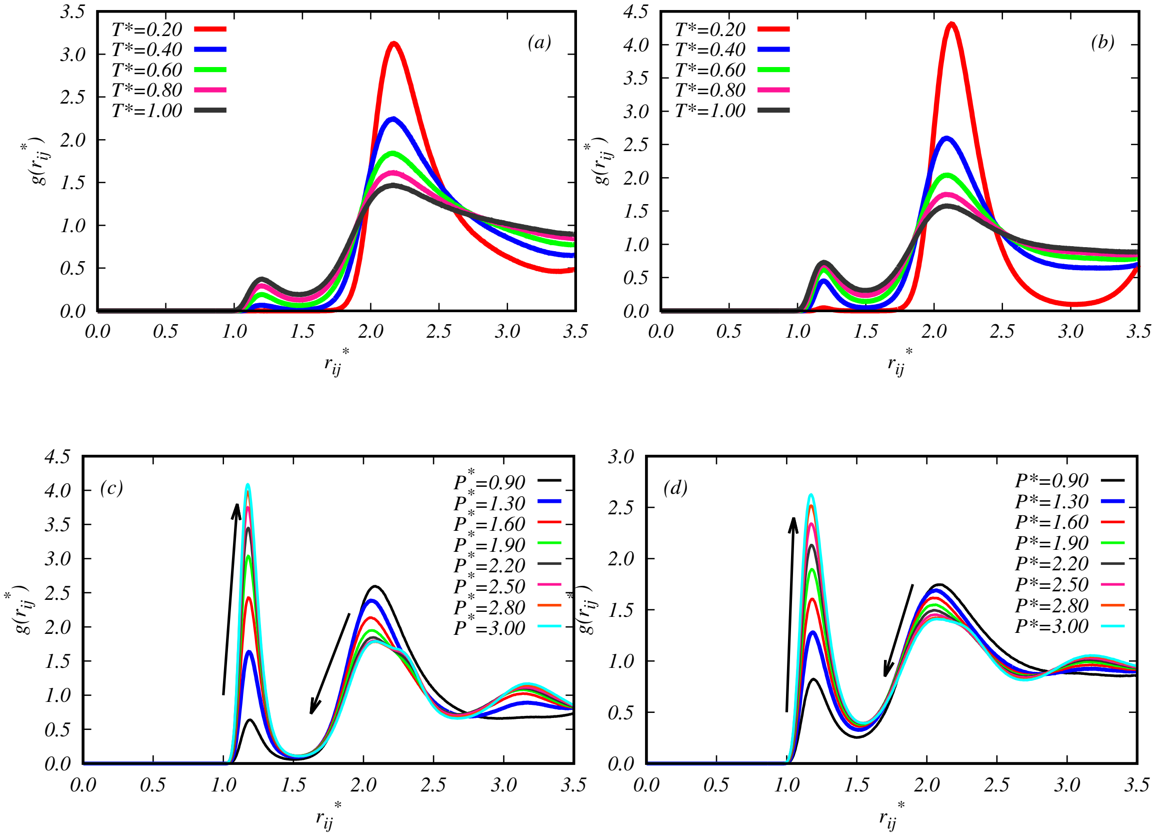

Figure 2-25: Radial distribution function behaviour for pressure two values below the threshold and temperature variation ($P^* = 0.40$ in (a) and $P^* = 0.80$ in (b)) indicating thermal effects in this region. At bottom figures, RDF's for two fixed temperatures ($T^* = 0.40$ in (c) and $T^* = 0.80$ in (d)) and pressure variation inside range $0.90 < P^* < 3.00$ indicating pressure effects in TMD region.

The regions identified by the radial distribution function as fulfilling the condition Eq. 2.15 are illustrated as red circles in figure 2-27(a). The solid curve shows the TMD line. All the stable state points with density equal or higher the minimum density at the TMD line verify the relation $\Pi_{12}(\rho, T) < 0$. This result gives support to our assumption that the presence of anomalies is related to particles moving from the furthest scale, r_2, to closest length scale r_1. In addition it indicates that the two length scales in the effective potential are related to the core-core repulsion competing withe polymer-polymer attraction present in the coarse-grained potential.

Another signature of anomalous fluids is the behavior of the diffusion coefficient which increases with density. Figure 2-26 represents the diffusion coefficient versus pressure for different isotherms, showing that D in a certain range of temperatures and pressures increases with pressure. The minimum in the diffusion coincides with the melting line. This behavior of the diffusion and melting line is related to an order - disorder transition and was previously observed for ramp-like potentials in two dimensions [191].

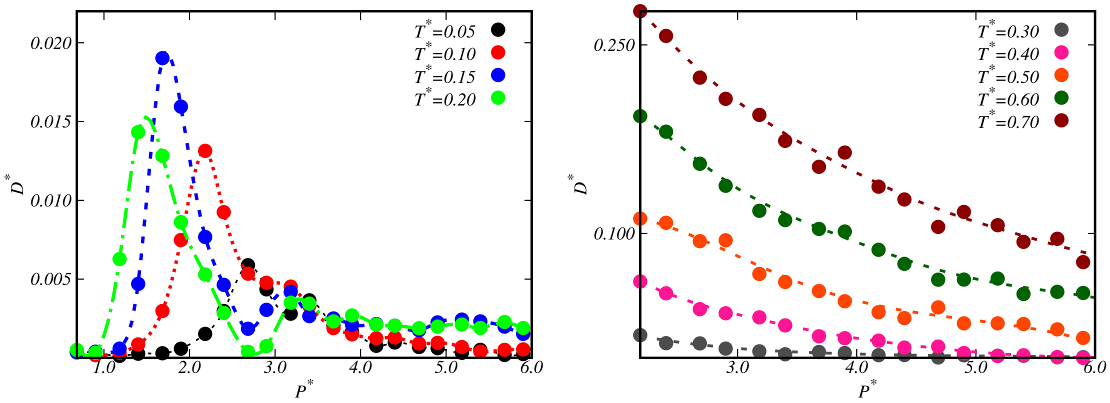

Figure 2-26: Diffusion coefficient versus pressure for (a) $T^* = 0.05$ (black line), $T^* = 0.10$ (red line), $T^* = 0.15$ (blue line), $T^* = 0.20$ (green line) and (b) $T^* = 0.30$ (gray line), $T^* = 0.40$ (magenta line), $T^* = 0.50$ (orange line), $T^* = 0.60$ (green line), $T^* = 0.70$ (brown line).

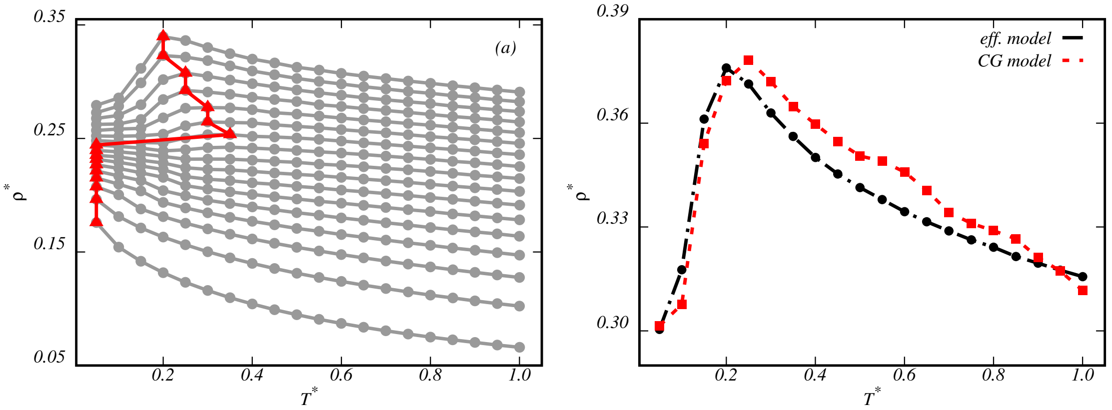

Figure 2-27: (a) TMD line (red line) for distinct isobars in the effective model (b) Comparison of one $\rho(T)$ curve along the isobar $P^* = 2.0$ between the effective (black circles) and the CG model (red squares).

Finally in order to check if the CG model also shows an anomaly, we run simulations along the isobar $P^* = 2.0$. Figure 2-27 (b) illustrates the density versus temperature for $P^* = 2.0$ for both CG (red squares) and effective (black circles) potentials. The two behaviors are quite similar. This result indicates that our strategy to derive a simpler two length scales potential to describe a more sophisticated system obtaining some information about the origin of the anomaly is valid.

Polymer-Grafted nanoparticles where the polymers are free to rotate

The pressure versus temperature phase diagram obtained using the effective potential for the grafted nanoparticles with free polymers is illustrated in figure 2-28. The phase behavior of the system is quite distinct when compared with the phase diagram for the system with fixed polymers.

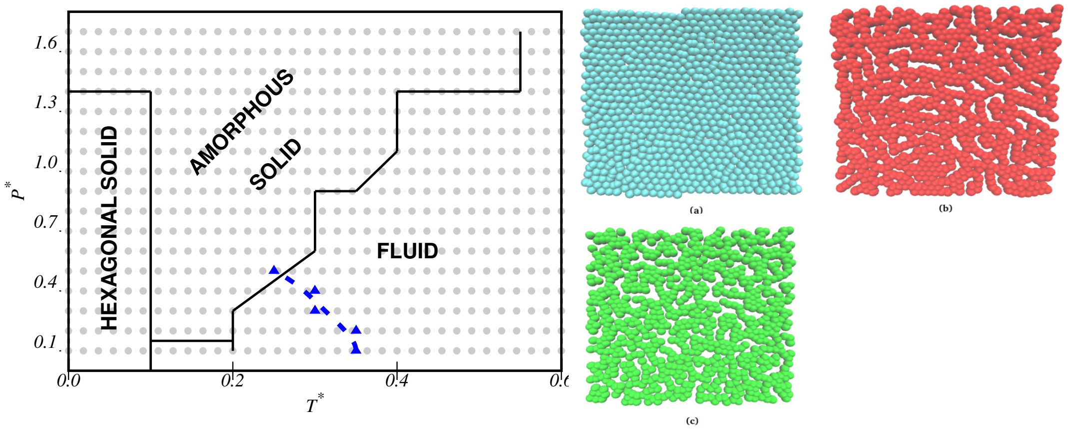

(a) (b)

Figure 2-28: left panel: Pressure temperature phase diagram of system which polymers are free to rotate. The gray dots are the simulated points. The lines divides the distinct phases, I is the hexagonal phase, II is the amorphous solid and the blue line is the TMD. right panel: System snapshots for (a) hexagonal solid ($P^* = 0.40$ and $T^* = 0.05$); (b) amorphous solid ($P^* = 1.10$ and $T^* = 0.10$) and (c) fluid ($P^* = 1.10$ and $T^* = 0.70$).

At low temperatures ($T^* \leq 0.10$) , and for pressures up to $P^* = 1.40$, the system is in a hexagonal solid phase. Increasing the temperature for $P^* < 0.12$, the system melts to a fluid phase, while in the range $0.12 < P^* < 1.4$ there is a order-disorder transition in the solid structure, that changes from the hexagonal to amorphous.

Both free- and fixed-polymer systems show a number of similarities in the phases; here, however, we observe neither a reentrant fluid phase nor the honeycomb solid phase. Also, the solid-liquid separation line moves to higher temperatures. As a result, the TMD line is smaller and there's no diffusion anomaly.

The absence of diffusion anomaly when the system exhibits a TMD is not new. It arises in lattice systems in the presence of two length scales interactions depending of the balance between the two length scales [194] and in confinement due the competition between the length scales and the confinement [195]. In this case, it may be related to the fact that here there is no reentrant fluid region - as we saw, these two phenomena were correlated for the U_{fixed} potential.

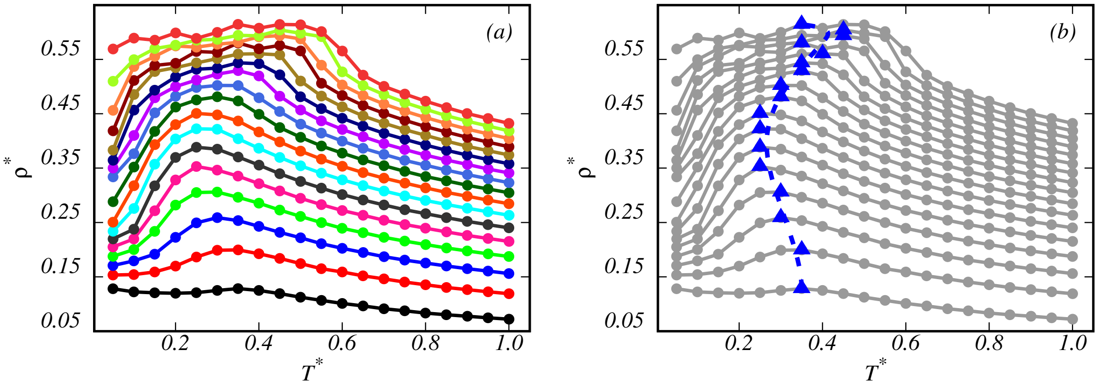

Figure 2-29: Density-temperature phase diagrams. (a) The lines are the isobars from $P^* = 0.10$ (bottom) to $P^* = 1.70$(top). (b) The same diagram evidencing the maximum density temperature (TMD) in blue.

Usually the presence of the TMD, as shown in figure 2-29, is related to a competition between the two length scales, as discussed earlier. However, some studies show that this same phenomenon may occur in fluids without competitive scales: a weak softening of the interparticle repulsion can lead to anomalous behavior. [196, 197].

Therefore, unlike the previous case (U_{fixed}), it is not possible to establish the connection between structure and anomaly in density, as we can see in figure 2-30, which shows behaviour of RDF's by varying temperature (at fixed P^*) and pressure (at fixed T^*). This disconnection can also be analyzed taking into account that the unfilled points of the graph obey the relation between the migration of scales, and that , in turn, the TMD reaches all points (filled or not), it is concluded that, for this potential, it would not be the competition between the scales responsible for the density anomaly, as may seen in figure 2-31. Still, because the potential has a

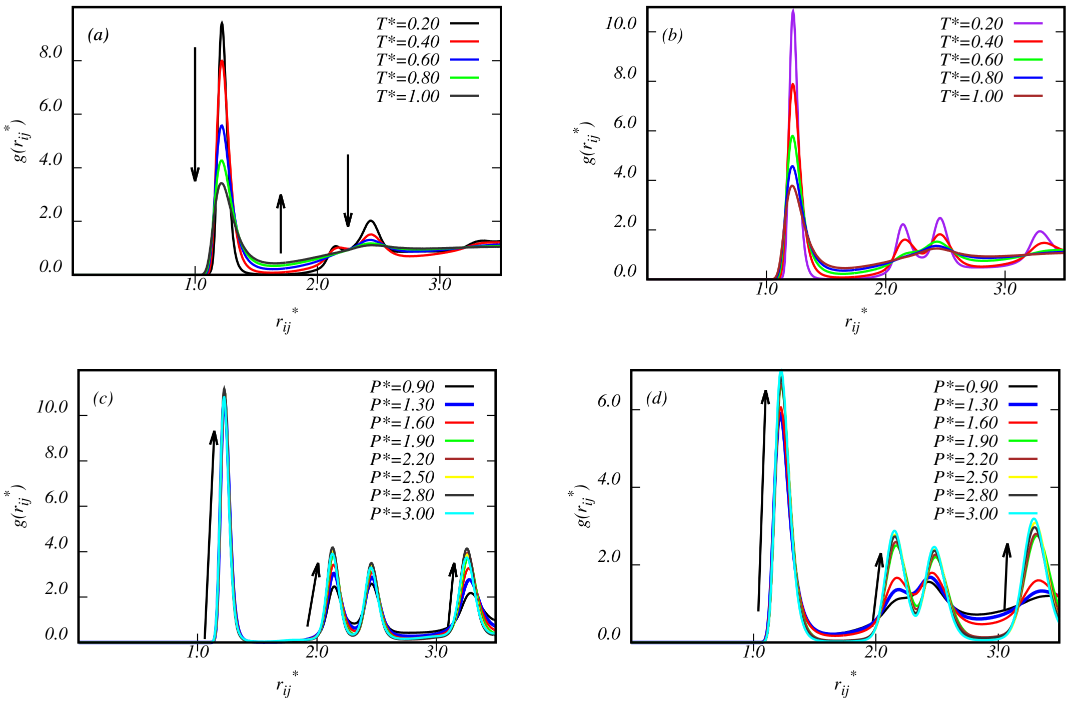

Figure 2-30: Radial distribution function behaviour for maintaining temperature fixed and varying pressure and vice-verse in order to verify relation between competition and structure. (a) $P^* = 0.40$ and each curve is from one temperature. (b)$P^* = 0.80$ analogously. (c) T^* is fixed at $T^* = 0.20$ and pressure is varying. (d)T^* is fixed at $T^* = 0.60$, analogously

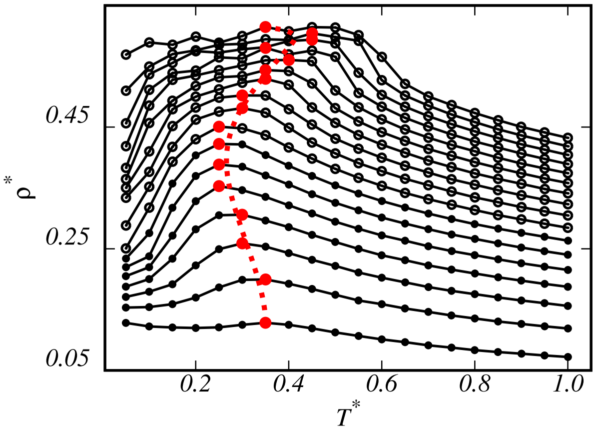

Figure 2-31: Density - temperature phase diagram confirming that's no relation between competition and structure. Filled symbols are dominated by thermal effects, and empty are those dominated by pressure effects.

short range attraction and a long range repulsion (SALR) shape, it was possible to capture some structural patterns (as stripes phase) that had already been observed in potentials of two more abrupt scales [198, 199].

Chapter 3

Water and Tert-Butanol Mixtures

The scientific interest in mixtures springs from the extra degrees of freedom provided by the composition variables, and the consequent diversity of physical behaviour that is possible. These include liquid-liquid and fluid-fluid phase equilibria, in which two dense fluid phases coexist, solvation effects (clustering of molecules of one species about another), and new critical points (consolute points, tricritical points, etc). Mixtures are also of great practical and technological importance. Virtually all naturally occurring fluids are mixtures, and fluid processing in the chemical, oil, food, and pharmaceutical industries involve separation, purification, and reaction of mixtures. An understanding of phase equilibria is of particular importance, but the large number of possible temperatures, pressures, and compositions precludes experimental measurements for all but a few of the possible mixtures of possible interest [16].

The properties of aqueous solutions of hydroxy-compounds are of interest in many fields of enquiry; although much effort has been directed to their study, more is needed fully to solve the problems they present. Among organic compounds, hydroxy-derivatives stand out in virtue of their high solubility in water, but their solutions often show abnormalities in properties, such as viscosity-composition maxima, or negative relative partial molar volumes, which are yet inadequately understood. For monohydric alcohols in dilute aqueous solution, such peculiarities can be attributed in a general way to the bifunctional nature of the solute molecules. The hydrophobic hydrocarbon group may be imagined as resisting the pull into solution exerted by the hydrophilic hydroxyl group, which, either as proton donor or acceptor, can hydrogen-bond with the solvent molecule. A second hydroxyl group in the solute molecule (glycols) shifts the balance of competing influences in favour of "aqueous behaviour" and the anomalies become less marked. Further hydroxylation eventually removes them altogether; thus the sugars are, ostensibly, among the most normal of solutes in water [200].

In this chapter, the first mixture analyzed in this thesis will be treated: water and tert-butyl alcohol solutions. For that, some concepts of water and thermodynamics of the solutions are necessary, which will be described in the next sections.

3.1 Water

Water is a unique, ubiquitous substance that is a major component of all living things: the human body is by weight roughly 75% water in the first days of life and roughly 60% water in the adult age. The majority of this water (roughly 60%) is inside the cells, while the rest (extracellular water) flows in the blood and below the tissues. Many living beings can survive only a few days without water. This is because water participates in the majority of the biological processes [201], such as the metabolism of nutrients catalyzed by enzymes. To be effective, the enzymes need to be suspended in a fluid to adopt their active three-dimensional structure. The main reason why we need water is that it allows the processes of elimination of cellular metabolic residues. It is through the water that our cells can communicate and that oxygen and nutrients can be brought to our tissues [202]. Its nature and properties have intrigued philosophers, naturalists and scientists since antiquity. Some of water's unique properties are literally essential for life, while others have profound effects on the size and shape of living organisms, how they work, and the physical limits or constraints within which they must operate [203]. The more recent discipline of computer simulation has also played a role, having achieved a level of sophistication in the study of water in which it can be used to interpret experiments and simulate properties not directly accessible by experiment. Many of water's basic physical properties can now be explained, at least semiquantitatively, in molecular and structural terms.

The ability to form up to four hydrogen bonds (H-bonds), in addition to the non-directional interactions seen in simple liquids, leads to many unusual properties such as increased density on melting, decreased viscosity under pressure, density maximum at 4°C, high surface tension and many more (there are among its 74 anomalies [204] cataloged up to now). If water would not behave in this unusual way it is most questionable if life could have developed on planet Earth. Figure 3-1 shows the temperature dependence of the density (ρ), the isobaric heat capacity (C_P) and the isothermal compressibility (κ_T) that initially decrease with decreasing temperature but, just above the ambient temperature regime, there is a deviation and both the heat capacity and compressibility begin to increase on further cooling [205].

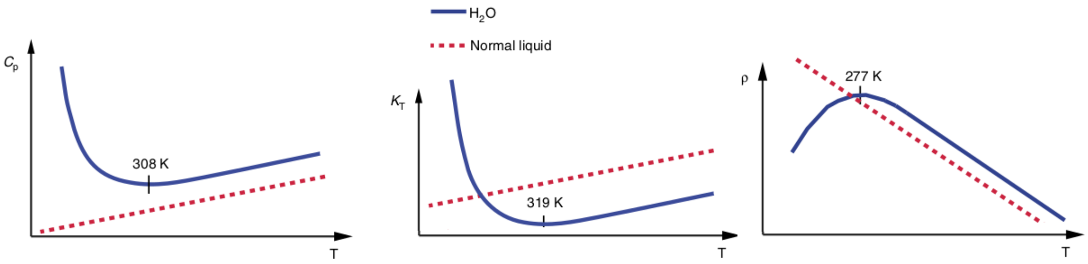

Figure 3-1: Comparison of the density (ρ), isothermal compressibility (κ_T) and heat capacity (C_P) for water (full line) with that of typical liquids (dashed) showing the onset of anomalous behaviour already at ambient temperatures and pressure. adapted from [205].

This myriad of anomalies makes water a great puzzle in regards to the mechanism underlying its weirdness. Interestingly, these anomalous properties become more prominent in its supercooled state, the metastable liquid phase below the melting point [206–208]. In this region, it is still possible to perform measurements in the liquid state until about 232 K, where eventually homogeneous nucleation of ice takes place [209].

The physical properties of water at ambient conditions are in sharp contrast with those of other liquids [211]. As a matter of fact, water presents more than 70 known anomalies [204] that make its behavior unique. For instance, it is long known that water density increases as the temperature grows from 0^{o}C to 4^{o}C at 1 atm [212],

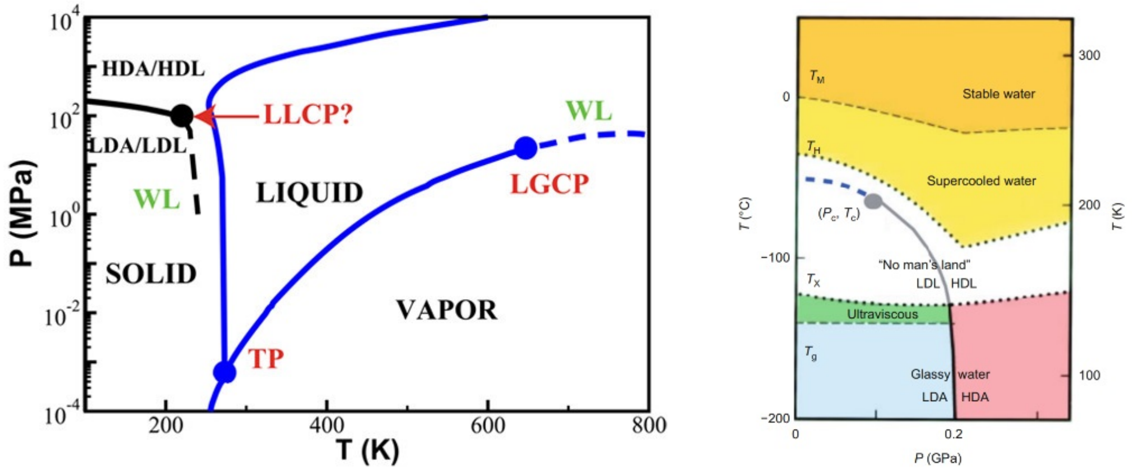

Figure 3-2: (a) Simplified water's temperature-pressure phase diagram portraying its solid, liquid and gaseous phases as well as the hypothetical liquid-liquid coexistence line ending in a critical point, printed from Ref. [207]. (b) A detailed picture regarding the domains of stability and metastability for liquid and glassy water. A first order LLPT line separates HDL and LDL. The LLPT ends with a LLCP at P_c, T_c. T_m , T_g and T_H represent the melting temperature, glass transition temperature, and homogeneous nucleation temperature, respectively. Extracted from Ref. [210].

whereas in most materials heating is associated naturally with the thermal expansion. It has been argued that the presence of second critical point –the liquid-liquid critical point (LLCP)– may be related to water's anomalies. First hypothesized in the seminal work of Poole and co-authors [213], and subject of a recent extensive debate [214–218], from simulation results this point has been estimated to lie withing the so-called no-man's land [219–221]. Due to spontaneous crystallization, there is a lack of direct experimental evidence of the LLPT, and the location of the LLCP remains elusive. Only computer simulations can provide some information in the rather extreme conditions where the LLPT is expected to occur, obviously subject to the limitations of the potential model used [222–226]. From a practical point of view, one can investigate the location of a critical point through an analysis of the the thermodynamic response functions in region above the LLCP. For instance, the isothermal compressibility and hence the correlation length, display a line of maxima in the P-T plane (Widom's line) that typically ends at a critical point with where the maximum evolves into a divergence in the thermodynamic limit [227–232]. Correspondingly, for water in addition to a Widom line ending at the vapor-liquid critical point, there is evidence of a second one that should end at the LLCP [83, 93, 233–237].

3.2 Thermodynamics of Solutions

A large number of chemical processes (most of these, fundamental to the maintenance of life on the planet) are carried in solutions. Solutions are by definition homogeneous mixtures in which n_D mols of a solute D (minor constituent) are dissolved within n_S mols of a solvent S (substance which predominates in a solution) [238, 239]. Although they can be presented in solid, liquid and gaseous states, in this PhD thesis we will be interested with solutions which are in liquid state - mixture of two liquids, which components are miscible in all proportions and in which all components maintain their identity, which means that no chemical reactions occur in a system.

Partial molar quantities

It is natural, when examining the properties of a mixture, try to assess the contributions made by several components. For a more general description of the thermodynamics of mixtures we need to introduce the concept of partial properties: a general partial molar quantity is a partial derivative of an extensive quantity with respect to the amount of one component, keeping T , P, and the amounts of all other components fixed. If the letter Y stands for any extensive quantity (U, H, A, G, S, V , and so on), the partial molar quantity for substance number i is denoted by Y_i and defined by [240–242]

$$\bar{Y_i} = \left(\frac{\partial Y}{\partial n_i}\right)_{T,P,n'} . \tag{3.1}$$

The partial molar function $\bar{Y_i}$ can be used to provide a systematic subdivision of the extensive function Y into a sum of component contributions. Suppose that the amount of each component in the mixture is increased, at constant temperature and pressure, by a factor ξ; THen, because Y is an extensive function,

$$Y(\xi n_1, \xi n_2, ..., T, p) = \xi Y(n_1, n_2, ..., T, p). \tag{3.2}$$

Differentiation of $Y(\xi n_1, \xi n_2, ..., T, p)$ with respect to ξ, followed by setting $\xi = 1$

leads to

$$Y = \sum_{i=1}^{r} n_i \bar{Y}_i. \tag{3.3}$$

Partial molar quantities are intensive properties of the mixture; they depend on T, p and the relative composition of the mixture. A differential change in the extensive property Y, at constant temperature and pressure, is given by

$$dY = \left(\sum_{i=1}^{r} n_i d\bar{Y}_i \right)_{T,p} + \left(\sum_{i=1}^{r} \bar{Y}_i dn_i \right)_{T,p}. \tag{3.4}$$

Comparison of Eqs. 3.4 and 3.3 leads to constraint on the possible changes of the several $\bar{Y}_i$, namely,

$$\left(\sum_{i=1}^{r} n_i d\bar{Y}_i \right)_{T,p} = 0. \tag{3.5}$$

In general, then, the possible changes in the partial molar properties of a mixture satisfy, individually, Gibbs-Duhem type equations of constraint.

Partial molar volume

Imagine a vessel isolated from the surroundings and consisting of two parts separated by a diathermal wall [243]. The parts are occupied by two different gases. For simplicity, we assume that both gases are very dilute so they can be considered ideal gases. Each gas is in thermodynamic equilibrium. We also assume that the temperature and pressure in both parts are the same. Then we remove the dividing wall. What will happen? Although the temperature and pressure will not change, according to the second law of thermodynamics, the system will reach a new equilibrium state of higher entropy. Why does the entropy of the system increase? We know from experience that the gases will not stay in their parts of the vessel but will mix. Due to the process of mixing each component fills the whole volume of the vessel. The process is irreversible, hence, the entropy of the system must increase. The new equilibrium state corresponds to a homogeneous gas in which both components are mixed up on a molecular scale.

And what will happen if we use liquids instead of gases? We know from experiment that some liquids mix in arbitrary proportion, as gases do, although the process of mixing is slower than in gases. Other liquids mix only in certain proportion. Besides, mixing of liquids involves some effects that are absent in gases. For instance, when two liquids mix at constant temperature and pressure their total volume before and after the mixing is different, in general. A good example is the mixture of liquid water and ethanol. The molar volume of water amounts to 18 $cm^3 \cdot mol^{-1}$. If we mix one mole of water with a much larger amount of ethanol, of the volume V, then the volume of the mixture amounts to about $V + 14cm^3$, instead of $V + 18cm^3$. This is because in strong dilution almost each water molecule is surrounded by ethanol molecules. The network of hydrogen bonds that normally hold H_2O molecules at certain distances from each other in pure water does not form. The packing of the molecules in the mixture results in the H_2O molecules increasing the volume by only $14cm^3$. The quantity 14 $cm^3 \cdot mol^{-1}$ is the partial molar volume of water in pure ethanol [244]. In general, the partial molar volume of a substance A in a mixture is the change in volume per mole of A added to a large volume of the mixture (fig. 3-3).

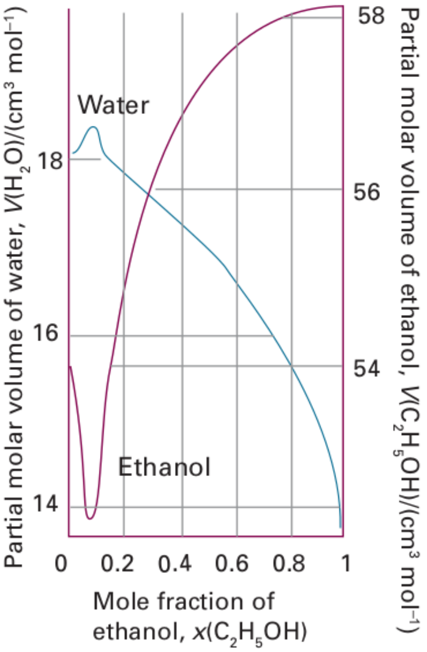

Figure 3-3: The partial molar volumes of water and ethanol at 25°C[244].

For a binary solution of n_1 mol of 1 and n_2 mol of 2 in a total volume V at constant temperature and pressure, we mix δn_1 mol of 1 and δn_2 mol of 2, and repeat this procedure as many times as needed while keeping the ratio $\delta n_1/\delta n_2 = n_1/n_2$ the same for each addition. Then, since the partial molar volumes $\bar{V}_1$ and $\bar{V}_2$ depend only on the relative composition for fixed T and P, adding up all increments in volume gives

$$V = n_1\bar{V_1} + n_2\bar{V_2}, \tag{3.6}$$

which is just a special case of Eq. 3.3.

The determination of partial molar properties from molar mixture quantities is based on the following transformation of Eq. 3.1. Let Y_m be the mean molar value defined by

$$Y_m = \frac{Y}{\sum_i n_i} = \sum_i x_i\bar{Y_i}. \tag{3.7}$$

Consider a binary mixture, and differentiate Y_m with respect to the mole fraction of component 1:

$$\begin{aligned}
\left(\frac{\partial Y_m}{\partial x_1}\right)_{T,p} &= \left(\frac{\partial\left[x_1\bar{Y_1} + (1-x_1)\bar{Y_2}\right]}{\partial x_1}\right)_{T,p}, \\
&= \bar{Y_1} - \bar{Y_2} + x_1\left(\frac{\partial\bar{Y_1}}{\partial x_1}\right)_{T,p} + x_2\left(\frac{\partial\bar{Y_2}}{\partial x_1}\right)_{T,p}, \\
&= \bar{Y_1} - \bar{Y_2},
\end{aligned} \tag{3.8}$$

the last line following from an application of Gibbs-Duhem equation. Combining the two previous equations leads to

$$\begin{aligned}
\bar{Y_1} &= Y_m - x_2\left(\frac{\partial\bar{Y}_m}{\partial x_2}\right)_{T,p}, \\
\bar{Y_2} &= Y_m - x_1\left(\frac{\partial\bar{Y}_m}{\partial x_1}\right)_{T,p}.
\end{aligned} \tag{3.9}$$

The Eq. 3.9 will be used in the next chapter when we analyze the behavior of the partial molar volume of aqueous TBA solutions.

Excess functions

Many phenomena that occur in liquid or solid mixtures can be explained by means of a certain idealization of a real system, called the ideal mixture or ideal solution.

In the ideal mixture, as in the mixture of ideal gases, the only effect of mixing is an increase in the entropy of the system caused by an increase in the volume available to each component. When can we apply the ideal mixture approximation to real mixtures? Usually we can do so if the molecules of different components are similar in respect of size and inter-molecular interactions. By a similarity of interactions we understand that the interaction of two molecules does not depend much on whether they are molecules of the same component or different components. Then, each molecule is always in a similar environment irrespective of whether it is a pure substance or a mixture of similar components [243].

In this way, we can often use the concept of an ideal solution to reduce the labor needed to compute property values for real mixtures. To do so we introduce, for each property f, an excess property f^E ,

$$f^E(T, P, x) = f(T, P, x) - f^{id}(T, P, x). \tag{3.10}$$

Here f represents an property value for the real mixture (which can be any thermodynamic function), and all three terms in 3.10 are at the same temperature T, pressure P, composition x, and phase. The excess properties provide a convenient way for measuring how a real mixture deviates from an ideal solution. In general, an excess property f^E may be positive, negative, or zero. An ideal solution will have all excess properties equal to zero. Note that the value for f^E depends on the choice of standard state used to define the ideal solution. Further note that the definition 3.10 is not restricted to any phase: excess properties may be defined for solids, liquids, and gases, although they are most commonly used for condensed phases [245].

Relations between excess functions exactly the same as those between the total functions [246]:

$$H^E = U^E + PV^E, \tag{3.11}$$

$$G^E = H^E - TS^E, \tag{3.12}$$

$$A^E = U^E - TS^E. \tag{3.13}$$

The excess enthalpy and volume are both equal to the observed enthalpy and volume of mixing, because the ideal values are zero in each case. Figure 3-4 shows two examples of the composition dependence of molar excess functions. In Fig. 3-4(a), the positive values of H^E indicate that the $A-B$ interactions in the mixture are weaker than the $A-A$ and $B-B$ interactions in the pure liquids (which are benzene and pure cyclohexane). The symmetrical shape of the curve reflects the similar strengths of the $A-A$ and $B-B$ interactions. Figure 3-4(b) shows the composition dependence of the excess volume, V^E , of a mixture of tetra-chloroethene and cyclopentane. At high mole fractions of cyclopentane, the solution contracts as tetrachloroethene is added because the ring structure of cyclopentane emerges in inefficient packing of the molecules but, as tetrachloroethene is added, the molecules in the mixture pack together more tightly. Similarly, at high mole fractions of tetrachloroethene, the solution expands as cyclopentane is added because tetra-chloroethene molecules are nearly flat and pack efficiently in the pure liquid but become disrupted as bulky ring cyclopentane is added [244].

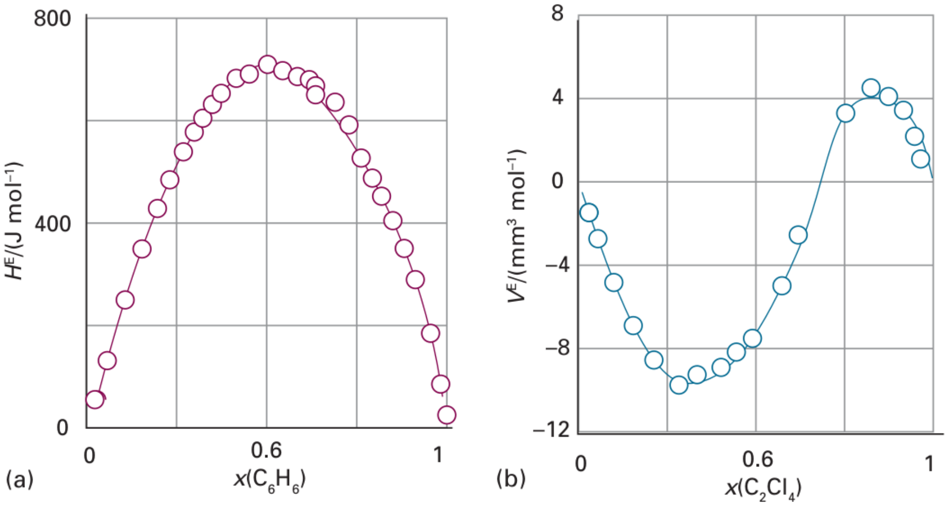

Figure 3-4: Experimental excess functions at 25°C. (a) H^E for benzene/cyclohexane; (b) The excess volume, V^E, for tetrachloroethene/cyclopentane [244].

Solute influence in thermodynamic anomalies of solutions

From a fundamental perspective the study of dilute short chain alcohol solutions is of utmost importance, being the simplest systems that illustrate the interplay of hydrogen bonding and hydrophobicity in amphiphilic substances. In particular, their thermodynamics is known to exhibit quite a few characteristic features, such as the presence of maxima in the excess specific heat [200, 247], minima in the excess volume [248] and negative excess entropy [249]. Some of the anomalies found in these systems are in close connection with the more than seventy anomalies present in water, among them, the presence of a density maximum at $3.98°C$ and $1bar$ in liquid water [250].

The way in which solutes modify the anomalous properties of water is not yet completely understood. In this respect, concerning the density anomaly, solutes can be classified into two groups, namely "structure-makers" (as they increase the TMD when added to water) or "structure-breakers" (decrease the TMD) [251, 252]. It has been found that solutes whose molecules do not join the hydrogen bond network, such as electrolytes [253], room temperature ionic liquids [254], or polar substances without H-bond active groups [255] (e.g. acetone, acetonytrile, tetrahydrofurane, among others) induce a decrease of the TMD. They can all be cast into the group of "structure-breakers". In contrast, dilute solutions of hydrogen bond forming substances with relatively small non-polar tails, such as short-chain alcohols [256] and some amines [14], exhibit an increase of the TMD with respect to pure water. This substances are thought to enhance the structuring of the tetrahedral low density phase of water, and thus are "structure-makers".

Therefore, the study of the thermodynamics of aqueous alcohol solutions has attracted a good amount of research since long [200, 255]. Having both hydrophilic and hydrophobic functional groups, alcohols are the simplest amphiphilic molecules. For this reason, exploring their behavior in water solutions can provide an invaluable insight on the role of hydrophobic and hydrophilic interactions in biophysical processes. As a matter of fact, those are thought to be the main actors in essential phenomena such as protein folding [257].

Particular interesting are short chain monohydric alcohols that are completely miscible with water: methanol, ethanol, propanol and tertiary butyl alcohol (TBA). Their solutions preserve the well known anomalous behavior of water [258–261] (temperature of maximum density, pressure of maximum self-diffusion ...) up to a certain concentration for which the anomalies are destroyed, typically around $x_{R-OH} \sim 0.05$, [262–264]. Interestingly, short chain alcohols are unique among solutes in the fact that the anomalous behavior is even enhanced [265, 266] by their presence in small amounts. Thus one finds that the temperature of maximum density exhibits an increase with respect to that of pure water that in the case of TBA reaches a maximum value for $x_{TBA} \sim 0.005$ [265].

The thermodynamic anomalies of alcohol-water mixtures originate from the corresponding anomalies of pure water [213, 267]. Of special relevance is the volume contraction of pure water that occurs with increasing temperature until a maximum density is reached around $4°C$ along the atmospheric pressure isobar. The existence of this temperature of maximum density (TMD) is probably the best known singularity of water, studied already since the 17th century [268]. Its microscopic origin is based on the prevalence of the formation of low-density ice-type structures over the high-density close-packed configurations right after melting. Solutes that promote a more stable hydrogen-bond network would enhance the anomalous behavior (raise the TMD), whereas those that tend to weaken it would have the opposite effect. This actually bring us back to the "iceberg model" introduced in the forties by Frank and Evans [269] to analyze the solvation of hydrophobic solutes. According to the "iceberg model", the presence of a hydrophobic solute (in the case of alcohols the alkyl chain) would induce the reorganization of the surrounding water molecules with an ice-like structure, which in turn would imply an enhancement of the water anomalies (e.g. a rise in the TMD). These solutes were originally termed "structure makers", in contrast with those that tend to destroy ice-like structures (e.g. hydrophilic groups), termed "structure breakers" [251, 252]. This view has been supported to some extent by the simulation study of Galamba [270].

Since the original contributions of Wada and Umeda in the early sixties [265, 266], a number of works have addressed the issue of the solute's influence on the TMD of water in the case of short chain alcohols [256, 271–277]. Among these, it is worth mentioning the statistical mechanical model of Chatterjee et al. [274]. This model predicts an increase in the TMD with the hydrophobic character of the solute (in this particular case, molecular size) and a decrease with the hydrophilic character (solute-solvent attraction), in apparent agreement with the experimental outcomes of Wada and Umeda [265]. The solute mole fraction for the maximum of the shift in the TMD is, however, larger than the experimental result. This idea proposed by Chatterjee et al. was later applied to a simplified dimer molecule where the effect of hydrogen bonding is modeled with a two scale potential[275]. In this case, the presence of the solute decreases the TMD. In contrast, another two-length scale potential dimer model proposed in Ref. [277] displayed a behavior in accordance with the experimental data, but for artificially low densities. On the other hand, atomistic simulations using either united atom models OPLS for methanol [276], or the very recent simulation work for alcohol/water solutions using flexible all-atom models for methanol, ethanol, propanol, and tert-butanol together with TIP4P/2005f water[278], all fail to reproduce the enhancement of the density anomaly for small alcohol concentrations. In all instances the presence of alcohol molecules induces a substantial decrease of the TMD (up to five times larger than the experimental one for concentrations $x_{R-OH} \sim 0.01$).

3.3 Model and simulation details

We will focus on tert-butanol(TBA) aqueous solutions here, which are of considerable interest due to the presence of marked thermodynamic anomalies [279, 280]. For instance, highly diluted TBA solutions exhibit the most significant increase of the TMD among all short chain alcohols. Moreover, it is the highest molecular mass alcohol to be completely miscible with water in all proportions under ambient conditions [281]. A possible origin of the anomalies has been attributed to the formation of clathrate-hydrates [282], which fits well within the "iceberg model" picture. Our results will provide further evidence in this direction.

From a computational standpoint modeling TBA/water solutions poses a considerable challenge. The bulky alkyl group of TBA is known to be responsible for the formation of molecular emulsions [262], which for certain concentrations are actually equivalent to a microphase separation, in which two intertwined regions of alcohol and water are separated at the microscopic level. Accounting for these structural effects implies lengthy simulations and extremely large samples. In addition, from the results of Ref. [278] we know that even optimized all-atom models do not seem capable of reproducing the experimental density anomalies. Therefore, here we have chosen a simpler model that can account for the structural order due to the presence of highly directional hydrogen bonds, namely, the Stillinger-Weber potential, which is characterized by the presence of a strongly directional thee-body component that favors tetrahedral coordination [283]. This was first used to model water by Molinero and Moore [284] without explicitly accounting for hydrogen atoms. Hereafter, we will denote this interaction as mW potential. We represent TBA molecules using a two-site model, in which the alkyl group is a Lennard-Jones center, and the hydroxil group site interacts with other hydroxil groups via a modified mW potential. Hydroxil/tert-butyl interactions are plain LJ potentials. The tert-butyl site and hydroxil sites are 1.836 Å apart, in agreement with the geometry parameters of Kusalik et al. three-site model [285]. Water will be modeled using strictly the original mW potential, and the cross interaction between water and TBA's hydroxil group also accounted for by a modified mW potential. A Lennard-Jones potential is used to model the interaction between the alkyl group and water. The presence of this interaction appropriately tuned leads to an approximately correct number of hydrogen bonds around the alcohol's hydroxil group. The parameters for the TBA-TBA interaction are tuned to reproduce qualitatively the experimental density and vaporization enthalpies, at least to a comparable level as those of the atomistic models of Kusalik et al. [285, 286].

Using extensive Molecular Dynamics (MD) simulations, we will show that our simple model captures the increase of the TMD of water upon addition of small amounts of TBA. Besides, we have performed a local structure analysis for a series of temperatures above, at and below de TMD using Nguyen and Molinero's CHILL+ algorithm [287]. This algorithm allows for an identification and quantification of ice like, clathrate, and liquid like structures in a series of configurations of water molecules. This analysis was run on configurations of our dimer TBA model solution and of the all atom flexible model of Ref. [278]. In this way, we have been able to provide a clear correlation between the structural reorganization at the microscopic level and changes in the TMD. Also, one can get some insight as to why all-atom models to date do not seem capable of reproducing the subtle effects that the presence of alcohols have on the density anomaly.

Our model coarse-grains the three water molecule atoms into a single site, the mW model, and the fifteen TBA atoms to our two-site model, as depicted in Figure 3-5 in which all the interactions involved are indicated by straight lines. In order to denote the pair site-site interactions, sites are labeled as follows: tert-butyl (TB) as 1, hydroxyl (OH) as 2 and water as 3.

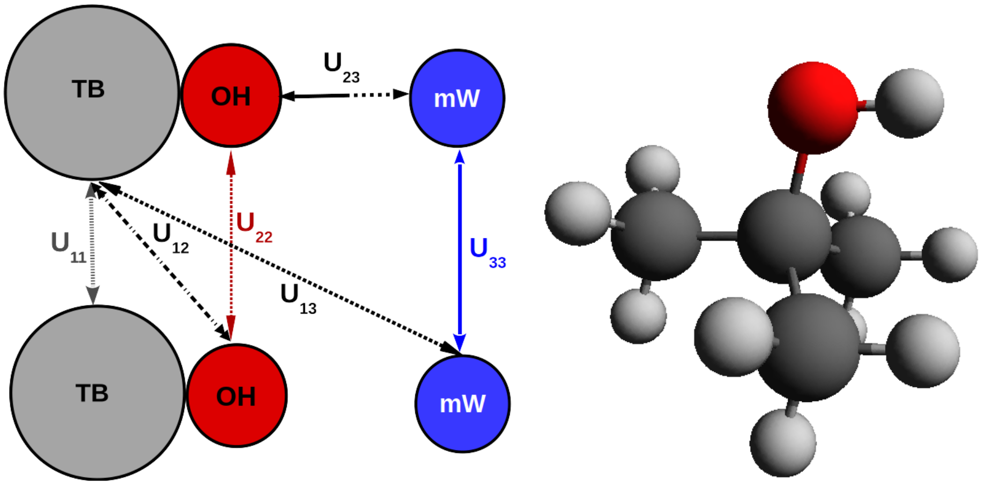

(a) (b)

Figure 3-5: (a) Our TBA and water models and their interactions. TB denotes the tert-butyl group, hydroxyl group is represented by the OH site, and mW indicates a one-site water molecule modeled with the mW potential [284]. (b) All-atom pictorial representation of the tert-butyl alcohol molecule.

<table>
<tr><th colspan="6">Water-Water Interaction Parameters</th></tr>
<tr><td>ϵ</td><td>σ</td><td>a</td><td>λ</td><td>γ</td><td>$cos(\theta_0)$</td></tr>
<tr><td>6.189</td><td>2.3925</td><td>1.80</td><td>23.15</td><td>1.20</td><td>-0.3333333</td></tr>
<tr><td colspan="2">A</td><td colspan="2">B</td><td>p</td><td>q</td></tr>
<tr><td colspan="2">7.049556277</td><td colspan="2">0.6022245584</td><td>4.0</td><td>0.0</td></tr>
</table>

Table 3.1: Parameters of the water-water interactions represented by the Moore and Molinero [284] model.

Water Model

First, for describing the single site water molecule we employ the mW model [284]. It was devised to tune Stillinger-Weber's potential, originally designed for Silicon [283], to reproduce a collection of macroscopic properties of water, preserving the tetrahedral coordination of oxygen atoms in ice [288]. The model is a coarse-grained representation of water molecules in which only effective oxygen-oxygen interactions are accounted for. It has two- and three-body contributions of the form

$$U_{33}(r) \;=\; \sum_i \sum_{j>i} \phi_2(r_{ij}) + \sum_i \sum_{j\neq i} \sum_{k>j} \phi_3(r_{ij}, r_{ik}, \theta_{ijk}), \tag{3.14}$$

where

$$\phi_2(r) = A\epsilon \left[B \left(\frac{\sigma}{r}\right)^p - \left(\frac{\sigma}{r}\right)^q \right] \exp\left(\frac{\sigma}{r - a\sigma}\right), \tag{3.15}$$

and

$$\phi_3(r, s, \theta) = \lambda\epsilon \left[\cos(\theta) - \cos(\theta_0)\right]^2 \exp\left(\frac{\gamma\sigma}{r - a\sigma}\right) \exp\left(\frac{\gamma\sigma}{s - a\sigma}\right). \tag{3.16}$$

The corresponding mW parameters are collected in Table 3.1. The potential parameters were fitted to reproduce the most significant structural and thermodynamic features of water. On the downside, it over-predicts the amount of tetrahedral order, has a lower melting point and TMD than experimentally measured.

Tert-butanol Model

<table>
<tr><th colspan="7">TBA-TBA Interaction Parameters</th></tr>
<tr><th colspan="5">OH - OH interactions</th><th colspan="2">TB-TB interactions</th></tr>
<tr><td>$\epsilon(kcal/mol)$</td><td>$\sigma(\text{Å})$</td><td>λ</td><td>γ</td><td>p</td><td>$\epsilon(kcal/mol)$</td><td>$\sigma(\text{Å})$</td></tr>
<tr><td>1.50</td><td>2.60</td><td>65.00</td><td>1.2</td><td>5</td><td>0.25</td><td>5.45</td></tr>
<tr><th colspan="7">TB-OH interactions</th></tr>
<tr><td colspan="5">$\epsilon(kcal/mol)$</td><td colspan="2">$\sigma(\text{Å})$</td></tr>
<tr><td colspan="5">0.61</td><td colspan="2">4.03</td></tr>
</table>

Table 3.2: Site-site parameters for TBA-TBA interactions. Cross interaction parameters are computed using the standard Lorentz-Berthelot (LB) combining rules. In the case of OH-OH, all remaining parameters retain the original values of Moore and Molinero [284] found in Table 3.1

.

The tert-butanol molecule illustrated in Figure 3-5 is coarse-grained into a two site model: an apolar tert-butyl site which interacts via a Lennard-Jones potential, U_{11}, with the TB site of other molecules and the hydroxyl group which interacts through a Lennard-Jones potential with TB site of other molecules, U_{12}, and with other OH sites via a Stillinger-Weber potential similar to the mW interaction, U_{22}, in which the three-body terms will account for the hydrogen bonding. In addition, a tert-butyl site will be placed 1.836 Å apart from the hydroxil, building a dimer molecule. This distance is taken from the geometry parameters of Kusalik et al. three-site model [285]. The whole set of parameters are tuned to reproduce qualitatively the experimental density and vaporization enthalpies, at least to a comparable level as those of the atomistic models of Kusalik et al. [285, 286], shown in Figure 3-6, and the radial distribution functions obtained for the three-site and fifteen-site models of Kusalik and coworkers [285, 286], as depicted in Figure 3-7. Cross interaction parameters are calculated with the standard Lorentz-Berthelot combination rules. LJ potentials are truncated at 12.5 Å and long range corrections to the energy and pressure are applied.

The final set of parameters is collected in Table 3.2. Figure 3-6(a) shows that our model for the tert-butanol performs reasonably well for the density when compared

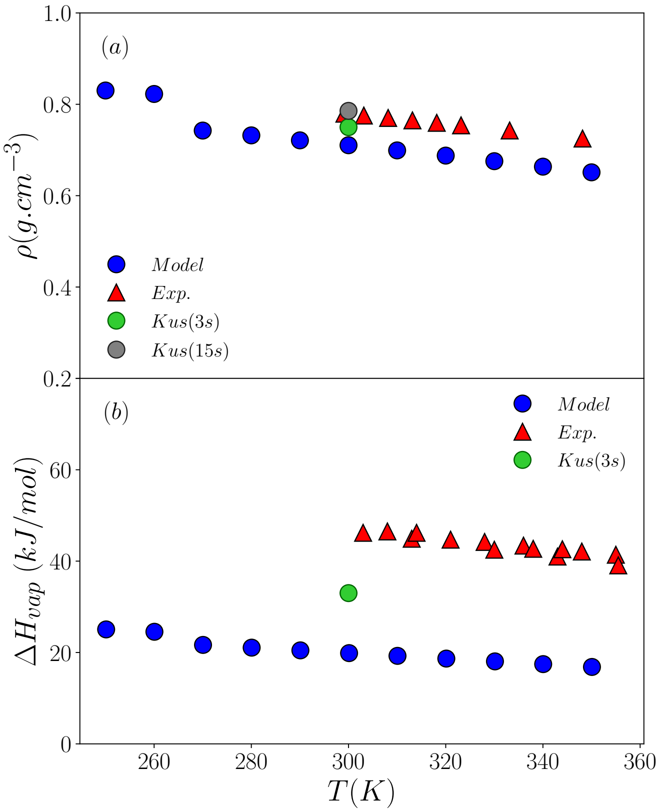

Figure 3-6: (a)Density and (b)vaporization enthalpy of our model in comparison with experimental data [289] and Kusalik models. 3s refers to the 3-site united atom model, and 15s to the fully atomic 15-site one [285, 286].

with the experiments. Actually it presents less than ten percent deviation from the experimental values which compares reasonably well with the four percent departure of the more sophisticated three site model of Ref. [285]. In particular the temperature dependence is correctly reproduced. Deviations in the vaporization enthalpy shown in Figure 3-6(b) are substantially larger when our results are compared with experiments, but in our opinion given the considerable departures exhibited by the more elaborate three site model, they can be deemed acceptable. Note that even for sophisticated water models, vaporization enthalpy is only reproduced when a term to account for the different self-polarization of liquid water are introduced ad hoc [290].

The analysis of the pair distribution functions presented in Figure 3-7 shows that the agreement with the atomistic models is reasonable, being our model logically closer to the three site model when compared with the fifteen site model. This is

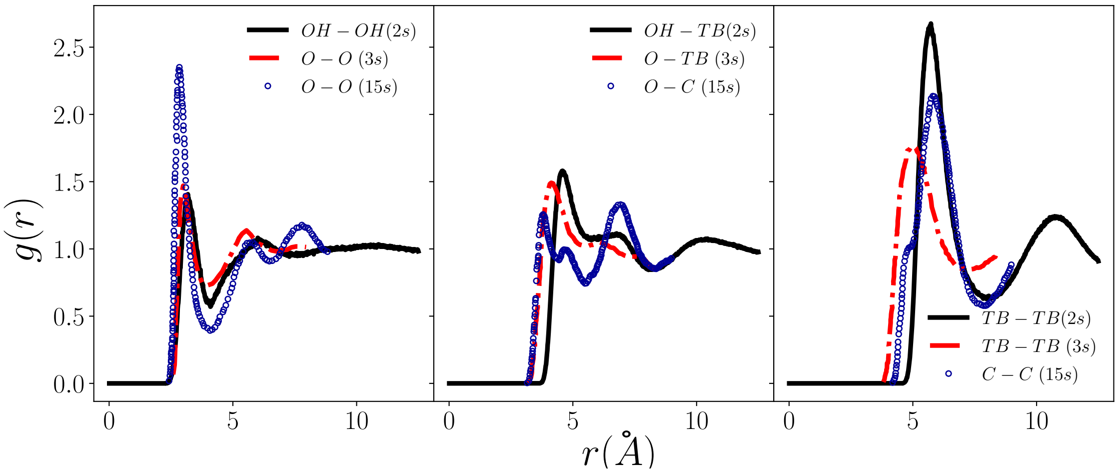

Figure 3-7: Comparison between radial distribution function from our two-site model (2s - continous black curves) and Kusalik et al. two atomistic models for tert-butanol: 3-site [285] (3s - dashed red curves) and 15-site [286] (15s - blue circles).

specially so for the OH-OH and OH-TB partial distributions. Differences between the fifteen site, three site and our model are in any case significant. Not surprisingly, the 15-site model yields pair distribution functions that seem to be in better qualitative agreement with experimental results from neutron diffraction [291]. As to hydrogen bonding, our model gives a coordination number from the integration of g_{OH-OH} up to its first minimum of 2.07 hydrogen bonds, which is somewhat larger than the values 1.62 and 1.77 of Kusalik et al. for three site and 15 site models respectively [285]. Experimental estimates lie in the range from 1.4 to 1.8 [291]. Note that the somewhat stronger hydrogen bonding of our model is due to the large value of the λ-parameter (cf. Table 3.2). Although it is to some extent compensated by the smaller ϵ, it is substantially larger that that of water. This however was necessary to keep the density down to the approximate experimental value, while at the same time keeping the system in the liquid state at 1 bar in the range from room temperature down to the TMD and a bit below. We will see later this has consequences for the fit of the mixture parameters.

Water/Tert-butanol Solution Model

Next, the tert-butyl/water interaction (U_{13}) is modeled via a plain LJ potential truncated at 12.5 Å with long range corrections to the energy and pressure are applied. The OH-water interaction (U_{23}) is again a Stillinger-Weber potential with a three-body component, for which the ϵ and σ parameters have been optimized.

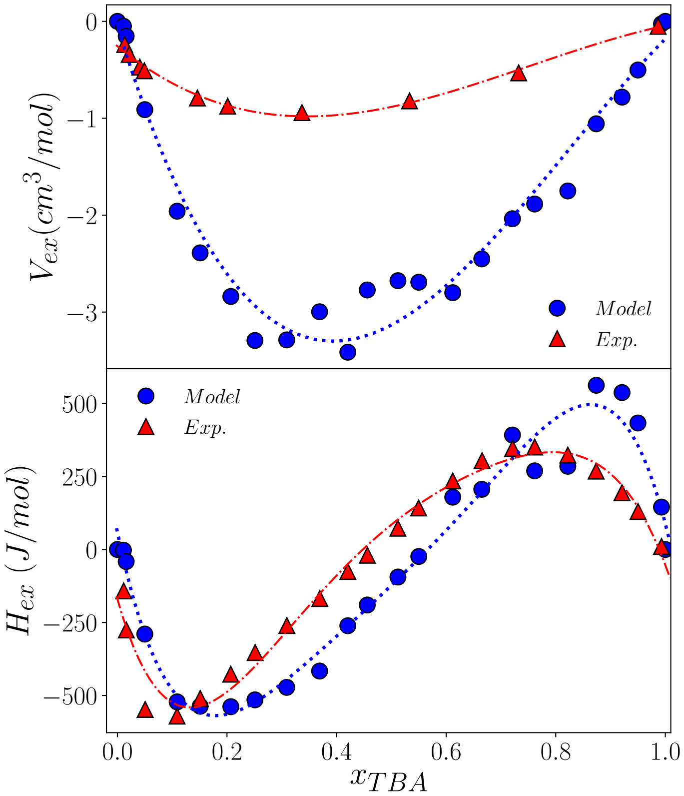

Figure 3-8: Experimental (red) and our model's (blue) excess thermodynamic properties of TBA/water solutions: excess volume (left) and excess enthalpy (right).

These parameters are fixed in terms of excess quantities. The excess quantity is the difference between the value of a given property of the mixture and the corresponding value calculated from those the pure solute and solvent in an ideal mixture. As shown in Ref. [276], excess properties from simulated models can hardly be reproduced if the cross interactions between different molecular components are computed using standard mixing rules. The obvious route to bypass this shortcoming is to adjust these cross interaction parameters to fit the experimental value of the excess properties over the whole composition range. In our case we have used as reference quantities to be fitted the excess enthalpy [292] and excess volume [293]. Given the large value of the λ parameter for TBA-TBA interactions, it seemed at first sensible to use $\lambda_{OH-mW} = \sqrt{\lambda_{OH-OH}\lambda_{mW}}$. This choice however, led to a TMD that decreased monotonously with TBA concentration. For this reason, we decided to keep the value for the hydrogen bond interaction between the hydroxil group of the TBA and water exactly the same as that of pure water, that is, $\lambda_{OH-mW} = 23.15$. We then proceeded to adjust the remaining parameters to the excess properties.

Results from the fit are illustrated in Figure 3-8, and we can see that the model reproduces qualitatively the experimental behavior, both the volume contraction and the non-monotonic compositional dependence of the excess enthalpy, although not as well as the full-atom model [278] . The final fitted parameters are collected in Table 3.3.

TBA-Water Interaction Parameters			
TB-mW interactions		**OH-mW interactions**	
ϵ (kcal/mol)	σ(Å)	ϵ(kcal/mol)	σ(Å)
0.459	3.984	1.371	3.660

Table 3.3: Optimal cross interaction parameters for our TBA-water mixture model. In the case of OH-mW, all remaining parameters take the original values of Moore and Molinero [284] found in the Table 3.1

A snapshot of a configuration for $x_{TBA} = 0.005$ and 252 K along a molecular dynamics trajectory, is depicted in Figure 3-9.

Dimers correspond to TBA molecules, and spheres to water molecules color-coded depending on the geometry of their individual local environment following the classification introduced by Nguyen and Molinero [287] (see Section 3.4 below for a more detailed description of the structural analysis). What it is immediately apparent from the snapshot is that alcohol molecules have certain tendency to aggregate, basically driven by their strong H-bonds. Nonetheless, some free TBA molecules are visible and throughout the whole composition range the system does not phase separate.

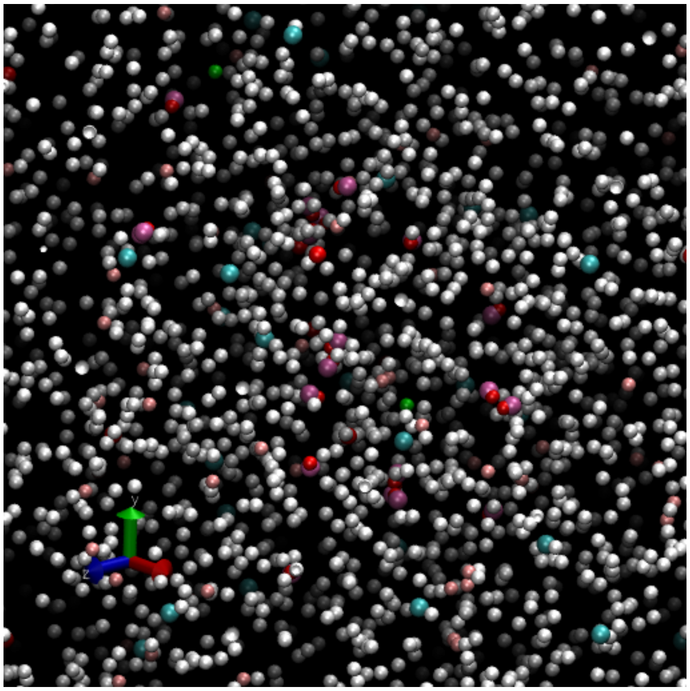

Figure 3-9: Snapshot of a configuration of TBA (red-violet dimers) in water for $x_{TBA} = 0.005$ and T=252K. Spheres of different colors correspond to water molecules in different local environments according to the CHILL+ classification[287], namely liquid-like (white), cubic ice-like (blue), hexagonal ice-like (green), clathrate-like (red), interstitial clathrate (pink) and interfacial ice-like (cyan).

As found by Kežić and Perera [262], all-atom models of TBA aqueous solutions also display a tendency to microsegregate, without reaching a complete phase separation (which is also absent in real TBA solutions).

Simulation Details

Employing the water and tert-butanol models described above we performed MD simulations for a number of systems with particle numbers ranging from 2000 (pure water) to 4000 (pure TBA) for various compositions using the LAMMPS package [188]. Simulations were performed in the isothermal-isobaric ensemble with a Nosé-Hoover thermostat and barostat [42, 294] with a time-step of one fs and relaxation times of 10ps and 100ps respectively. Particles were placed in a cubic box with standard periodic boundary condition. The dimer bonds were kept fixed using a SHAKE algorithm [295], with a tolerance factor of 10^{-4}. Our simulations started from a compositionally disordered mixture of TBA and water particles, which was equilibrated at the chosen pressure and temperature for 2 ns. Production runs were 10 ns long. To ensure that the system was thermalized, the evolution of the pressure, and the kinetic and potential energies were closely monitored during the equilibration run. Configurations were stored every 2 ps and running averages computed every 0.1 ps. Additionally, we have run all-atom simulations using an optimized OPLS-AA model proposed by Jorgensen et al. [296] in combination with a TIP4P/2005f flexible model for water [297] and cross interaction parameters fitted to experimental excess properties [278]. Simulations for pure TIP4P/2005f water were also run. Here we have used the GROMACS package [298, 299] in the isothermal-isobaric ensemble with a time-step of 0.5 fs. Configurations were stored every 2000 time-steps for temperatures approximately at the TMD and some 10K above and below, in order to analyze the structural changes taking place when crossing the temperature of maximum density at constant pressure.

3.4 Results and discussion

Figure 3-10 illustrates density isobars for the water-TBA mixture for various pressures and TBA mole fractions $x_{TBA} = 0.005$ and $x_{TBA} = 0.01$. The dashed curves correspond to third degree polynomial fits. With these fits we obtained the temperature of maximum density denoted by filled pentagons in the graph. As the pressure grows, the TMD decreases in agreement with experimental findings [290]. We observe this behavior for all the mole fractions studied. The origin of the decrease of the temperature of maximum density due to pressure increase can be attributed to the fact that pressure tends to hinder the formation of low density ice-like and clathrate structures by which the anomalous region of water (or water solutions here) is shifted to lower temperatures.

The change in the TMD due to the addition of solute, $\Delta T_{MD}(x_{TBA})$, is a key quantity not only to test if the model reproduces the experiments but also to understand the mechanism behind the unusual increase of the excess of temperature

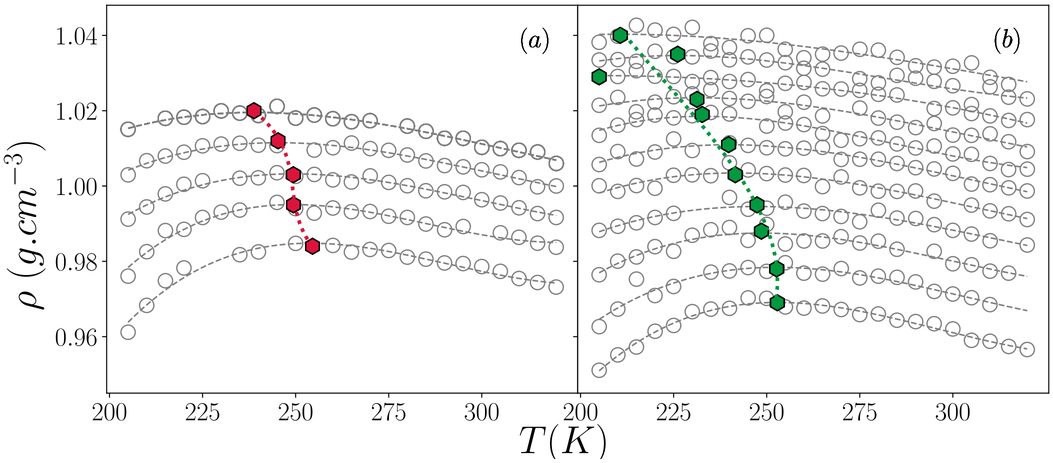

Figure 3-10: Density isobars for pressures, 1 bar, 500 bar, 1000bar,...5000bar (from bottom to top) for TBA in water with $x_{TBA} = 0.005$ (a) and $x_{TBA} = 0.01$ (b). Simulation data are denoted by symbols and lines correspond to a third degree polynomial fit.

of maximum density with the addition of solute. Figure 3-11 compares the ΔT_{MD} versus TBA concentration obtained by our simulations with experiments by de Wada and Umeda [265]. Our model gives the maximum of $\Delta T_{MD}(x_{TBA}) \sim 2$K, for a TBA fraction $x_{TBA} \sim 0.005$ which is approximately the TBA fraction corresponding to the maximum ΔT_{MD} in the experiments. It is readily apparent that our model overestimates the maximum increase of the TMD. For higher TBA concentrations, the curve reaches $\Delta T_{MD}(x_{TBA}) < 0$ for $x_{TBA} \gtrsim 0.01$, a value slightly higher than that of the experimental crossover. For even larger values of x_{TBA}, the excess TMD decreases further, as it does experimentally, up to a point where it is either destroyed (TBA does not exhibit any density anomaly) or preempted by crystallization.

One possible reason for the overestimated value of the maximum $\Delta T_{MD}(x_{TBA})$ is that our model is endowed with stronger hydrogen bonds between TBA molecules than those between water molecules. This effect promotes the formation of TBA clusters with large hydrophobic surfaces. In turn this might enhance the increase in the temperature of maximum density due to the enlargement of the hydrophobic hydration shell.

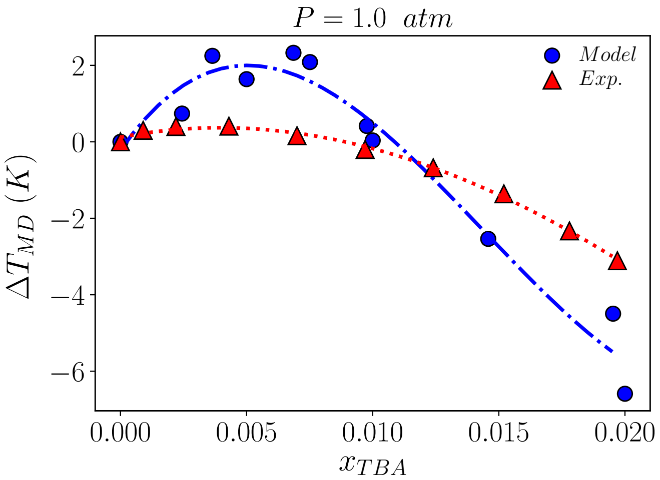

Figure 3-11: Mole fraction dependence of the change in the TMD of water/TBA solutions with respect to that of pure water. Red triangles and dash-dotted curve correspond to our model results, blue triangles and dashed curve denote experimental data.

Partial molar volume analysis

The solute's partial molar volume dependence on temperature and concentration are known to be related to the changes in the TMD (e.g. see Eqs.(24)-(27) in Ref. [300]). This means that a further consistency check of our results can be obtained through their analysis. The relation between TBA partial molar volume, v_{TBA}, and molar volume of the mixture v is described by [301, 302]

$$v_{TBA} = v + (1 - x_{TBA}) \left(\frac{\partial v}{\partial x_{TBA}} \right)_{p,T}, \tag{3.17}$$

that can be expressed at low TBA concentrations using the incremental method [303, 304] as follows:

$$\begin{aligned} v_{TBA}(x_{TBA}) &= \frac{v(x_{TBA} + \Delta x_{TBA}) + v(x_{TBA} - \Delta x_{TBA})}{2} \\ &+ (1 - x_{TBA}) \times \frac{v(x_{TBA} + \Delta x_{TBA}) - v(x_2 - \Delta x_{TBA})}{2\Delta x_{TBA}}. \end{aligned} \tag{3.18}$$

We identify the terms of the interval $(x_{TBA} - \Delta x_{TBA},\ x_{TBA} + \Delta x_{TBA})$ with two consecutive TBA mole fractions. The small difference between consecutive mole fractions makes this method suitable. Figure 3-12 shows the behavior of v_{TBA} with the temperature for four TBA mole fractions around the value of v_{TBA} for which ΔT_{MD} is maximum.

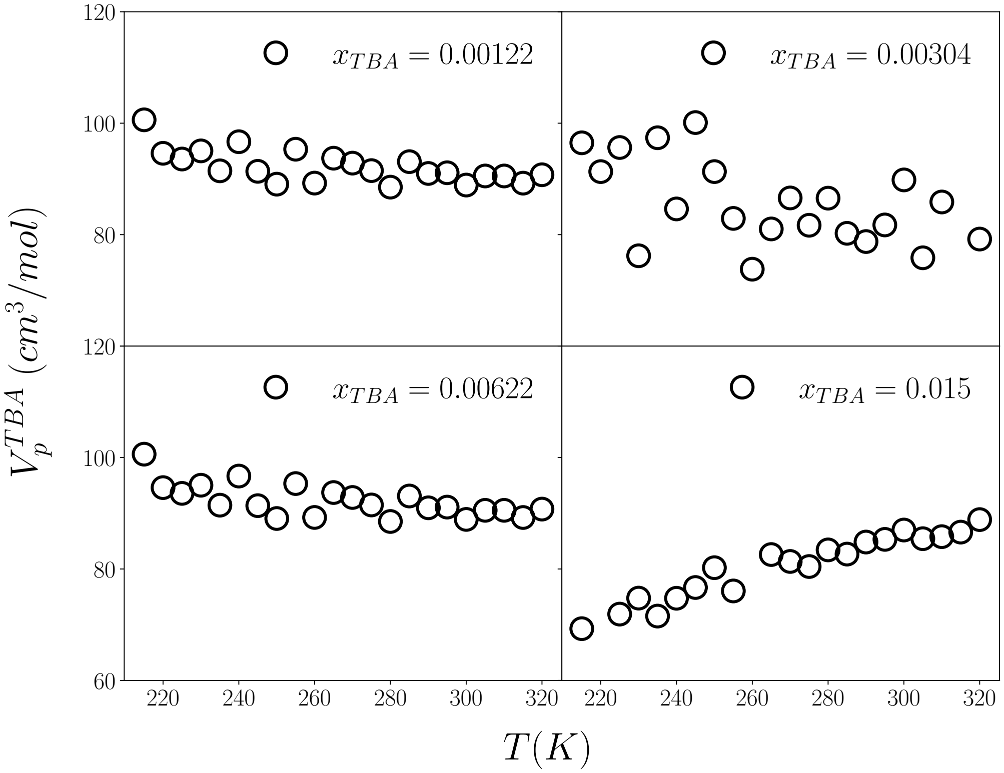

Figure 3-12: TBA partial molar volume v_2 plotted as a function of temperature T for four TBA mole fractions x_{TBA}.

It shows that only for the highest mole fraction analyzed, $x_{TBA} = 0.015$, v_{TBA} increases with temperature. As the mole fraction decreases below $x_{TBA} = 0.015$, the slope of the curve v_{TBA} changes sign (i.e. $(\partial v_{TBA}/\partial T)_P < 0$), indicating the occurrence of the maximum in the ΔT_{MD} close to $x_{TBA} = 0.005$. Figure 3-13 compares the behavior of v_{TBA} versus x_{TBA} at 300K for our model and experimental results [293].

There is a qualitative agreement between our results and the experimental data. Both exhibit a drop in the partial volume of TBA as the concentration decreases at very low TBA mole fractions. In our case, however, the decrease occurs at a higher

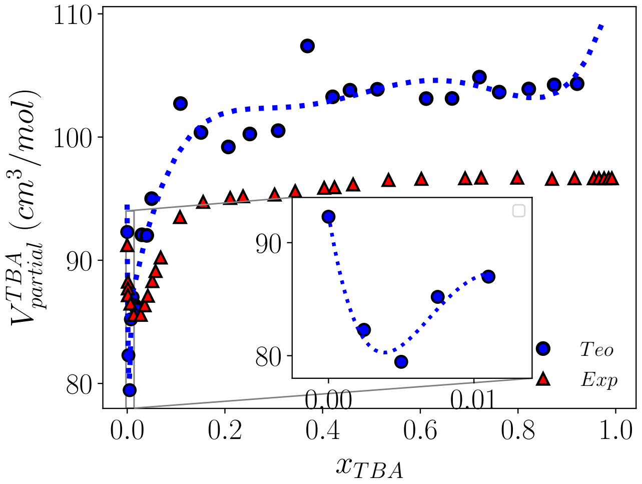

Figure 3-13: The partial molar volumes of TBA as a function of mole fraction x_{TBA}. The derivatives were estimated by a numerical difference. Red triangles are experimental data from [293].

dilution regime ($x \sim 0.005$), which coincides with the maximum we have obtained in the TMD variation (ΔT_{MD}). Such drop beginning from infinite dilution in the partial molar volume with increasing concentration has been observed experimentally and in simulations of water-alcohol mixtures [300, 305–307].

Structural analysis

In summary, our simple model of short chain alcohol displays the "structure maker" character observed experimentally, i.e. a solute that increases the temperature of the maximum density of water. In order to correlate the non-monotonic density dependence of water and water/TBA with microscopic structural changes, we have analyzed a series of configurations from our TBA/water model using Nguyen and Molinero's CHILL+ algorithm [287]. This procedure allows for the identification and quantification of local structures of water molecules depending on the number and configuration of their nearest neighbor bonds. Depending on their relative disposition, bonds are classified as eclipsed and staggered. Then, the algorithm identifies cubic ice-like structures, (no eclipsed and four staggered bonds), hexagonal ice-like, (one eclipsed and three staggered bonds), interfacial ice-like structures, (any number of eclipsed bonds and 2 or 3 staggered bonds), interfacial clathrate-like structures, (three eclipsed and any number of staggered bonds), and finally clathrate like structures, (four eclipsed bonds and no staggered bonds). All other local structures with higher coordinations are cast into the class of liquid-like particles. In any case, it is worth noticing that the lowest density structures correspond to ice-like and clathrates, are all tetrahedrally coordinated. Since the latter corresponds to distorted tetrahedra, they will lead to a slightly higher density: a network of perfect tetrahedra will always yield a more open (less dense) structure. We will see how this is reflected in the TMD. For the sake of comparison we will also perform the same kind of analysis on our own first tentative model with stronger OH-mW interactions, and on the more sophisticated model for water/TBA mixtures with flexible all-atom potentials proposed in Ref. [278]. Both models are unable to reproduce the TMD increase upon TBA addition, and consequently the analysis performed using CHILL+ will illustrate the key differences between models at the microscopic level.

Figures 3-14 show the histograms of relative abundance of local clathrate hydrates (Ct), hexagonal ice (HI), cubic ice (CI), interfacial clathrates (ICt), interfacial ice (II), and liquid water (L) for five models: mW [284] and flexible TIP4P/2005f [297] pure water models –upper graphs– and flexible all-atom TIP4P/2005f-OPLS model of [278] and our TBA/mW model and its variation with stronger water-TBA H-bonding –lower graphs–. Statistical uncertainties are not visible at the scale of the figure.

Focusing first on pure water models, we observe in the upper graphs of Figures 3-14 that only clathrate hydrate structures exhibit a subtle maximum at the TMD for both water models. In the case of the mW water model a maximum is also present in interfacial clathrate structures. Clathrate-like structures are tetra-coordinated oxygen atoms but with eclipsed bonds [287]. As temperature increases, both these and liquid-water structures grow initially at the expense of ice-like structures. Being almost perfectly tetrahedral, ice-like structures are less dense. This explains the initial anomalous increase of density. From the TMD onward, the relative weight of low density structures (clathrate, and ice-like structures both bulk and interface) diminishes considerably, and density decreases due to the regular thermal expansion of the

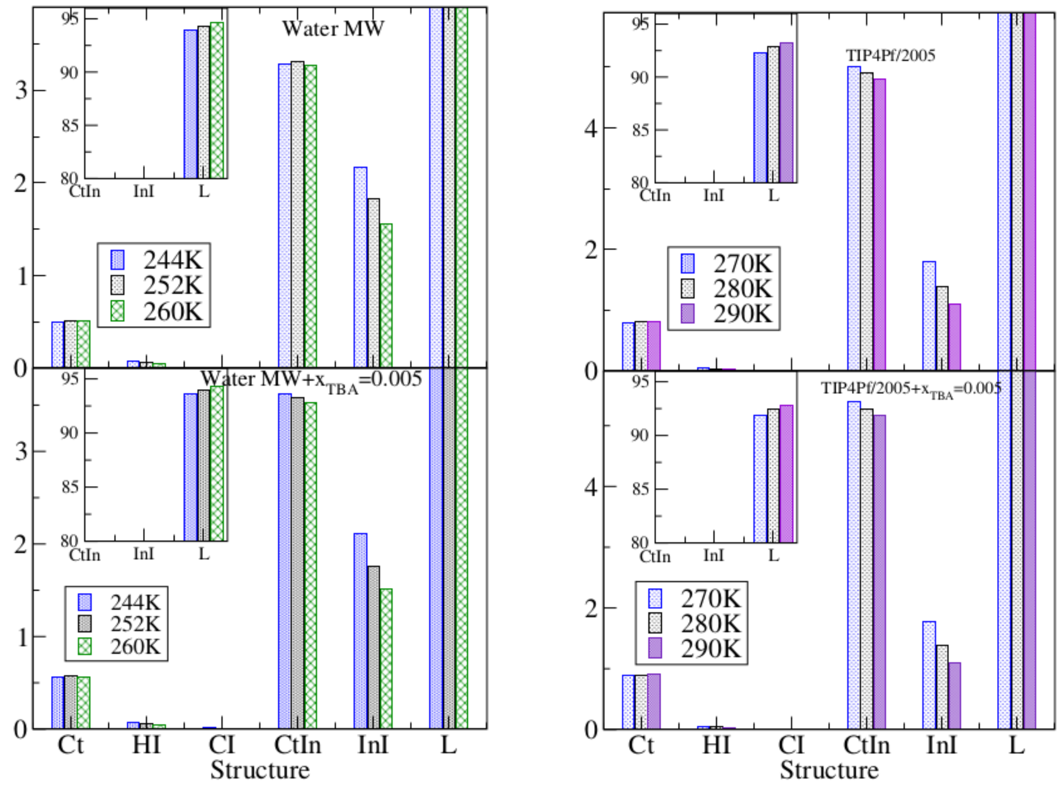

(a) (b)

Figure 3-14: Histograms of relative abundance of local clathrate hydrates (Ct), hexagonal ice (HI), cubic ice (CI), interfacial clathrates (ICt), interfacial ice (II), and liquid water (L), as determined using CHILL+ algorithm[287] on 2000 for (a) Pure mW water (upper graph) and mW water+our TBA model (lower graph). Dashed bars (visible mostly on the clathrate –Ct– data) correspond to our model with stronger OH-mW hydrogen bonds ($\lambda_{OH-mW} = 36$) (b) TIP4P/2005f pure water model (upper graph), and flexible all-atom TIP4P/2005f-OPLS [278] mixture models (lower graph). Notice the vertical dashed lines that separate data with ordinates on the left and right axis.

high density liquid water structure.

Thus, the interplay between a small maximum in low density structures (clathrates) and increase of liquid-like (high density) structures seems to be at the source of the existence of a TMD. All other low density (ice-like) structures have a very small presence after melting, and display a monotonic decrease with increasing temperature. It is important to notice that the clathrate structures occur in both models of pure water, so its existence does not require -although, as shown below, it is enhanced by– the presence of solute molecules.

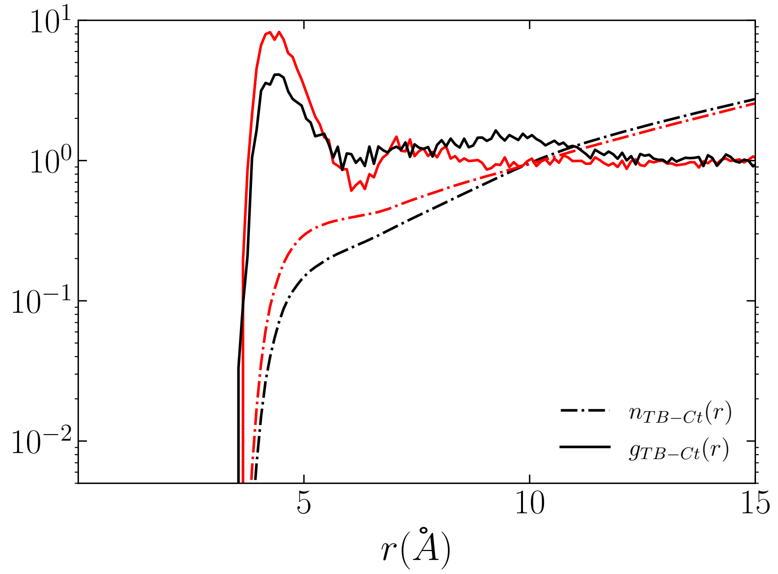

Figure 3-15: Pair correlation functions (solid curves) between tert-butyl sites and water molecules with clathrate-like (Ct) local structures and corresponding integrated r-dependent coordination numbers (dashed curves). In black our present model for TBA-mW water, in red curves corresponding to the model with a stronger OH-mW hydrogen bonding.

Next, in the case of the lower graphs of Figure 3-14 we have the corresponding histograms for the solutions at $x_{TBA} = 0.005$, i.e. close to the maximum of $\Delta T_{MD}(x_{TBA})$ for our model. Our results exhibit again a maximum in the bulk clathrate hydrate structures. Interestingly the maximum does not occur for the interfacial clathrates anymore. In the solution, these structures are basically promoted by the presence of solute molecules, and their relative weight monotonically decreases with temperature. Now, in the TIP4P/2005f-OPLS model the maximum is shifted to temperatures well beyond the TMD, the region shown in the figure displaying a slight increase in the relative weight of the clathrate structures. Also, in our model with stronger water-TBA H-bonds the clathrate-like structures maximum has practically vanished. This implies that in these two cases, as temperature reaches the TMD the number of clathrate structures does not grow appreciably, and consequently the density increase from the melting temperature is smaller, by which $\Delta T_{MD} < 0$. For higher temperatures, above the TMD, the thermal expansion of the dominant liquid-like structures controls the temperature dependence of the density, and thus the water anomaly disappears.

Now, we may ask ourselves where one should expect to find the largest concentration of clathrate-like structures in the presence of TBA solute molecules. To answer this question, in Figure 3-15 we have plotted the pair correlation function $g_{TB-Ct}(r)$ between tert-butyl sites and water molecules with a clathrate-like local environment. In the same graph we also include the corresponding r-dependent coordination number, n_{Tb-Ct}. For our model (black curves)we observe that the first coordination shell reaches up to 5.8 Å, which roughly corresponds to the first hydration shell ($r < 5.4$ Å) [308]. Interestingly, the effect extends moderately up to the second coordination layer, in contrast with the model with a modified stronger H-bonding between TBA and water (red curves). Looking at the integrated coordination numbers, one observes that in our model (which reproduces the experimental rise of the TMD) the number of clathrate like structures is slightly higher since the effect propagates further into the bulk. The tendency of the TBA molecules to aggregate in our solution model leads to the formation of larger clusters with big hydrophobic surfaces and an overgrown hydration shell. This is likely the origin of the overestimation of ΔT_{MD} already commented upon in previous paragraphs.

Finally, in our model, for a larger concentration, such as $x_{TBA} = 0.02$ the density anomaly occurs at very low temperatures, where the large fluctuations in the results are connected with the onset of crystallization and $\Delta T_{MD}(x_{TBA}) < 0$. In this case, the solute behaves now as a strong "structure breaker". We have observed that the maximum in the ratio of bulk clathrate structures is much less marked. Also, the relative weight of interfacial clathrates increases 25 percent with respect to the value for pure water and diminishes with increasing temperature. As in the case of the all-atom model, these structures are promoted by the presence of solute molecules and their relative weight depends on the concentration of the latter. As discussed above, the decrease in the maximum of bulk clathrate structures is directly connected with the fall in the TMD. Larger increases in x_{TBA} will lower the TMD even further, and the density anomaly will be completely preempted by crystallization/vitrification. Apparently, in the all-atom model solution, the shift of the bulk clathrate structure maximum, and in our dimer TBA model the smoothing of the corresponding maxima for concentrations above $x_{TBA} \sim 0.01$ (or when the TBA-water H-bond is stronger that that of bulk water), are the structural features that determine the "structure breaker" character of the solutes. For concentrations below $x_{TBA} \sim 0.01$, our model solute behaves as a "structure maker".

Chapter 4

Water and Short-Chain Alcohol Mixtures

4.1 Introduction

Life, as we known, started and evolved in water solutions. Then, we can say that to understand the complexity of complex molecules in water, at both micro- and macro- levels, is of paramount importance in modern science [301, 309]. The physical properties of aqueous solutions are strongly dependent on the intermolecular interactions, and typically deviate substantially from ideality [27]. In this respect, solvation effects (clustering of molecules of one species around another species) are essential in determining the properties of solutions. Additionally, under certain circumstances, fluid-fluid phase equilibrium (demixing in two dense fluid phases) might even take place [310].

Although the behavior of complex biological proteins in water is a huge and complex problem, with many hydrophobic and hydrophilic sites, we can draw some information from simpler systems. In this way, a special class of aqueous solutions are those containing short-chain alcohols (i.e., alcohols with a small number of carbon atoms in the chain, like methanol, ethanol, or 1-propanol), most of which are miscible in water over the full range of concentrations [311, 312]. They have attracted a great attention of scientific community for decades for a number of reasons: (i) they are ubiquitous in the medical [313], food industries [314], transportation [315] and personal care [316], among others, and thus have attracted much theoretical and experimental attention; (ii) comparatively to water, the molecular structure of alcohols shows the presence of an organic radical in place of one of the hydrogen atoms; as a consequence, alcohols do not form a completely developed hydrogen-bonded network, as in the case of water; (iii) On the other hand, the presence of both the hydroxyl group and the organic radical, usually non-polar (amphiphilic character), allows for the interaction with a huge number of organic and inorganic compounds, making alcohols good solvents, since the solute-solvent interaction can have the same order of magnitude as the solute-solute and solvent-solvent interactions [317]. In addition, (iv) although the interactions with molecules of a dual nature, such as alcohols, involve not only the hydrophobic hydration of the non-polar moiety of the molecule but also the hydrophilic interactions between the polar groups and the water molecules, still they constitute a model for the investigation of the hydrophobic effect [318, 319].

With water as a solvent, both the complexity of analysis and the richness of phenomena observed for such solutions are highlighted, since the physical properties at ambient conditions are in sharp contrast with those of other liquids [211]: water is the most anomalous material, with more than 70 known anomalies [204]. Probably, the most well known is the density anomaly. While most of the materials increases the density upon cooling, liquid water density decreases when cooled from 4^{o}C to 0^{o}C at atmospheric pressure [212]. Recent findings indicated a relation between the anomalies and another unique feature of water: the liquid polymorphism and the phase transition between two distinct liquids [237]. In addition to the usual liquid-gas critical point (whose near-critical properties are so drastically different from those of liquid water [320]), since the 1990s [213] the existence of a second critical point - the liquid-liquid critical point (LLCP) has been hypothesized by simulations and subject of extensive debate [214–218]. It has not yet been reported from experiments once is located in the so-called no-man's land: due the spontaneous crystallization it is (almost) impossible to reach this region by experiments - however, some recent experiments show strong evidence of the existence of the LLCP [219–221]. The LLCP locates at the end of a first order liquid-liquid phase transition (LLPT) line between low-density liquid (LDL) and high-density liquid (HDL) at low temperatures [213, 237, 321–328]. Unlike the liquid–gas phase transition (LGPT), which always has a positive slope of the first-order phase transition line because $\Delta S > 0$ and $\Delta V > 0$ (Clausius–Clapeyron relation), the LLPT line can indeed be either negative or positive, depending on the pair atomic interactions of the model [329]. From a practical point of view, one can investigate the location of a critical point through an analysis of the the thermodynamic response functions in region above the LLCP. For instance, the isothermal compressibility and hence the correlation length, display a line of maxima in the P-T plane (Widom's line) that typically ends at a critical point where the maximum evolves into a divergence in the thermodynamic limit [227–232]. Correspondingly, for water in addition to a Widom line ending at the vapor-liquid critical point, there is evidence of a second one that should end at the LLCP [83, 93, 233–237].

The critical behavior of mixtures has been widely analyzed from both an experimental and theoretical point of view [330–339]. The location of the LLCP can be affected by the disruption of the hydrogen bond (HB) network induced by nanoconfinement [340–343] or the presence of solutes [344–355]. The latter studies mostly focus on either hydrophobic or hydrophilic solutes, from hard spheres to ions. Alcohols, in turn, represent the simplest amphiphilic molecules, with both hydrophilic and hydrophobic sites. This ambivalent behavior is essential to understand the dynamics and structural reorganization of biomolecules in water[257]. Among alcohols, methanol is the shortest molecule, with an apolar methyl group and a polar hydroxyl group. It is fully miscible for all compositions, and methanol molecules are fully integrated in water's hydrogen bond network [356]. These solutions present anomalies in some of their thermodynamic properties, which are strongly dependent on the solute concentration and have thoroughly investigated experimentally and by computational modeling [258, 276, 357–360]. On the other hand, to the best of our knowledge, the influence of concentration of amphiphilic solutes and of the size of the alcohol chain on the liquid-liquid critical region has not being investigated so far. From the experimental point of view, one is likely to find the same insurmountable difficulties as in pure water, and to obtain straight computer simulation answers using realistic potential models is a truly demanding problem.In this way, some questions that arise are: how longer chains of alcohol will affect the behavior of Core-Softened(CS) water in the supercooled regime? How possible changes in the critical behavior can be related to the anomalous behavior? Also, there is some effect in the spontaneous crystallization observed near the LLCP?

To answer this question, we perform extensive simulations to analyze the phase diagram of CS water and water-alcohols mixtures. The success of these simple models stems from the existence of two characteristic length scales in the potential [361]. The competition between microscopic water structures induced by the first or the second length scale is directly related to the presence of anomalies – as the competition between two fluids structures in liquid water [237]. More recently, this core-softened approach has been extended to methanol [362, 363] and water-metanol mixtures [277, 364]. In these models the methanol is modeled as a dumbbell, with a CS site as the hydroxyl-like monomer and a standard Lennard-Jones (LJ) site as the methyl-like monomer. Previous studies have shown that CS-LJ amphiphilic dimmers can exhibit water-like anomalies [365, 366], and have been used to predict a LLCP for methanol [367, 368]. Here, we will focus on how the concentration of core-softened methanol and the size of the alcohol chain on influence the LLCP of a core-softened(CS) water model. In the first work [369], we have explored the supercooled regime of pure water, pure methanol and their mixtures using a core-softened (CS) potential model [309]. In this scheme, hydroxyl groups of different molecules interact by a continuous shouldered well (CSW) potential, while all other interactions are reproduced by LJ-like contributions, and our principal focus in that publication was on the relations between density anomaly, liquid-liquid phase transition and spontaneous crystallization by means of Molecular Dynamics simulations. In the second work, in a similar way to that performed by Urbic et al [370], we extend this scheme to ethanol (CH_3-CH_2-OH) and 1-propanol ($CH_3-CH_2-CH_2-OH$), by modeling such alcohols as linear chains constituted by three (trimers) and four (tetramers) partially fused spheres, respectively, and the primary objective is to complement our previous study by exploring the influence of the size of the solute on the thermodynamic properties of mixtures of core-softened water and alcohols: methanol, ethanol and 1-propanol.

4.2 Model and details of simulation

Our water-like solvent here will be the core-softened fluid in which particles interact with the potential model proposed by Franzese [371]. Water-like particles W_{CS} are represented by spheres with a hard-core of diameter a and a soft-shell with radius $2a$, whose interaction potential is given by

$$\begin{aligned} U^{CS}(r) \quad = \quad & \frac{U_R}{1+exp\left[\Delta(r-R_R)\right]} \\ & -U_A exp\left(-\frac{(r-R_A)^2}{2\delta_A^2}\right)+U_A\left(\frac{a}{r}\right)^{24}. \end{aligned} \tag{4.1}$$

With the parameters $U_R/U_A = 2$, $R_R/a = 1.6$, $R_A/a = 2$, $(\delta_A/a)^2 = 0.1$, and $\Delta = 15$ this potential displays an attractive well for $r \sim 2a$ and a repulsive shoulder at $r \sim a$, as can be seen in figure 4-1(a) (red curve). The competition between these two length scales leads to water-like anomalies, as the density anomaly, and to the existence of a liquid liquid critical point [363, 371, 372].

More recently, Urbic and co-workers proposed the models for our solutes: a dumbbell model for the methanol molecule which consists of a pair of tangent spheres of diameter a, where one monomer is apolar (the methyl group) and corresponds to 24-6 Lennard-Jones (LJ) site, and the other monomer (the hydroxyl group) is a core-softened polar particle, in which the hydrogen bond interaction is accounted for by the second length scale of the potential expressed in equation 4.1. A extension towards ethanol ($CH_3 - CH_2 - OH$) and 1-propanol ($CH_3 - CH_2 - CH_2 - OH$) was done as linear trimers and tetramers, respectively (Fig. 4-1). Trimers are constructed as linear rigid molecules consisting of three partially fused spheres, where two adjacent spheres are placed at fixed distance $L_{ij} = 0.60a$, with a as the unit length. Analogously, tetramers are modeled as linear rigid molecules consisting of four partially fused spheres, where two adjacent spheres are placed at fixed distance $L_{ij} = 0.78a$. In all models, hydroxyl groups interact through a soft-core potential (eq 4.1), while CH_2 and CH_3 groups are nonpolar and interact through LJ-like potential,

$$U^{LJ} = \frac{4}{3}2^{2/3}\epsilon\left[\left(\frac{\sigma}{r}\right)^{24} - \left(\frac{\sigma}{r}\right)^{6}\right], \tag{4.2}$$

$OH - CH_2$ and $OH\breve{}CH_3$ interactions are of LJ type as well. LJ parameters are reported in Table 4.1. Quantities are reported in reduced dimensionless units relative to the hydroxyl group diameter and the depth of its attractive well.

	L_{ij}	ϵ_{1n}	ϵ_{nn}	σ_{1n}	σ_{nn}
Dimers	1.000	0.316	0.100	1.000	1.000
Trimers	0.600	0.400	0.400	1.115	1.230
Tetramers	0.780	0.500	0.500	1.115	1.230

Table 4.1: Potential parameters for dimers ($n = 2$), trimers ($n = 2, 3$), and tetramers ($n = 2, 3, 4$); the OH group is labeled with 1. As for the bond length, $j = i + 1$ [370].

In the mixture, water-like and hydroxyl-like groups also interact via equation 4.1. For the interaction between apolar sites and the polar sites, the Lorentz-Berthelot mixing rules were employed using equation 4.2, as proposed by Urbic[362]. The interaction potentials are shown in figure 4-1(a), and a schematic depiction of the pair interactions and the system constituents is show in figure 4-1(b). All quantities presented hereafter will be reported in reduced dimensionless units relative to the hydroxyl group diameter and the depth of its attractive well: $T^* = k_BT/U_A$, $\rho^* = \rho a^3$ and $P^* = Pa^3/U_A$.

The simulations were performed in the NPT ensemble with a fixed number of molecules ($N_{tot} = 1000$). $N_{alc} = x_{alc}N_{tot}$ is the number of alcohol (methanol, ethanol or propanol) molecules and $N_w = N_{tot} - N_{alc}$ that of water molecules, where x_{alc} is the alcohol mole fraction, which has been varied from 0.0 (pure water) to (i) 1.0 (pure methanol) in case of water-methanol mixtures, and (ii) to 0.01, 0.05 and 0.1 (we've focused in low-concentration range for studies about influence of chain size of

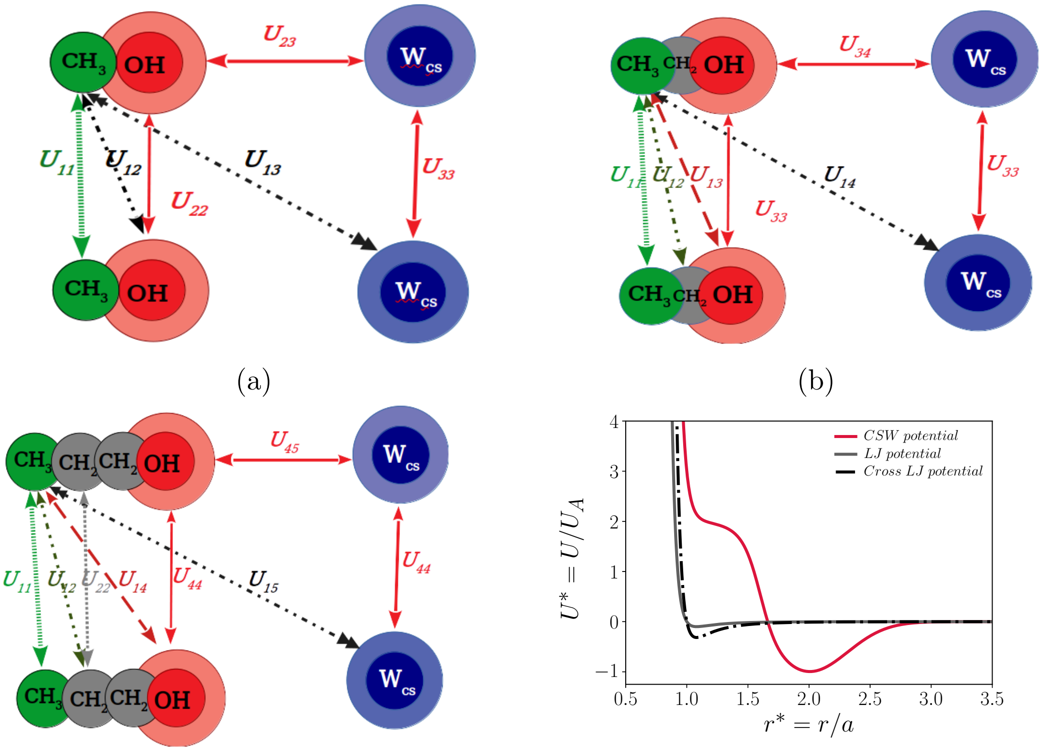

(a)

(b)

(c)

(d)

Figure 4-1: In (a), (b) and (c), our model for methanol, ethanol and 1-propanol is outlined, while in (d) we see the interaction between water and hydroxyl's is described by the CSW potential, while other interactions behave like a 24-6 Lennard-Jones potential.

alcohols). The temperature and pressure were controlled using the optimized constant pressure stochastic dynamics proposed by Kolb and Dünweg [373] as implemented in the ESPResSo package [374, 375]. This barostat implementation allows for the use of a large time step. This was set to $\delta t^* = 0.01$, and the equations of motion were integrated using the velocity Verlet algorithm. The Langevin thermostat [12], that keeps the temperature fixed, has a coupling parameter $\gamma_0 = 1.0$. The piston parameters for the barostat are $\gamma_p = 0.0002$ and mass $m_p = 0.001$. The particles were randomly placed in a cubic box, and then dynamics was run for 5×10^6 time steps in the NVT ensemble to thermalize the system. This was followed by 1×10^6 time steps in the NPT ensemble to equilibrate the system's pressure and 1×10^7 time steps further for the production of the results, with averages and snapshots being taken at every 1×10^5 steps. To ensure that the system temperature and pressure were well controlled we averaged this quantities during the simulations. As well, to monitor the equilibration the evolution of the potential energy along the simulation was followed. Here, the molecule density ρ is defined as $N_m/ < V_m >$ with $< V_m >$ being the mean volume at a given pressure and temperature. Isotherms were evaluated with changing intervals - a finer grid was used in the vicinity of the critical points. In the first study, focused in water-methanol mixtures and how the fraction of methanol affects the TMD and the LLCP, we study pressures from $P = 0.01$ up to $P = 0.70$ along isotherms ranging from $T^* = 0.40$ up to $T^* = 0.64$ upon heating. For the second work, focused on the effects of the alcohol chain length in the polymorphism and TMD, we studied pressures from $P = 0.005$ up to $P = 0.30$ under cooling from $T^* = 0.70$ down to $T^* = 0.20$.

We evaluated the temperature of maximum density (TMD) and the locus of the maximum of response functions close to the critical point at the fluid phase (the isothermal compressibility κ_T, the isobaric expansion coefficient α_P and the specific heat at constant pressure C_P):

$$\kappa_T = \frac{1}{\rho}\left(\frac{\partial \rho}{\partial P}\right)_T \; , \quad \alpha_P = -\frac{1}{\rho}\left(\frac{\partial \rho}{\partial T}\right)_P \; , \quad C_P = \frac{1}{N_{tot}}\left(\frac{\partial H}{\partial T}\right)_P \; , \tag{4.3}$$

where $H = U + PV$ is the system enthalpy, with V the mean volume obtained from the NPT simulations. The quantities shown in the Supplementary Material A were obtained by numerical differentiation. As consistency check, we have obtained the same maxima locations when using statistical fluctuations: the compressibility is a measure of volume fluctuations, the isobaric heat capacity is proportional to the entropy fluctuations experienced by N molecules at fixed pressure, and the thermal expansion coefficient reflects the correlations between entropy and volume fluctuations [12, 376].

Aiming to analyze the structure of the system, we have evaluated the radial distribution function (RDF) $g(r^*)$, which was subsequently used to compute the excess entropy(s_{ex}) and the translational order parameter τ, defined as [377]

$$\tau \equiv \int_0^{\xi_c} \mid g(\xi) - 1 \mid d\xi, \tag{4.4}$$

where $\xi = r\rho^{1/3}$ is the interparticle distance r scaled with the average separation between pairs of particles $\rho^{1/3}$. ξ_c is a cutoff distance, defined as $\xi_c = L\rho^{1/3}/2$, where L is the simulation box size. For an ideal gas (completely uncorrelated fluid), $g(\xi) = 1$ and τ vanishes. For crystal or fluids with long range correlations $g(\xi) \neq 1$ over long distances, which leads to $\tau > 0$.

s_{ex} can be obtained by counting all accessible configurations for a real fluid and comparing with the ideal gas entropy [378]. Consequently, the excess entropy is a negative quantity since the liquid is more ordered than the ideal gas. Note that s_{ex} increases with temperature just like the full entropy S does; in fact $s_{ex} \rightarrow 0$ as temperature goes to infinity at fixed density because the system approaches to an ideal gas [379, 380]. Analytically, the excess entropy may be computed if the equation of state is known [381]. A systematic expansion of s_{ex} exists in terms of two-particle, three-particle contributions, etc.,

$$s_{ex} = s_2 + s_3 + s_4 + ... \tag{4.5}$$

The two-particle contribution is calculated from the radial distribution function $g(r)$ as follows:

$$s_2 = -2\pi\rho \int_0^{\infty} \left[g(r)lng(r) - g(r) + 1)\right] r^2 dr, \tag{4.6}$$

since s_2 is the dominant contribution to excess entropy [382, 383] and it is proved to be between 85% and 95% of the total excess entropy in Lennard-Jones systems [384].The excess entropy and the translational order parameter τ are linked once both are dependent on the deviation of $g(r)$ from unity.

Another structural quantity evaluated was the orientational order parameter (OOP), that gives insight on the local order [377, 385–387]. The OOP for a specific particle

i with N_b neighbors, is given by

$$q_l(i) = \sqrt{\frac{4\pi}{2l+1}\sum_{m=-l}^{l}|q_{lm}|^2}, \tag{4.7}$$

with

$$q_{lm}(i) = \sqrt{\frac{1}{N_b}\sum_{j=1}^{N_b} Y_{lm}(\theta(\vec{r}_{ij}), \phi(\vec{r}_{ij}))}. \tag{4.8}$$

where Y_{lm} are the spherical harmonics of order l and $\vec{r}_{ij}$ is the vector from particle i to its neighbour j. The OOP for a whole system is obtained taking the average over the parameter value for each particle i, $q_l = \langle q_l(i)\rangle_i$. In this work we evaluated the OOP for $l = 6$, using the freud python library [388], and the number of neighbors for each particle was found computing Voronoi diagrams using voro++ [389].

The system dynamics was analyzed by the mean square displacement (MSD), given by

$$\langle[\vec{r}(t) - \vec{r}(t_0)]^2\rangle = \langle\Delta\vec{r}(t)^2\rangle \ , \tag{4.9}$$

where $\vec{r}(t_0) =$ and $\vec{r}(t)$ denote the particle position at a time t_0 and at a later time t, respectively. The MSD is then related to the diffusion coefficient D by the Einstein relation,

$$D = \lim_{t\to\infty}\frac{\langle\Delta\vec{r}(t)^2\rangle}{6t} \ . \tag{4.10}$$

For alcohol molecules we have considered the center of mass displacement. The onset of crystallization was monitored analyzing the local structural environment of particles by means of the Polyhedral Template Matching (PTM) method implemented in the Ovito software [390, 391]. Ovito was also employed to visualize the phases and take the system snapshots.

4.3 Results and discussion

In this part of the thesis, we aim to answer two questions. The first one is how the CS methanol will affect the TMD and the liquid-liquid phase transition. Next, we address to the anystropic effect: how the alcohol chain length change de polymorphism observed not only in the fluid phase, but in the solid phase as well, and how it relates to the competition and anomalies. In this way, first we will show our results for water-methanol mixtures near the TMD and LLCP region. Next, we expand this analysis, identifying the solid polymorphism at lower temperatures in pure CS water and how the presence of methanol, ethanol and 1-propanol affects the phase diagram.

Water-methanol mixtures

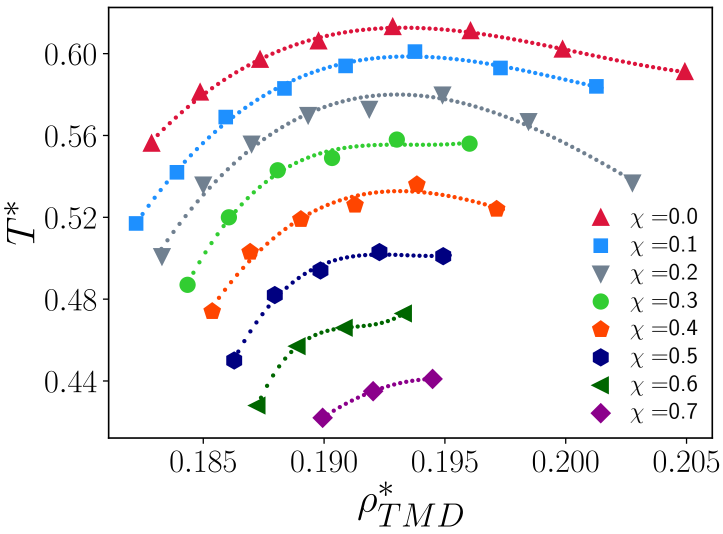

Figure 4-2: ρT diagram indicating the TMD behaviour for all molar fractions until $\chi = 0.7$. The errors bars are smaller than the data points.

We start the discussion showing the behavior of the temperature of maximum density (TMD) for distinct methanol fractions [276]. Previous studies using a different core-softened model [277] lead to TMDs appearing at too low temperatures and densities. For the methanol geometry, in Ref. [277] it was found that the presence of small amounts of methanol always lowers the TMD. The model constructed in that work acts as a 'structure-breaker', by disfavoring the build up of open structures (second scale), which is equivalent to a weakening of the hydrogen bond network. As a consequence, the system becomes less anomalous and the TMD decreases. In our case, as can be appreciated in figure 4-2, the density anomalies were observed up to high methanol fractions, $x_{MeOH} = 0.7$ - the complete isobars with the maxima are shown in the Supplementary Material. The existence of the density anomaly for such high methanol fraction is a consequence of the core-softened model employed. Once the water-water, water-hydroxyl and hydroxyl-hydroxyl interactions have the same intensity there is no difference for a water molecule to create a HB with another water molecule or with the hydroxyl site from the alcohol molecule. In fact, in this model, the interaction at the second scale – HB formed – is so strong that the effect of the first scale of the alkyl group are suppressed.

The LLCP was roughly estimated using the isothermal density derivatives of the pressure

$$\left(\frac{\partial P}{\partial \rho}\right)_T = \left(\frac{\partial^2 P}{\partial \rho^2}\right)_T = 0 \; . \tag{4.11}$$

For the case of pure core-softened water molecules – $\chi = 0.0$ – our simulations indicate a LLCP located near $P_c^* \approx 0.12$, $T_c^* \approx 0.58$ and $\rho_c^* \approx 0.23$. This result is close to the one obtained by Hus and Urbic [367], $P_c^* = 0.106$, $T_c^* = 0.58$ and $\rho_c^* = 0.246$, but distinct from the original results from Franzese [371], $P_c^* = 0.286$, $T_c^* = 0.49$ and $\rho_c^* = 0.248$. In the pure methanol limit, $\chi = 1.0$, we estimate a critical point near $P_c^* \approx 0.24$, $T_c^* \approx 0.54$ and $\rho_c^* \approx 0.29$. The critical point is slightly above the one predicted by Urbic [367], $\rho_c^* = 0.27$, $P_c^* = 0.1539$, $T_c^* = 0.503$, which is obviously a finite size effect. Additionally, unlike Hus and Urbic [367], we do not use the Umbrella Sampling technique to avoid the spontaneous crystallization – more recently, Desgranes and Delhommelle [368] have effectively employed a non-equilibrium technique to prevent the spontaneous crystallization. Our goal here is not prevent it, but analyze how it is related to the liquid-liquid phase transition and the existence of a density anomaly.

In the Supplementary Material we provide the isobars in the $T \times \rho$ phase diagram, the $P \times T$ phase diagram with the phases and maxima in the response functions as the κ_T, C_P and α_P curves for all temperatures, pressures and densities, as well tables with all critical temperatures T_c^*, pressures P_c^* and densities ρ_c^* and the higher temperature where the solid phase was observed, T_{HCP}. Here, for simplicity, we show the phase diagram of four concentrations: pure core-softened water ($x_{MeOH} = 0.0$),

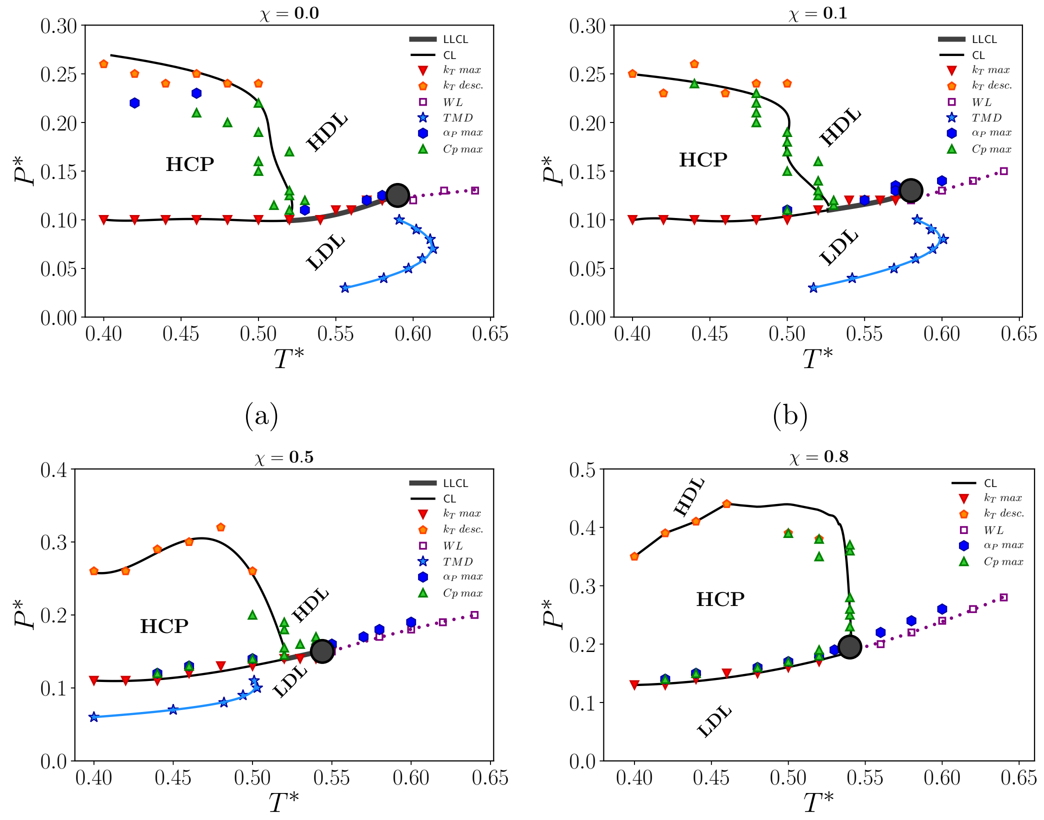

(a) (b)

(c) (d)

Figure 4-3: Phase diagrams for (a) pure water and mixtures with methanol concentration (b) $x = 0.1$ (dilute regime), (c) $x = 0.5$(balanced regime), and (d) $x = 0.8$. The black solid lines are the LDL-HDL, LDL-HCP and HCP-LDL coexistence lines. Maxima in the response functions are: red triangles are maxima in κ_T below the critical point, purple squares maxima in κ_T above the critical point indicating the Widom Line (WL), orange triangles represent discontinuity in κ_T for larger pressures, green triangles are maxima in C_P and blue hexagons maxima in α_P. Blue stars are the TMD line. The gray large dot is the critical point. The errors bars are smaller than the data points.

dilute regime ($\chi = 0.1$), balanced regime ($x_{MeOH} = 0.5$) and methanol rich regime ($x_{MeOH} = 0.8$). The latter composition corresponds to the lowest concentration of methanol without density anomaly.

The isothermal compressibility, κ_T, is an indication of the vicinity of the critical behavior and its line of maxima in the P-T diagram defines the Widom line. In figure 4-3, we can see that this response function has maxima in the Widom line and in the LDL-HDL coexistence line. However, below T_{HCP} it has a maximum at low pressures and a discontinuity at higher pressures. The maxima at low pressures are the continuation of the Widom/LDL-HDL coexistence line that turns into a coexistence between the LDL phase and the solid hexagonal closed packed (HCP) phase. For mixtures we can clearly identify the solid phase as HCP if we consider only the hydroxyl group when using the PTM method. At higher pressures, the discontinuity coincides with a second-order HCP-HDL melting. The C_P behavior indicates the higher melting temperature T_{HCP} in the HCP-HDL phase transition, as we can see in the figure 4-3. For isotherms above the critical point it is possible to observe the Widom line - here we characterize it using the maxima in κ_T in supercritical isotherms and the also using the points where the water-water or OH-OH radial distribution function have the same occupancy [392]. As well, the maxima in isobaric thermal expansion coefficient,α_P, are observed at this line. As the phase diagrams in the figure 4-3 shows, the TMD is observed up to the limit where $T_{HCP} < T_C$. To understand the mixture behavior we will analyze in more detail the dilute and concentrated regimes.

The liquid polymorphism can also be observed analyzing the structure and the dynamics of the water-methanol dilute mixtures. In the figure 4-4 we show the dynamical and structural behavior along three isotherms for the case $\chi = 0.1$: $T^* = 0.52$, smaller than T^*_{HCP}, $T^* = 0.56 > T^*_{HCP}$, subcritical isotherm that crosses the LDL-HDL coexistence line, and the supercritical $T^* = 0.62 > T^*_C$, that crosses the Widom line. Along the subcritical isotherm $T^* = 0.52$ three distinct behaviors can be observed. At lower pressures it corresponds to the LDL phase. Then, the diffusion constant D – figure 4-4(a) – decreases while the translational order parameter τ – figure 4-4(b) – increases. This lower diffusion and higher structure corresponds to the spontaneous crystallization in the HCP phase. Also, the maxima in the κ_T and the discontinuity in D and τ indicate a first order phase transition. Increasing the pressure it transforms into the HDL phase - here, the discontinuity in κ_T and the smooth curve for D and τ indicates that this is a second order phase transition. The radial distribution function, figure 4-4(c), also shows clearly three distinct structures along this isotherm. At lower pressures the LDL structure is dominated by the second length scale in the

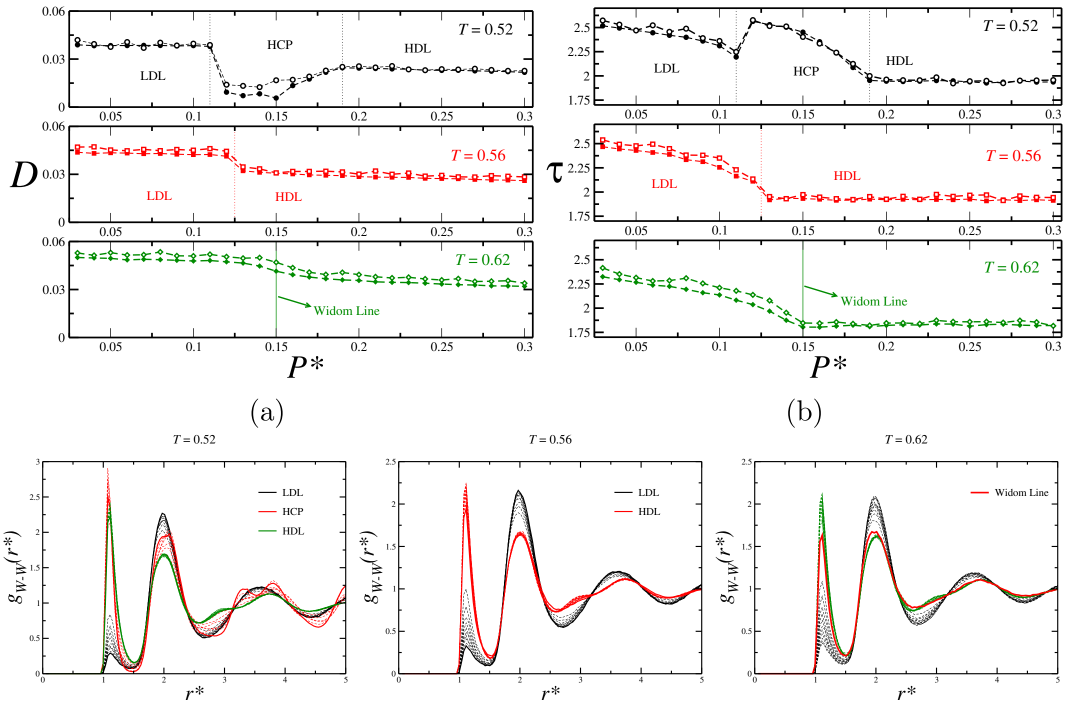

(a) (b)

(c) (d) (e)

Figure 4-4: Dynamical and structural analysis of the mixture with $\chi = 0.1$ (a) Diffusion coefficient for water (filled symbols) and methanol center of mass (open symbols). (b) Translational order parameter τ for water (filled symbols) and OH monomers (open symbols). The errors bars are smaller than the data points. Water-water radial distribution function $g_{W-W}(r^*)$ for three isotherms: (c) $T^* = 0.52$ that crosses the HCP region, (d) $T^* = 0.56$ that crosses the LDL-HDL coexistence line and (e) $T^* = 0.62$ that crosses the Widom line.

CSW potential, as the black curves in figure 4-4(c) indicate. Compression forces the most molecules in the system to vacate second length scale, approach each other and occupy positions at separations close to the first potential scale. As a consequence, at high pressures we observe the HDL structure - green curves in figure 4-4(c). Between the LDL and the HDL phases, the system freezes in a solid HCP phase, whose region is indicated by the red curves in figure 4-4(c). The system structure is controlled by the core-softened interactions – Eq. 4.1– among water-water, water-OH and OH-OH sites. The CSW monomers change from one structure to another, while the LJ24-6 monomers behave as if they were in a gas-like phase, in agreement to what has been found in previous works for core-softened/LJ dumbbells [365, 367].

A different behavior has been observed along the subcritical isotherm, $T^* = 0.56$.

At this temperature no HCP structure was found. As a consequence, only one phase transition takes place – D and τ have a discontinuity at the transition, as the shown in the Figures 4-4(a) and (b). At this point the system changes from LDL to HDL structure as illustrated in the figure 4-4(d). Also, the RDFs display a sudden change with the characteristics of one length scale to those of the other at the coexistence pressure. This is in contrast with our observations for the supercritical isotherm, $T^* = 0.56$, that crosses the Widom line. Here is also possible to see a change in the behavior of D and τ as we cross the WL – see the Figs. 4-4(a) and (b)–. However, the RDF in figure 4-4(e) shows that there is a pressure where the occupancy of the first and second length scales are the same. As Salcedo and co-authors have shown [392] this can be interpreted as an indication that the Widom line has been reached.

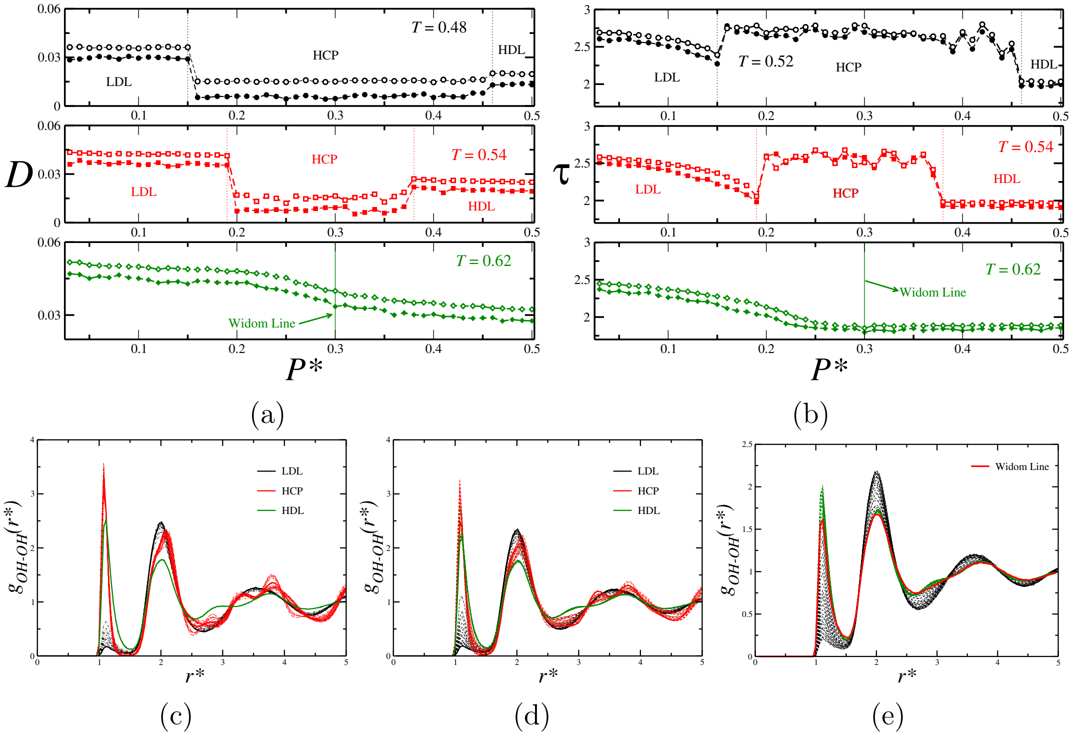

(a) (b)

(c) (d) (e)

Figure 4-5: Dynamical and structural analysis of the mixture with $\chi = 0.8$ (a) Diffusion coefficient for water (filled symbols) and methanol center of mass (open symbols). (b) Translational order parameter τ for water (filled symbols) and OH monomers (open symbols). The errors bars are smaller than the data points. OH-OHr radial distribution function $g_{OH-OH}(r^*)$ for the subcritical isotherm (c) $T^* = 0.48$, the critical (d) $T^* = 0.54$ and the supercritical (e) $T^* = 0.62$.

Nonetheless, if the mixture lacks density anomaly we do not observe the LDL-HDL coexistence. As we show in figure 4-5, along the subcritical and critical isotherms ($T^* = 0.48$ and $T_C^* = 0.54$ respectively) the two liquid phases are separated by the HCP region. However, we can see signatures of liquid-liquid critical point in the maxima of the response functions [277] and the equality of occupation numbers corresponding to both scale lengths, as shown in figure 4-5(e).

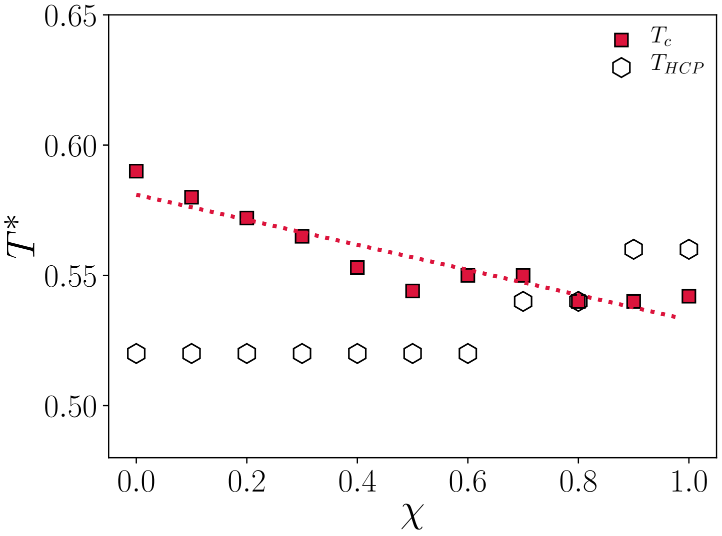

Figure 4-6: Liquid-Liquid critical temperature T_C^* and higher temperature of spontaneous crystallization T_{HCP}^* for distinct concentrations of methanol in the mixture. The errors bars are smaller than the data points.

Adding methanol to the water changes the competition scenario. The W_{CS} particles - the water and the hydroxyl groups - lead to a competition between the two length scales that mimic full hydrogen bonding (open structure at the second length scale) or broken hydrogen bonds (dense structure dominated by separations at the first length scale) [393]. As mention, this is the source of the well known water-like anomalies and of the existence of the LLCP in these CS fluids [372]. Our results have shown a discontinuous change in the occupancy from the second to the first length scale along the liquid-liquid coexistence - there is no pressure value where the occupancy in both scales are equal (no Widom line). On the other hand, the change in the occupancy is continuous along a supercritical isotherm, with an equal occupancy in the Widom line. On the other hand, the presence of our model methanol particles changes the scenario. The hydroxyl behaves as water, but the methyl groups acts as hydrogen bond breakers, which favors structures where particles accommodate in the first length scale. This unbalanced competition kills the density anomaly. At the same time, the energy necessary to for particles to leave the second scale and occupy the first one is small. Consequently, the critical temperature T_C of the LLPT lowers with x_{MeOH}. Also, higher energy is required to leave the first scale, and this is necessary to melt the HCP crystal into the HDL phase. As a consequence, T_{HCP} increases with x_{MeOH}. The methanol concentration where these two temperatures are equal is the same as the one where water-like anomalies vanish, as illustrated in Figure 4-6. Summarizing, large amounts of methanol in water kill the density anomaly and suppress the LLPT by favoring spontaneous crystallization.

Solute-size effects

Pure CS Water phase diagram

Once the solid polymorphis of the CS mode was not explored in the literature, we expand the previous water phase diagram and, before discussus the mixture with bigger alcohol, we will discuss in more details the water phase diagram. The LLCP location was estimated using the isothermal density derivatives of the pressure (eq. 4.11). Coming from the supercritical region, the LLCP lays at the end of the Widom Line (WL) - a line in the $P \times T$ phase diagram that can be obtained by the maxima in the response function κ_T and corresponds to the separation between LDL-like and HDL-like behavior in the supercritical regime. In the figure 4-7 (a) we show the CS water phase diagram obtained from our simulations. The WL, indicated by the dotted purple line and the purple squares, ends at the LLCP. Below the LLCP we have the transition between the liquid phases, indicated by the discontinuity in the thermodynamic property κ_T – shown in the Supplementary Material (SI) A for all isotherms – and in the structural and dynamic properties. For instance, the upper panel in the figure 4-7(b) shows the structure factor τ for the subcritical pressure $P^* = 0.13$ and for the supercritical pressure $P^* = 0.15$ as function of the inverse of temperature. As T decreases we can see a discontinuity in the subcritical isobar, in-

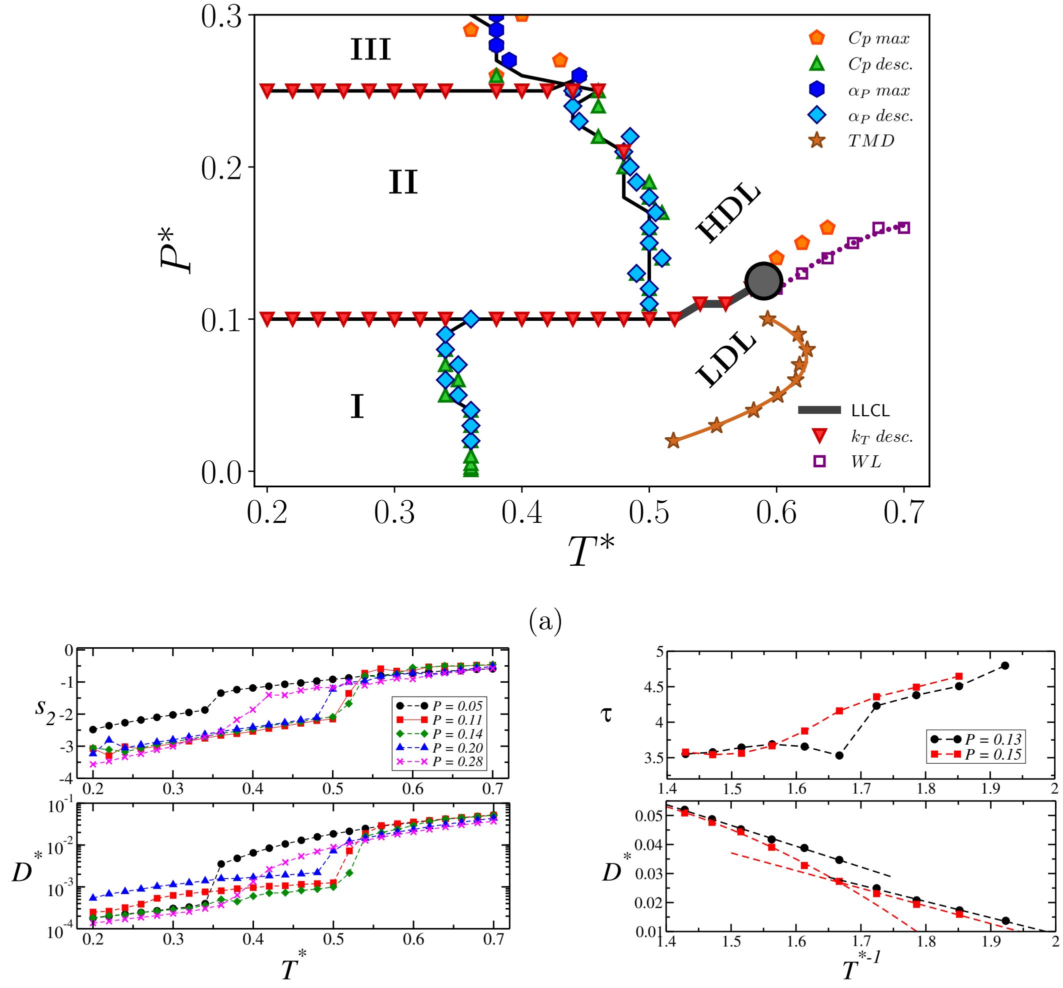

(a)

(b)

(c)

Figure 4-7: (a) PT phase diagrams for pure CS water showing the solid phases I (BCC solid), II (HCP solid) and III (amorphous solid) and the low and high density liquid phases. The points in the phase separations indicate distinct discontinuities or maxima in the evaluated response functions. The Widom Line corresponds to maxima in κ_p. The solid-liquid coexistence lines were draw based in the discontinuities in the pair excess entropy, the structure factor (not shown here for simplicity) and in the diffusion constant, as indicated in the figure (b). Also, the pair excess entropy (not shown here for simplicity), the structure factor and D^* have discontinuities in the LDL-HDL transition, as we show in the figure (c) for the subcritical isobar $P^* = 0.13$, and a fragile to strong transition for the supercritical isobar $P^=0.15$ as it crosses the Widom Line.

dicating an abrupt change in the fluid structure. On the other hand, the supercritical isobar has a monotonic increase in τ as T decreases, indicating an increase in the particles order. Similarly, the dependence of the diffusion coefficient D with T^{*-1} is discontinuous in the supercritical isobar. For the supercritical pressure $P^* = 0.15$ we see a change in the diffusion inclination with temperature when it crosses the Widom Line, indicating the HDL-dominated to LDL-dominated regime. These results are in agreement with our recent work obtained by the heating of the system [369] and previous works employing this potential [371, 372, 394, 395].

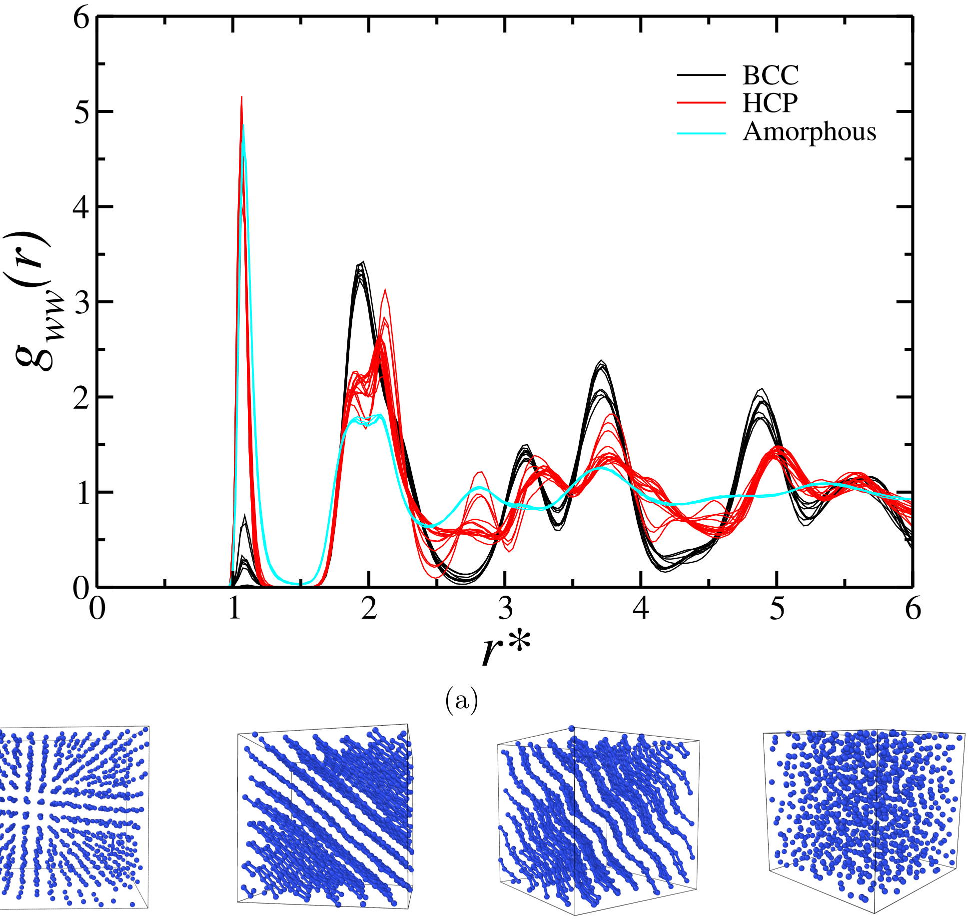

(a)

(b) (c) (d) (e)

Figure 4-8: (a) CS water-water radial distribution function (RDF) along the isotherm $T^* = 0.26$. Black lines are the pressures in the BCC phase, red lines in the HCP phase and cyan in the amorphous phase. System snapshots in the (b) BCC phase, HCP phase with (c)straight or (d) rippled planes and in (e) the amorphous solid phase.

However, the solid phases weren't explored for this system. In fact, the HCP phase was observed in our work [369] and in the study by Hus and Urbic using the methanol model [367, 396]. Here, exploring a larger region in the phase diagram, we characterized three distinct solid phases. The solid phase I corresponds to a body-centered cubic (BCC) crystal at lower pressures. Increasing P it changes to the solid phase II, with a hexagonal closed packed (HCP) structure, and at even higher compression we observe the amorphous solid, named phase III. The transition between the solid phases, and from LDL to HCP, are well defined by the discontinuous behavior in κ_T, shown in the SI. The transition from solid phase I to LDL and from solid phase II to HDL have discontinuities in the response functions α_p and C_p, shown in the SI. Also, the structure (here characterized by the pair excess entropy) and the dynamic behavior (given by the diffusion coefficient) are discontinuous for these solid-fluid transition. This can be observed in the figure 4-7(c). Here, the pressure $P^* = 0.05$ is a isobar that cross the BCC-LDL transition, $P^* = 0.11$, 0.14 and 0.20 the HCP-HDL transition and $P^* = 0.28$ the amorphous-HDL transition. As we can see, the structure and dynamics change smoothly for this last transition, as the magenta line for $P^* = 0.28$ indicates in the figure 4-7 (c). Also, the response functions C_p and α_p are not discontinuous in this transition, but have a maximum – indicating that this is a second order, smooth transition. The distinct phases can also be observed when we analyze the water-water radial distribution function (RDF) $g_{ww}(r)$ along one isotherm. For instance, we show in the figure 4-8(a) the $g_{ww}(r)$ for pressures ranging from $P^* = 0.01$ to $P^* = 0.30$ along the isotherm $T^* = 0.26$. We can see clear changes in the structure as P varies. At lower pressures the particles are separated mainly at the second length scale, characterizing the BCC phase – a snapshot at $P^* = 0.01$ and $T = 0.26$ is shown in the figure 4-8(b). Increasing the pressure the system changes for the HCP phase, where the occupation in the first length scale dominates the structure. In fact, the HCP planes are separated by a distance equal to the second length scale, while the distance between particles in the same plane is the first length scale. It becomes clear when we use the Ovito [391] feature "create bonds" if the distance is equal to the first scale. While for the BCC snapshot we did not see any bond, for the HCP snapshot at $P^* = 0.14$ in the figure 4-8(c) we can see the bonds between particles in the same plane. As P grows, the HCP planes get rippled, as we can see in figure 4-8(d) for $P^* = 0.24$ and in the behavior of the RDF red lines. Finally, it changes to an amorphous structure at high pressure, as we show for $P^* = 0.30$ in figure 4-8(e).

Now, with the phase behavior of the CS water model depicted, we can see how the presence of short alcohol affects the observed phases and the density anomaly.

Water-short alcohol mixtures

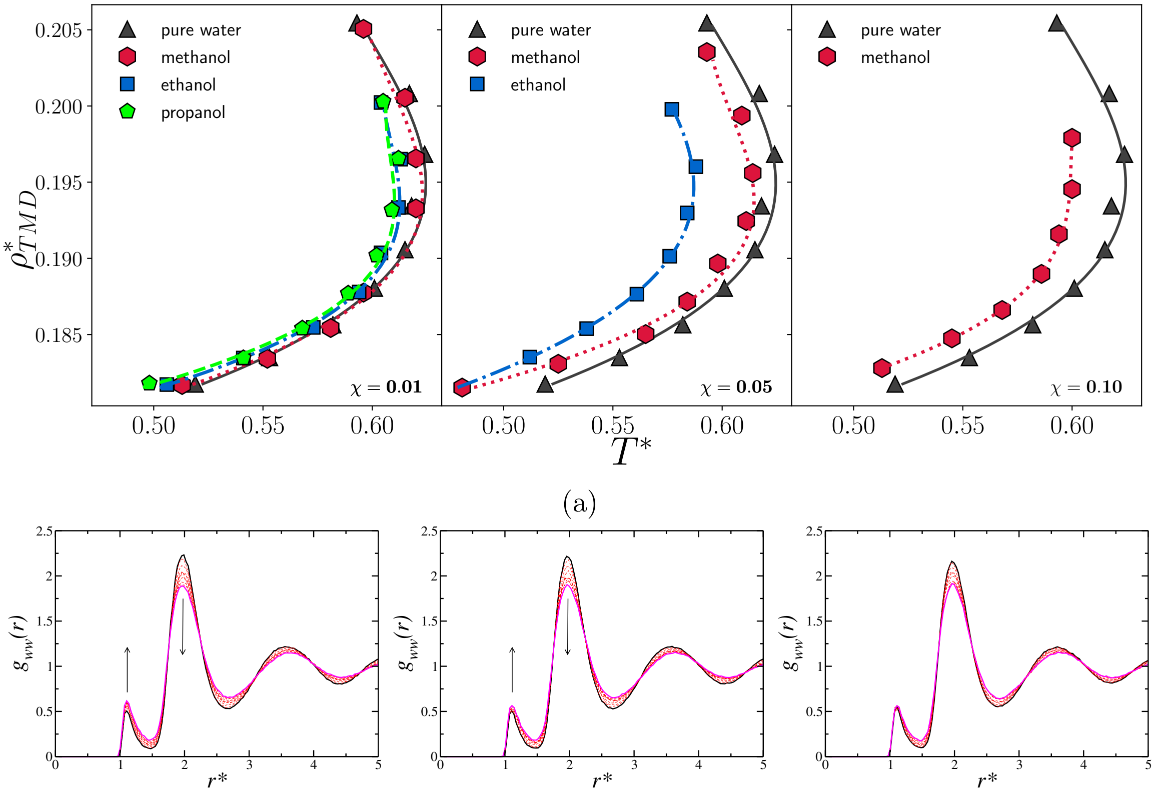

(a)

(b) (c) (d)

Figure 4-9: (a) TMD behaviour of all CS alcohols used in this work: for $\chi_{alc} = 0.05$, 1-propanol didn't show TMD and for $\chi_{alc} = 0.10$, only methanol shows TMD. (b) CSW-CSW radial distribution function $g_{ww}(r)$ along the isobar $P^* = 0.08$ for water-ethanol at $\chi_{alc} = 0.10$ case with temperatures ranging from $T = 0.50$ (black solid line) to $T = 0.68$ (magenta solid line). The intermediate temperatures are shown with red dashed lines. The arrows indicate the competition between the scales as T increases. (c) is for the case with ethanol concentration at $\chi_{alc} = 0.05$, were the competition between the scales and the TMD are still observable, while for (d) $\chi_{alc} = 0.10$ both competition and TMD vanish.

Small concentrations of short chain alcohols such as methanol, ethanol and 1-propanol create a very interesting effect in the TMD line [265, 353]. They act as "structure maker", promoting the low density ice-like water structure and increasing the TMD. This is usually observed for alcohol concentrations χ_{alc} smaller than 0.01 - and is not our goal here. We want to analyze the TMD vanishing and what happens in the phase diagram as it vanishes. This can be observed as x increases and methanol acts as "structure breaker". Using the CS model for water-methanol mixtures [369] we found that the TMD persists up to high methanol concentrations, as $\chi < 70\%$ – much higher than in experiments. This is a consequence of the model: the same potential is employed for water-water, water-OH and OH-OH. On the other hand, the energy for the water-water h-bonds is equal to the water-OH h-bonds. Nevertheless, we can increase the structure breaker effect by increasing the solute size. In fact, for ethanol the TMD line vanishes at $\chi_{alc} = 0.10$, while for 1-propanol the TMD is only observed at $\chi_{alc} = 0.01$ - the TMD lines are shown in the figure 4-9(a).

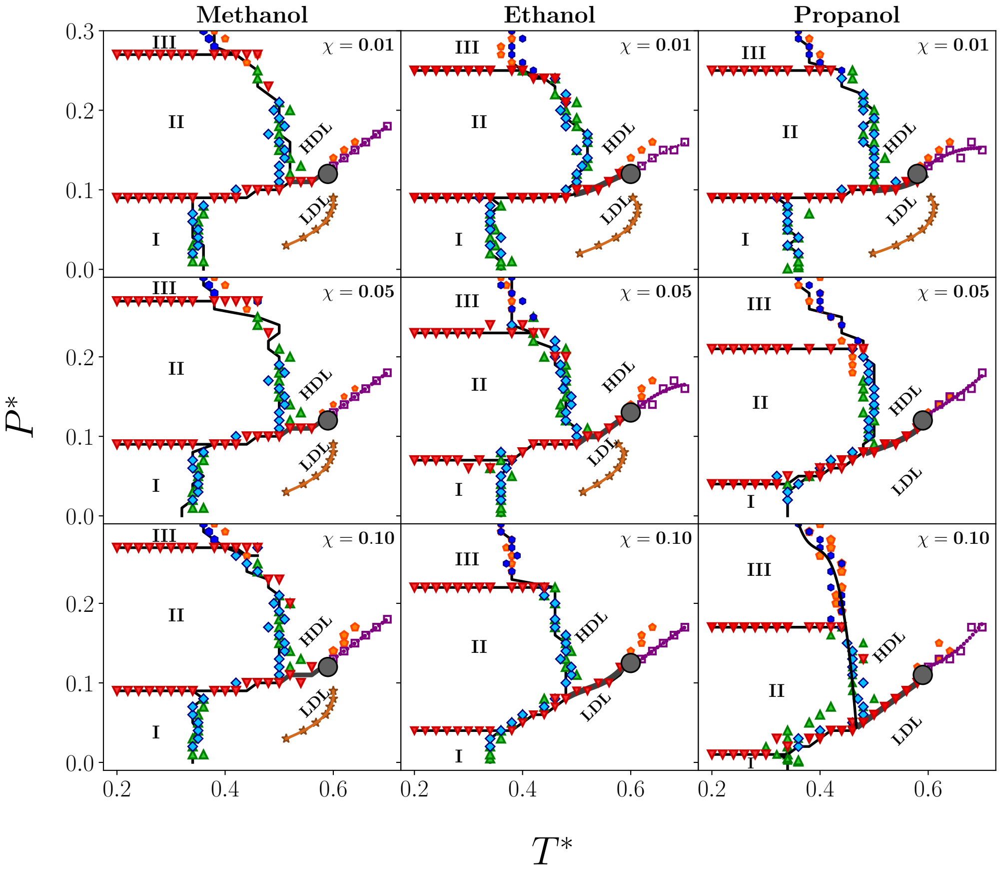

Figure 4-10: PT phase diagrams for aqueous solutions of (a) methanol, (b) ethanol and (c) propanol for all concentrations analyzed in this work.

The water anomalous behavior is related to the competition between two liquids that coexist [237, 392, 397]. This competition can be observed using the $g_{ww}(r)$. Here we show the RDFs the isobar $P^* = 0.080$ between the temperatures $T^* = 0.50$ and $T^* = 0.68$ for a fraction of ethanol of $\chi_{alc} = 0.01$ in the figure 4-9(b), for $\chi_{alc} = 0.05$ in the figure 4-9(c) and for $\chi_{alc} = 0.10$ in figure 4-9(d). As we can see, for the fractions $\chi_{alc} = 0.01$ and $\chi_{alc} = 0.05$ we observe the competition between the scales: the water particles migrates from the second length scale to the first length scale as T increases, as indicated by the arrows. On the other hand, for $\chi_{alc} = 0.10$ there is practically no increase in the occupation of the first length scale as the occupation in the second length scale decreases. Once there is no competition, we do not observe the density anomaly. This indicates that adding higher concentration of alcohol changes the competition between the scales in the CSW water model and that the CS alcohol chain length also affects the competition - in our previous work for methanol, we only observe this at $\chi_{alc} = 0.70$ [369].

Curiously, even without the density anomaly, all the water-alcohol mixtures have liquid-liquid phase transition. In the figure 4-10 we show the PT phase diagrams for all the fractions and types of alcohols. After the liquid-liquid critical point, The Widom Line (WL) separates water with more HDL-like local structures at high temperatures from water with more LDL-like local structures at low temperatures [398]. Looking at the diffusion coefficient D^* isotherms we can see the distinct transitions. At lower temperatures, as $T^* = 0.34$ it melts from the solid phase to the HDL phase at high pressures, as we show in the figure 4-11. Increasing T^*, we can see the system going from the LDL phase (with $D^* > 0$) to the HCP phase, with diffusion near zero, to the HDL phase, were D^* increases again. In the isotherms that cross the LDL-HDL transition we can see the discontinuity in the curve, indicating the phase transition. Above the LLCP we can see a change in the $D^* \times P^*$ curve behavior as it crosses the WL.

The same discontinuity can be observed in the structural behavior. Besides τ and s_2, we also evaluated the q_6 to analyze the structure. For simplicity, we show here only the case of pure water and water-ethanol mixtures. Along the isotherm $T^* = 0.46$,

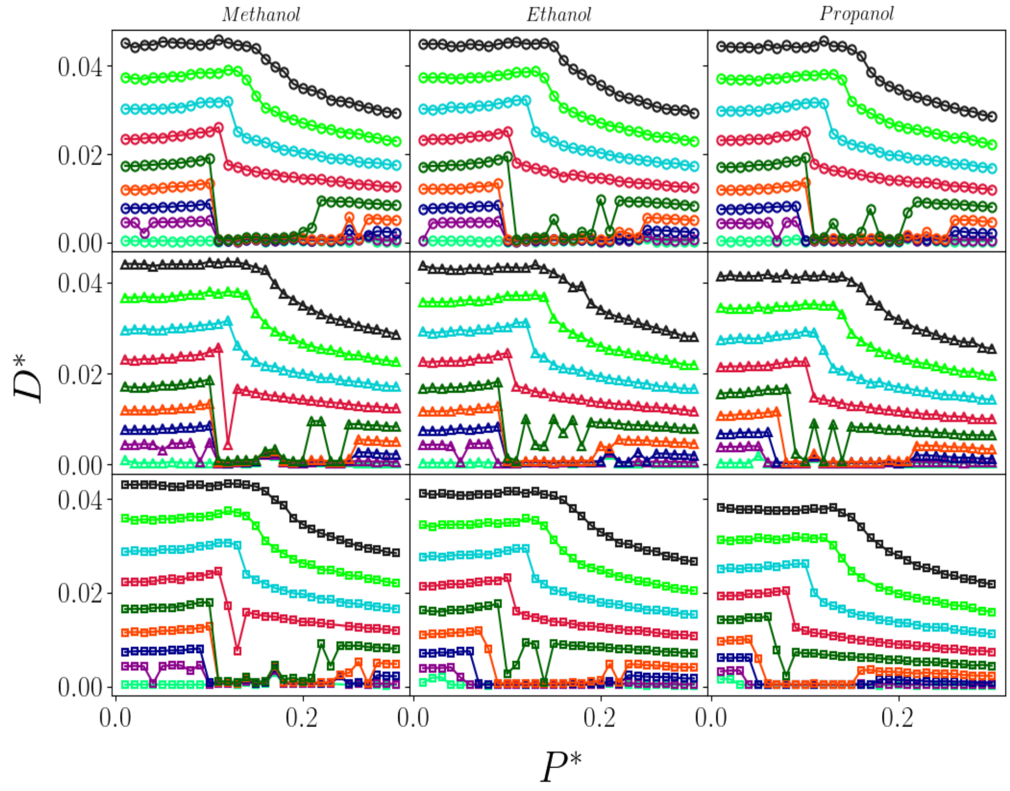

Figure 4-11: Diffusion coefficient versus pressure for all solutions analyzed in this work. From bottom to top in each diagram, we have the isotherms $T^* = 0.34, 0.38, 0.42, ...0.66$. Each row represents a concentration of solute: $x_{alc} = 0.01, 0.05\ and\ 0.1$

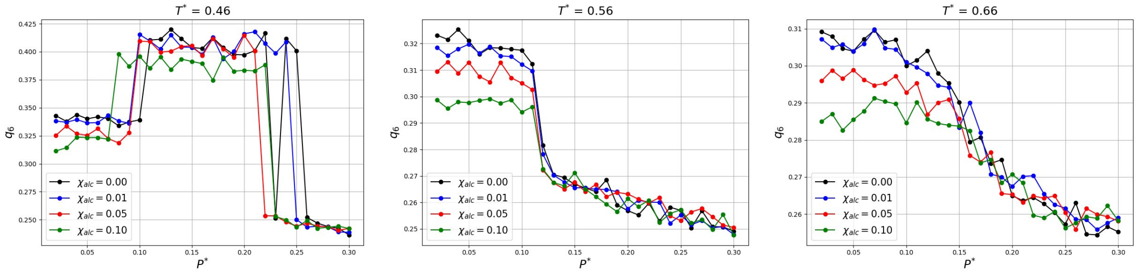

(a) (b) (c)

Figure 4-12: Local bond orientation order parameter q_6 as function of pressure for the isotherms (a) $T^* = 0.46$, (b) $T^* = 0.56$ and (c) $T^* = 0.66$.

that crosses the phases LDL, HCP and HDL, we can see in the figure 4-12(a) clearly the discontinuities correspondents to this transitions for all fractions of ethanol. Also, it is noticeable how the ethanol is structure breaker: the value of q_6 in the LDL and

HCP phases are smaller as χ_{alc} increases. Along the isotherm $T^* = 0.56$, shown in the figure 4-12(b), we can see the same structure breaker effect in the LDL regime, and a discontinuous transition to the HDL phase. In contrast, above the LLCP there is no discontinuity. The isotherm $T^* = 0.66$, shown in the figure 4-12(c), have a smooth decay in q_6 as it crosses the WL and goes from LDL-like to HDL-like. This is interesting, once it indicates that a system can have a LLCP without have density anomaly.

As in the pure CSW water case, three solid phases were observed. However, an interesting finding is how the carbon chain length affects the solid phases. It is clear that longer apolar chains affects the extension of the region occupied by each solid phase: the BCC crystal (region I) loses space, moving to lowers pressures. Likewise, the HCP crystal (region II) moves to lower pressures as the alcohol chain increase. However, the area occupied in the PT phase diagram remains - it just shifts to lower pressures as the size and fraction of alcohol increases. For this two solid phases, the temperature range in the PT phase diagram seems to be independent of the fraction χ_{alc}. On the other hand, the amorphous solid phase (region III) is favored as the it expands its extension to lower pressures and higher temperatures as the apolar chain grows. To understand why the HCP phase remains occupying a large area in the phase diagram while the BCC area shrinks we show in the figure 4-13 the $g_{ww}(r)$ for the three alcohols with fraction $\chi_{alc} = 0.10$ along the isotherm $T^* = 0.26$ from $P^* = 0.01$ to $P^* = 0.30$. Comparing the three cases with the pure CSW case, figure 4-8(a), is clear that increasing the size of the apolar tail in the alcohol favor the occupation in the second length scale. While for methanol and ethanol we see a low occupation in the first length scale at the lower pressures, for propanol this occupancy is high even for $P^* = 0.01$. This is consequence of a alcohol bubble formation: for the CS methanol, once the molecule size is comparable to the second length scale and the OH is modeled as a CSW particle, the molecules merge in the BCC structure, as we show in the figure 4-13(d). However, the longer alcohols create bubbles, as we can see in figure 4-13(e) and (f) for ethanol and propanol, respectively. It alters the water structure near the bubbles, favoring the first length scale. It reflects in the local

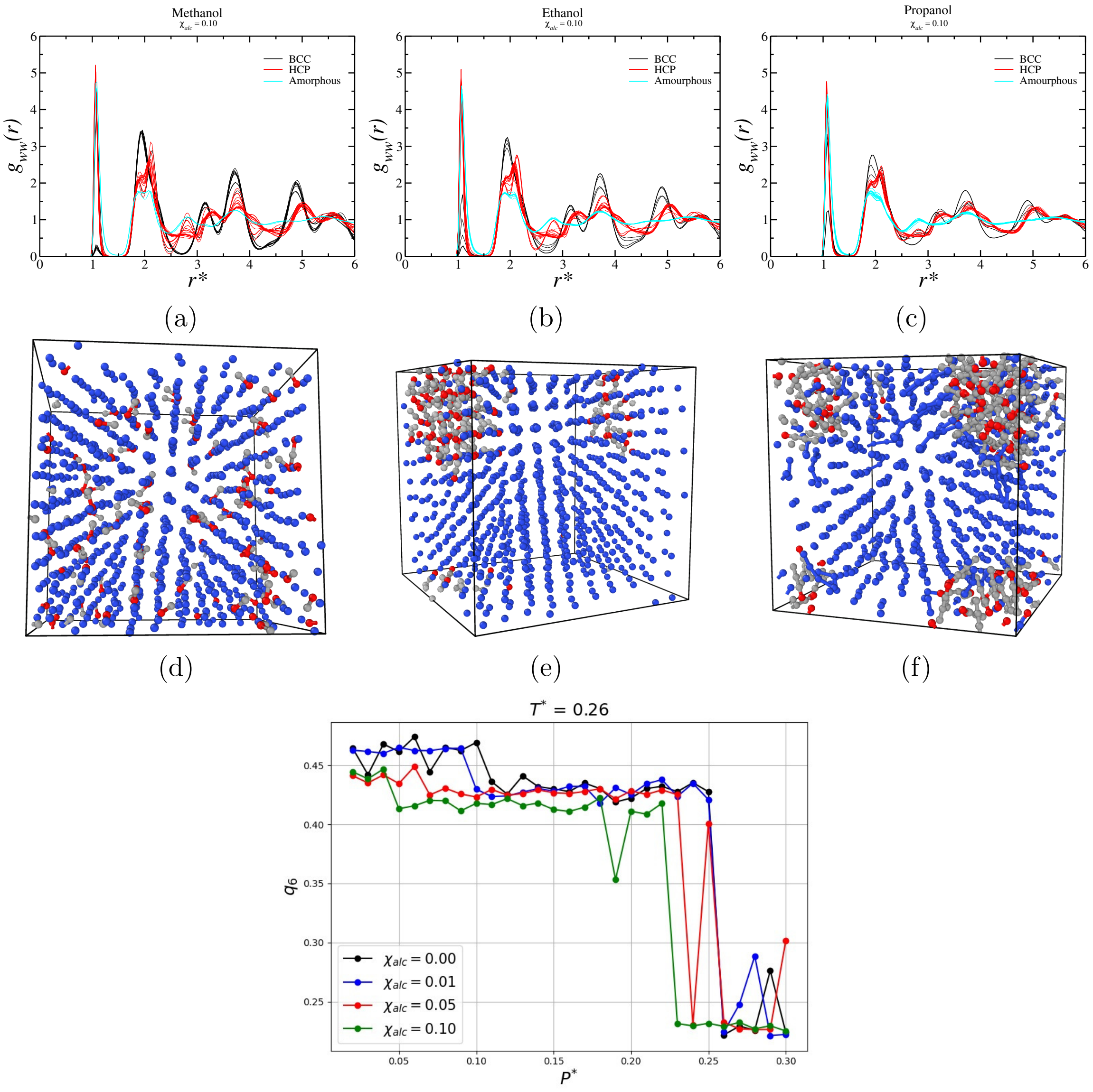

(a) (b) (c)

(d) (e) (f)

(g)

Figure 4-13: CSW-CSW radial distribution function $g_{ww}(r)$ along the isotherm $T^* = 0.26$ for water-alcohol mixtures with $\chi_{alc} = 0.10$ for (a) methanol, (b) ethanol and (c) propanol. Snapshots for the correspondents mixtures: $\chi_{alc} = 0.10$ of (d) methanol, (e) ethanol and (f) propanol. (g) Local bond orientation order parameter q_6 as function of pressure for the isotherm $T^* = 0.26$.

orientation. In the figure 4-13(g) we show the q_6 for this isotherm for the case of pure CS water ($\chi_{alc} = 0.00$) and the three fractions of ethanol. We can see that for both crystal phases, BCC and HCP, the local order is affected by the alcohol once that q_6 is small for higher fractions.

Chapter 5

Final Remarks and Conclusions

In this work we analyzed four systems which display water-like anomalies: a two dimensional system of polymer grafted nanoparticles using large-scale Langevin Dymanics simulations and three coarse-grained mixtures: one composed of water and TBA, a second whose composition occurs between water and methanol, and a third where we studied the effects of solute size in mixtures of water and methanol, ethanol and propanol.

In the first system described in the thesis a two dimensional system of polymer grafted nanoparticles is analyzed using large-scale Langevin Dymanics simulations. The use of effective core-softened potentials allow us to explore the complete system phase space. In this way, the PT, $T\rho$ and $P\rho$ phase diagrams for each potential were obtained The phase boundaries were defined analyzing the specific heat at constant pressure, the system mean square displacement, the radial distribution function and the discontinuities in the density-pressure phase diagram. Also, due the competition in the system we have observed the presence of water-like anomalies, such as the temperature of maximum density - in addition with a tendency of the TMD to move to lower temperatures (negative slope)- and the diffusion anomaly. Different structural morphologies were observed for each nanoparticle case. We observed that for the fixed polymer case the waterlike anomalies originate in the competition between the potential characteristic length scales, while for the free to rotate case the anomalies arises due to a smaller region of stability in the phase diagram and no competiton between the scales was observed. The main driving force for these different morphologies is the competition between strong short-range attractions of the particle cores (the enthalpic gain upon the core-core aggregation) and long-range entropic repulsions of the grafted chains. Thus, it is a system that allows us to recognize that the water-like anomalies are present in many different systems in addition to pure water and that this type of behavior is due to a meso-scale interaction and therefore can be captured by effective potentials.

In the second system analyzed in this thesis, we have devised a simple diatomic model for TBA with three-body interactions on the hydroxyl site that mimics the formation of hydrogen bonds. Cross interactions were fitted to qualitatively account for the experimental excess properties of water/TBA solutions, with water represented by Molinero and Moore's model [284]. We have seen that the model is capable of reproducing the experimental enhancement of the density anomaly of water observed for very small concentrations of alcohol. A structural analysis of the simulation results illustrates the correlation between the presence of a maximum of certain clathrate structures and the density anomaly. The fact that the maximum occurs in the bulk clathrates and not interfacial clathrates and that high density liquid-like structures also increase in a monotonic fashion with temperature seems to be at the root of the density anomaly enhancement. As found in Ref. [278], a much more sophisticated all-atom model is unable to reproduce the experimental behavior. Future work should address the inability (until now) of all-atom models to account for the concentration dependence of water anomalies. In this regard, the role of the hydrogen bond network has to be reassessed and possibly include non-additive effects such as polarization and charge transfer.

The third system described in this thesis allowed us to explore the supercooled regime of pure water, pure methanol and their mixtures using a core-softened potential models. Our aim has been to understand the relations between density anomaly, liquid-liquid phase transition and spontaneous crystallization. Essentially, by increasing the methanol concentration in the mixture we observe three effects: the density anomaly shrinks and finally vanishes, the critical temperature for the LLPT is lowered and the temperature for the spontaneous crystallization increases. These features can be understood as a direct consequence of the uneven competition of length scales induced by the presence of methyl group in the methanol molecule. This group favors the occupancy of the first length scale by water and hydroxyl sites – i.e. disrupts the hydrogen bond network. However, even for the case of pure methanol one can determine the Widom line but the critical point disappears in the solid region. As Desgranges [368] showed, shear stress can prevent this crystallization and lead to possible experimental observations of the LLCP for pure methanol. Our results shed some light on the molecular behavior of water-methanol mixtures in the supercooled regime. A natural question that arises is how larger amphiphilic molecules might change this scenario. New simulations are being performed in this direction.

Finally, in the fourth system originating from this thesis we have explored the supercooled regime of pure water and mixtures of water and short chain alcohols: methanol, ethanol and propanol using a two-length scale core-softened potential approach. Our aim has been to understand the influence of chain size on density anomaly, the liquid-liquid phase transition and on the polymorphism which are generally observed in these models. There's a pronounced influence of the apolar chain size on solid polymorphism. The BCC phase loses space in the phase diagram once longer alcohols favor the occupancy in the first length scale. Once the HCP phase has a higher occupancy in this length scale it is shifted to smaller pressures, while the amorphous solid phase grows favored by the disorder induced by alcohol. The density anomaly vanishes as the competition between the scales is suppressed in the LDL phase. However, the LDL-HDL phase transition persists for all cases. This indicates that the competition between two liquids is connected with waterlike anomalies, but the system will no necessarily have the anomalies if it has a liquid-liquid phase transition and liquid-liquid critical point. This results helps to understand the complex behavior of water and mixtures with amphiphilic solutes in the supercooled regime.

References

[1] I. Newton, *Opticks* (Smith and Walford, 1704).

[2] R. J. Boscovich, *Philosophiae naturalis theoria redacta ad unicam legem virium in natura existentium* (Officina Libraria Kaliwodiana, 1758).

[3] L. Guzzardi, "Ruggiero boscovich and "the forces existing in nature"", Science in Context **30**, 385–422 (2017).

[4] G. Belli, *Riflessioni sulle leggi dell'attrazione molecolare.* (Giornale de Fisica, 1814).

[5] G. Malescio, "Intermolecular potentials - past, present, future", Nature materials **2**, 501–3 (2003).

[6] J. C. Maxwell, "Iv. on the dynamical theory of gases", Philosophical Transactions of the Royal Society of London **157**, 49–88 (1867).

[7] J. Waals and J. Rowlinson, *J.d. van der waals: on the continuity of the gaseous and liquid states*, Studies in statistical mechanics (North-Holland, 1988).

[8] I. Kaplan, *Intermolecular interactions: physical picture, computational methods and model potentials*, Wiley Series in Theoretical Chemistry (Wiley, 2006).

[9] P. Debye, "Zur theorie der spezifischen wärmen", Annalen der Physik **344**, 789–839 (1912).

[10] F. London, "Zur theorie und systematik der molekularkrafte", Zeitschrift fur Physik **63**, 245–279 (1930).

[11] J. Israelachvili, *Intermolecular and surface forces*, Intermolecular and Surface Forces (Elsevier Science, 2015).

[12]M. P. Allen and D. J. Tildesley, *Computer simulation of liquids*, 2nd (Oxford University Press, Inc., New York, NY, USA, 2017).

[13]L. Verlet, “On the theory of classical fluids”, Il Nuovo Cimento (1955-1965) **18**, 77–101 (1960).

[14]H. D. Ursell, “The evaluation of gibbs’ phase-integral for imperfect gases”, Mathematical Proceedings of the Cambridge Philosophical Society **23**, 685–697 (1927).

[15]J. E. Mayer, “The statistical mechanics of condensing systems. i”, The Journal of Chemical Physics **5**, 67–73 (1937).

[16]C. Gray, K. Gubbins, and C. Joslin, *Theory of molecular fluids*, Vol. 2 (Oxford University Press, Jan. 2012), pp. 1–784.

[17]W. E. Morrell and J. H. Hildebrand, “The distribution of molecules in a model liquid”, The Journal of Chemical Physics **4**, 224–227 (1936).

[18]H. Temperley, J. Rowlinson, and G. Rushbrooke, *Physics of simple liquids* (North-Holland Publishing Company, 1968).

[19]L. Sarolea and J. E. Mayer, “Integral equation method in the theory of liquids”, Phys. Rev. **101**, 1627–1640 (1956).

[20]K. E. Gubbins, “Perturbation methods for calculating properties of liquid mixtures”, AIChE Journal **19**, 684–698 (1973).

[21]I. Z. Fisher, *Statistical theory of liquids* (University of Chicago Press, 1965), p. 335.

[22]P. Egelstaff, *An introduction to the liquid state*, Oxford science publications (Clarendon Press, 1994).

[23]S. P. Das, *Statistical physics of liquids at freezing and beyond* (Cambridge University Press, 2011).

[24]J.-P. Hansen and I. McDonald, *Theory of simple liquids: with applications to soft matter; 4th ed.* (Academic Press, New York, NY, 2013).

[25]J.-L. Barrat and J.-P. Hansen, *Basic concepts for simple and complex liquids* (Cambridge University Press, 2003).

[26]W. Schirmacher, *Theory of liquids and other disordered media*, Vol. 887 (Springer International Publishing Switzerland, Jan. 2015), p. 167.

[27]W. Fawcett, *Liquids, solutions, and interfaces: from classical macroscopic descriptions to modern microscopic details*, OUP E-Books (Oxford University Press, USA, 2004).

[28]D. C. Rapaport, *The art of molecular dynamics simulation*, 2nd ed. (Cambridge University Press, 2004).

[29]G. Raabe, *Molecular simulation studies on thermophysical properties* (Jan. 2017), p. 303.

[30]W. Greiner, L. Neise, H. Stocker, H. Stöcker, and D. Rischke, *Thermodynamics and statistical mechanics*, Classical theoretical physics (Springer-Verlag, 1995).

[31]P. Balbuena and J. Seminario, *Molecular dynamics: from classical to quantum methods*, ISSN (Elsevier Science, 1999).

[32]J. Thijssen, *Computational physics*, 2nd ed. (Cambridge University Press, 2007).

[33]J. Haile, *Molecular dynamics simulation: elementary methods* (Wiley, 1997).

[34]A. Barnes, W. Orville-Thomas, and J. Yarwood, *Molecular liquids: dynamics and interactions*, Nato Science Series C: (Springer Netherlands, 2012).

[35]N. Metropolis, A. W. Rosenbluth, M. N. Rosenbluth, A. H. Teller, and E. Teller, "Equation of state calculations by fast computing machines", The Journal of Chemical Physics **21**, 1087–1092 (1953).

[36]T. Pang, *An introduction to computational physics*, 2nd (Cambridge University Press, New York, NY, USA, 2010).

[37]P. Strathern, *Turing e o computador em 90 minutos*, Cientistas em 90 Minutos (Zahar, 2000).

[38]P. Deuflhard, J. Hermans, I. Modelling, B. Leimkuhler, A. Mark, S. Reich, and R. Skeel, *Computational molecular dynamics: challenges, methods, ideas: proceeding of the 2nd international symposium on algorithms for macromolecular modelling, berlin, may 21–24, 1997*, Algorithms for macromolecular modelling : international symposium (U.S. Government Printing Office, 1999).

[39]D. Frenkel and B. Smit, *Understanding molecular simulation*, 2nd (Academic Press, Inc., Orlando, FL, USA, 2001).

[40]A. R. Leach, *Molecular modelling: principles and applications* (Pearson Education, 2009).

[41]W. C. Swope, H. C. Andersen, P. H. Berens, and K. R. Wilson, "A computer simulation method for the calculation of equilibrium constants for the formation of physical clusters of molecules: application to small water clusters", The Journal of Chemical Physics **76**, 637–649 (1982).

[42]S. Nosé, "A unified formulation of the constant temperature molecular dynamics methods", The Journal of Chemical Physics **81**, 511–519 (1984).

[43]W. G. Hoover, "Canonical dynamics: equilibrium phase-space distributions", Phys. Rev. A **31**, 1695–1697 (1985).

[44]R. Sadus, *Molecular simulation of fluids* (Elsevier Science, 2002).

[45]M. S. Shell, *Coarse graining and multiscale techniques*, `https://sites.engineering.ucsb.edu/~shell/che210d/Multiscale.pdf`, Accessed: 2019-04-30, 2008.

[46]K. Binder, "Monte carlo simulation in polymer physics: some recent developments", Makromolekulare Chemie. Macromolecular Symposia **50**, 1–17 (1991).

[47]J. Baschnagel, K. Binder, P. Doruker, A. A. Gusev, O. Hahn, K. Kremer, W. L. Mattice, F. Muller-Plathe, M. Murat, W. Paul, S. Santos, U. W. Suter, and V. Tries, "Bridging the gap between atomistic and coarse-grained models of polymers: status and perspectives", in *Viscoelasticity, atomistic models, statistical chemistry* (Springer Berlin Heidelberg, Berlin, Heidelberg, 2000), pp. 41–156.

[48]K. Kremer and F. Müller-Plathe, “Multiscale problems in polymer science: simulation approaches”, MRS Bulletin **26**, 205–210 (2001).

[49]M. Kotelyanskii and D. Theodorou, *Simulation methods for polymers* (Taylor & Francis, 2004).

[50]J. Baschnagel, K. Binder, W. Paul, M. Laso, U. W. Suter, I. Batoulis, W. Jilge, and T. Bürger, “On the construction of coarse-grained models for linear flexible polymer chains: distribution functions for groups of consecutive monomers”, The Journal of Chemical Physics **95**, 6014–6025 (1991).

[51]W. Paul, K. Binder, K. Kremer, and D. W. Heermann, “Structure-property correlation of polymers, a monte carlo approach”, Macromolecules **24**, 6332–6334 (1991).

[52]D. Reith, M. Pütz, and F. Müller-Plathe, “Deriving effective mesoscale potentials from atomistic simulations”, Journal of Computational Chemistry **24**, 1624–1636 (2003).

[53]V. A. Harmandaris, N. P. Adhikari, N. F. A. van der Vegt, and K. Kremer, “Hierarchical modeling of polystyrene: from atomistic to coarse-grained simulations”, Macromolecules **39**, 6708–6719 (2006).

[54]K. M. Salerno, A. Agrawal, D. Perahia, and G. S. Grest, “Resolving dynamic properties of polymers through coarse-grained computational studies”, Phys. Rev. Lett. **116**, 058302 (2016).

[55]G. Papoian, *Coarse-grained modeling of biomolecules*, Series in Computational Biophysics (CRC Press, 2017).

[56]M. Dinpajooh and M. G. Guenza, “Coarse-graining simulation approaches for polymer melts: the effect of potential range on computational efficiency”, Soft Matter **14**, 7126–7144 (2018).

[57]D. Fritz, C. R. Herbers, K. Kremer, and N. F. A. van der Vegt, “Hierarchical modeling of polymer permeation”, Soft Matter **5**, 4556–4563 (2009).

[58]T. Schlick, R. Collepardo-Guevara, L. A. Halvorsen, S. Jung, and X. Xiao, "Biomolecular modeling and simulation: a field coming of age", Quarterly Reviews of Biophysics **44**, 191–228 (2011).

[59]W. G. Noid, "Perspective: coarse-grained models for biomolecular systems", The Journal of Chemical Physics **139**, 090901 (2013).

[60]S. Kmiecik, D. Gront, M. Kolinski, L. Wieteska, A. E. Dawid, and A. Kolinski, "Coarse-grained protein models and their applications", Chemical Reviews **116**, PMID: 27333362, 7898–7936 (2016).

[61]A. Puglisi, A. Sarracino, and A. Vulpiani, *Thermodynamics and statistical mechanics of small systems* (MDPI AG, 2018).

[62]S. Izvekov and G. A. Voth, "Multiscale coarse graining of liquid-state systems", The Journal of Chemical Physics **123**, 134105 (2005).

[63]F. Müller-Plathe, "Coarse-graining in polymer simulation: from the atomistic to the mesoscopic scale and back", ChemPhysChem **3**, 754–769 (2002).

[64]J. McCarty, A. J. Clark, I. Y. Lyubimov, and M. G. Guenza, "Thermodynamic consistency between analytic integral equation theory and coarse-grained molecular dynamics simulations of homopolymer melts", Macromolecules **45**, 8482–8493 (2012).

[65]M. Neri, C. Anselmi, M. Cascella, A. Maritan, and P. Carloni, "Coarse-grained model of proteins incorporating atomistic detail of the active site", Phys. Rev. Lett. **95**, 218102 (2005).

[66]G. Voth Ed, S. Marrink, M. Fuhrmans, H. Risselada, and X. Periole, *Coarse-graining of condensed phase and biomolecular systems* (CRC Press, Jan. 2008), p. 456.

[67]M. Praprotnik, L. D. Site, and K. Kremer, "Multiscale simulation of soft matter: from scale bridging to adaptive resolution", Annual Review of Physical Chemistry **59**, PMID: 18062769, 545–571 (2008).

[68]M. G. Guenza, “Theoretical models for bridging timescales in polymer dynamics”, Journal of Physics: Condensed Matter **20**, 033101 (2007).

[69]A. P. Lyubartsev and A. Laaksonen, “Calculation of effective interaction potentials from radial distribution functions: a reverse monte carlo approach”, Phys. Rev. E **52**, 3730–3737 (1995).

[70]A. P. Lyubartsev and A. Laaksonen, “On the reduction of molecular degrees of freedom in computer simulations”, in *Novel methods in soft matter simulations* (Springer Berlin Heidelberg, Berlin, Heidelberg, 2004), pp. 219–244.

[71]A. Lyubartsev, A. Mirzoev, L. Chen, and A. Laaksonen, “Systematic coarse-graining of molecular models by the newton inversion method”, Faraday Discuss. **144**, 43–56 (2010).

[72]D. Rosenberger, M. Hanke, and N. Vegt, “Comparison of iterative inverse coarse-graining methods”, The European Physical Journal Special Topics **225**, 1323–1345 (2016).

[73]S. O. Nielsen, C. F. Lopez, G. Srinivas, and M. L. Klein, “A coarse grain model for n-alkanes parameterized from surface tension data”, The Journal of Chemical Physics **119**, 7043–7049 (2003).

[74]T. A. Knotts, N. Rathore, D. C. Schwartz, and J. J. de Pablo, “A coarse grain model for dna”, The Journal of Chemical Physics **126**, 084901 (2007).

[75]H. Goldstein, C. Poole, and J. Safko, *Classical mechanics* (Addison Wesley, 2002).

[76]J. Barker, R. Fisher, and R. Watts, “Liquid argon: monte carlo and molecular dynamics calculations”, Molecular Physics **21**, 657–673 (1971).

[77]G. Marcelli and R. J. Sadus, “Molecular simulation of the phase behavior of noble gases using accurate two-body and three-body intermolecular potentials”, The Journal of Chemical Physics **111**, 1533–1540 (1999).

[78]C. F. Tejero, A. Daanoun, H. N. W. Lekkerkerker, and M. Baus, “Phase diagrams of "simple" fluids with extreme pair potentials”, Phys. Rev. Lett. **73**, 752–755 (1994).

[79]P. Bolhuis and D. Frenkel, "Prediction of an expanded-to-condensed transition in colloidal crystals", Phys. Rev. Lett. **72**, 2211–2214 (1994).

[80]E. A. Jagla, "Phase behavior of a system of particles with core collapse", Phys. Rev. E **58**, 1478–1486 (1998).

[81]P. C. Hemmer and G. Stell, "Fluids with several phase transitions", Phys. Rev. Lett. **24**, 1284–1287 (1970).

[82]G. Stell and P. C. Hemmer, "Phase transitions due to softness of the potential core", The Journal of Chemical Physics **56**, 4274–4286 (1972).

[83]H. E. Stanley, P. Kumar, G. Franzese, L. Xu, Z. Yan, M. G. Mazza, S. V. Buldyrev, S. H. Chen, and F. Mallamace, "Liquid polyamorphism: possible relation to the anomalous behaviour of water", Eur. Phys. J. Special Topics **161**, 1–17 (2008).

[84]P. G. Debenedetti, V. S. Raghavan, and S. S. Borick, "Spinodal curve of some supercooled liquids", The Journal of Physical Chemistry **95**, 4540–4551 (1991).

[85]E. A. Jagla, "Core-softened potentials and the anomalous properties of water", The Journal of Chemical Physics **111**, 8980–8986 (1999).

[86]E. A. Jagla, "Low-temperature behavior of core-softened models: water and silica behavior", Phys. Rev. E **63**, 061509 (2001).

[87]P. H. Poole, F. Sciortino, U. Essmann, and H. E. Stanley, "Phase behaviour of metastable water", Nature **360**, 324–328 (1992).

[88]M. R. Sadr-Lahijany, A. Scala, S. V. Buldyrev, and H. E. Stanley, "Liquid-state anomalies and the stell-hemmer core-softened potential", Phys. Rev. Lett. **81**, 4895–4898 (1998).

[89]A. Scala, F. W. Starr, E. La Nave, H. E. Stanley, and F. Sciortino, "Free energy surface of supercooled water", Phys. Rev. E **62**, 8016–8020 (2000).

[90]A. Lopes Balladares and M. Barbosa, "Density anomaly in core-softened lattice gas", Journal of Physics: Condensed Matter **16**, 8811–8822 (2004).

[91]G. Franzese, G. Malescio, A. Skibinsky, S. Buldyrev, and H. Stanley, "Generic mechanism for generating a liquid-liquid phase transition", Nature **409**, `10.1038/35055514` (2001).

[92]E. A. Jagla, "The interpretation of water anomalies in terms of core-softened models", Brazilian Journal of Physics **34**, `10.1590/S0103-97332004000100003` (2004).

[93]L. Xu, P. Kumar, S. V. Buldyrev, S.-H. Chen, P. H. Poole, F. Sciortino, and H. E. Stanley, "Relation between the widom line and the dynamic crossover in systems with a liquid–liquid phase transition", Proceedings of the National Academy of Sciences **102**, 16558–16562 (2005).

[94]A. Barros de Oliveira, P. A. Netz, T. Colla, and M. C. Barbosa, "Thermodynamic and dynamic anomalies for a three-dimensional isotropic core-softened potential", The Journal of Chemical Physics **124**, 084505 (2006).

[95]P. Vilaseca and G. Franzese, "Softness dependence of the anomalies for the continuous shouldered well potential", The Journal of Chemical Physics **133**, 084507 (2010).

[96]F. Hussain, M. Hojjati, M. Okamoto, and R. E. Gorga, "Review article: polymer-matrix nanocomposites, processing, manufacturing, and application: an overview", Journal of Composite Materials **40**, 1511–1575 (2006).

[97]R. Borst and T. Sadowski, *Lecture notes on composite materials. current topics and achievements*, Vol. 154 (Jan. 2009).

[98]K. I. Winey and R. A. Vaia, "Polymer nanocomposites", MRS Bulletin **32**, 314–322 (2007).

[99]R. Jones, *Mechanics of composite materials*, Materials Science and Engineering Series (Taylor & Francis, 1998).

[100]E. R. Littmann, "Maya blue—a new perspective", American Antiquity **45**, 87–100 (1980).

[101]A. C. Balazs, T. Emrick, and T. P. Russell, "Nanoparticle polymer composites: where two small worlds meet", Science **314**, 1107–1110 (2006).

[102]H.-H. Görtz and T. Breiner, “Nanocomposites science and technology. by pulickel m. ajayan, linda s. schadler, and paul v. braun.”, Angewandte Chemie International Edition **43**, 1909–1910 (2004).

[103]A. Usuki, Y. Kojima, M. Kawasumi, A. Okada, Y. Fukushima, T. Kurauchi, and O. Kamigaito, “Synthesis of nylon 6-clay hybrid”, Journal of Materials Research **8**, 1179–1184 (1993).

[104]Y. Kojima, A. Usuki, M. Kawasumi, A. Okada, Y. Fukushima, T. Kurauchi, and O. Kamigaito, “Mechanical properties of nylon 6-clay hybrid”, Journal of Materials Research **8**, 1185–1189 (1993).

[105]V. Vasiliev and E. Morozov, *Advanced mechanics of composite materials and structural elements: third edition* (July 2013).

[106]Andrew McWilliams, *Nanocomposites, nanoparticles, nanoclays and nanotubes: global markets to 2022.bcc research report*, `https://www.bccresearch.com/market-research/nanotechnology/nanocomposites-nanoparticles-nanoclays-and-nanotubes-global-markets.html`, [Online; accessed 05-August-2019], 2018.

[107]Andrew McWilliams, *Polymer nanocomposite market - growth, trends, and forecast (2019 - 2024).* `https://www.mordorintelligence.com/industry-reports/polymer-nanocomposite-market`, [Online; accessed 27-July-2019], 2018.

[108]R. Pujala, *Dispersion stability, microstructure and phase transition of anisotropic nanodiscs*, Springer Theses (Springer International Publishing, 2014).

[109]J. Dhont, *An introduction to dynamics of colloids*, Studies in Interface Science (Elsevier Science, 1996).

[110]T. Graham, “Liquid diffusion applied to analysis”, Philosophical Transactions of the Royal Society of London **151**, 183–224 (1861).

[111]W. Norde, *Colloids and interfaces in life sciences and bionanotechnology: second edition* (June 2011), pp. 1–466.

[112]A. Philipse, *Brownian motion: elements of colloid dynamics*, Undergraduate Lecture Notes in Physics (Springer International Publishing, 2018).

[113] P. Achinstein, "Evidence for molecules: jean perrin and molecular reality", in (Oct. 2001), pp. 243–265.

[114] A. Einstein, "Zur theorie der brownschen bewegung", Annalen der Physik **324**, 371–381 (1906).

[115] D. S. Lemons and A. Gythiel, "Paul langevin's 1908 paper "on the theory of brownian motion" ["sur la théorie du mouvement brownien," c. r. acad. sci. (paris) 146, 530–533 (1908)]", American Journal of Physics **65**, 1079–1081 (1997).

[116] L. Onsager, "Theories of concentrated electrolytes.", Chemical Reviews **13**, 73–89 (1933).

[117] L. Onsager, "The effects of shape on the interaction of colloidal particles", Annals of the New York Academy of Sciences **51**, 627–659 (1949).

[118] W. G. McMillan and J. E. Mayer, "The statistical thermodynamics of multicomponent systems", The Journal of Chemical Physics **13**, 276–305 (1945).

[119] A. Fernandez-Nieves and A. Puertas, *Fluids, colloids and soft materials: an introduction to soft matter physics*, Wiley Series on Surface and Interfacial Chemistry (Wiley, 2016).

[120] H. N. W. Lekkerkerker and R. Tuinier, *Colloids and the depletion interaction*, Vol. p. 233 (May 2011).

[121] I. Hamley, *Introduction to soft matter: synthetic and biological self-assembling materials* (Wiley, 2008).

[122] B. Derjaguin and L. Landau, "Theory of the stability of strongly charged lyophobic sols and of the adhesion of strongly charged particles in solutions of electrolytes", Progress in Surface Science **43**, 30–59 (1993).

[123] E. J. W. Verwey, "Theory of the stability of lyophobic colloids.", The Journal of Physical and Colloid Chemistry **51**, 631–636 (1947).

[124] J. Gregory, "Polymers at interfaces, by g. j. fleer, m. a. cohen stuart, j. m. h. m. scheutjens, t. cosgrove and b. vincent. chapman and hall, london, 1993. pp. xv + 502, price £65.00. isbn 0-412-58160-4", Polymer International **36**, 102–102 (1995).

[125]D. Napper and A. Netschey, “Studies of the steric stabilization of colloidal particles”, Journal of Colloid and Interface Science **37**, 528–535 (1971).

[126]R. Jones, P. R Jones, and R. Jones, *Soft condensed matter*, Oxford Master Series in Physics (OUP Oxford, 2002).

[127]C. M. Wijmans, E. B. Zhulina, and G. J. Fleer, “Effect of free polymer on the structure of a polymer brush and interaction between two polymer brushes”, Macromolecules **27**, 3238–3248 (1994).

[128]B. Zhao and L. Zhu, “Mixed polymer brush-grafted particles: a new class of environmentally responsive nanostructured materials”, Macromolecules **42**, 9369–9383 (2009).

[129]C. M. Hui, J. Pietrasik, M. Schmitt, C. Mahoney, J. Choi, M. R. Bockstaller, and K. Matyjaszewski, “Surface-initiated polymerization as an enabling tool for multifunctional (nano-)engineered hybrid materials”, Chemistry of Materials **26**, 745–762 (2014).

[130]S. K. Kumar, N. Jouault, B. Benicewicz, and T. Neely, “Nanocomposites with polymer grafted nanoparticles”, Macromolecules **46**, 3199–3214 (2013).

[131]S. K. Kumar, B. C. Benicewicz, R. A. Vaia, and K. I. Winey, “50th anniversary perspective: are polymer nanocomposites practical for applications?”, Macromolecules **50**, 714–731 (2017).

[132]N. J. Fernandes, H. Koerner, E. P. Giannelis, and R. A. Vaia, “Hairy nanoparticle assemblies as one-component functional polymer nanocomposites: opportunities and challenges”, MRS Communications **3**, 13–29 (2013).

[133]L. Zhang, H. P. Bei, Y. Piao, Y. Wang, M. Yang, and X. Zhao, “Polymer-brush-grafted mesoporous silica nanoparticles for triggered drug delivery”, ChemPhysChem **19**, 1956–1964 (2018).

[134]J. He, X. Huang, Y.-C. Li, Y. Liu, T. Babu, M. A. Aronova, S. Wang, Z. Lu, X. Chen, and Z. Nie, “Self-assembly of amphiphilic plasmonic micelle-like nanoparti-

cles in selective solvents", Journal of the American Chemical Society **135**, PMID: 23642094, 7974–7984 (2013).

[135]G. Liu, Z. Liu, N. Li, X. Wang, F. Zhou, and W. Liu, "Hairy polyelectrolyte brushes-grafted thermosensitive microgels as artificial synovial fluid for simultaneous biomimetic lubrication and arthritis treatment", ACS Applied Materials & Interfaces **6**, PMID: 25347384, 20452–20463 (2014).

[136]A. J. Chancellor, B. T. Seymour, and B. Zhao, "Characterizing polymer-grafted nanoparticles: from basic defining parameters to behavior in solvents and self-assembled structures", Analytical Chemistry **91**, PMID: 31013073, 6391–6402 (2019).

[137]C. Tian, C. Bao, A. Binder, Z. Zhu, B. Hu, Y. Guo, B. Zhao, and S. Dai, "An efficient and reusable 'hairy' particle acid catalyst for the synthesis of 5-hydroxymethylfurfural from dehydration of fructose in water", Chem. Commun. **49**, 8668–8670 (2013).

[138]K. Ohno, T. Morinaga, K. Koh, Y. Tsujii, and T. Fukuda, "Synthesis of monodisperse silica particles coated with well-defined, high-density polymer brushes by surface-initiated atom transfer radical polymerization", Macromolecules **38**, 2137–2142 (2005).

[139]C. Li, J. Han, C. Y. Ryu, and B. C. Benicewicz, "A versatile method to prepare raft agent anchored substrates and the preparation of pmma grafted nanoparticles", Macromolecules **39**, 3175–3183 (2006).

[140]Y.-Z. You, K. K. Kalebaila, S. L. Brock, and D. Oupický, "Temperature-controlled uptake and release in pnipam-modified porous silica nanoparticles", Chemistry of Materials **20**, 3354–3359 (2008).

[141]M. Yavuz, J. Chen, C. Cobley, Q. Zhang, M. Rycenga, J. Xie, C. Kim, K. Song, A. Schwartz, L. Wang, and Y. Xia, "Gold nanocages covered by smart polymers for controlled release with near-infrared light", Nature materials **8**, 935–9 (2009).

[142]J. W. Hotchkiss, A. B. Lowe, and S. G. Boyes, "Surface modification of gold nanorods with polymers synthesized by reversible addition-fragmentation chain transfer polymerization", Chemistry of Materials **19**, 6–13 (2007).

[143]M.-Q. Zhu, L.-Q. Wang, G. J. Exarhos, and A. D. Q. Li, “Thermosensitive gold nanoparticles”, Journal of the American Chemical Society **126**, PMID: 14995155, 2656–2657 (2004).

[144]P. Chmielarz, J. Yan, P. Krys, Y. Wang, Z. Wang, M. R. Bockstaller, and K. Matyjaszewski, “Synthesis of nanoparticle copolymer brushes via surface-initiated seatrp”, Macromolecules **50**, 4151–4159 (2017).

[145]R. A. E. Wright, D. M. Henn, and B. Zhao, “Thermally reversible physically crosslinked hybrid network hydrogels formed by thermosensitive hairy nanoparticles”, The Journal of Physical Chemistry B **120**, PMID: 27455167, 8036–8045 (2016).

[146]C. Bao, S. Tang, J. M. Horton, X. Jiang, P. Tang, F. Qiu, L. Zhu, and B. Zhao, “Effect of overall grafting density on microphase separation of mixed homopolymer brushes synthesized from y-initiator-functionalized silica particles”, Macromolecules **45**, 8027–8036 (2012).

[147]C. Bao, S. Tang, R. A. E. Wright, P. Tang, F. Qiu, L. Zhu, and B. Zhao, “Effect of molecular weight on lateral microphase separation of mixed homopolymer brushes grafted on silica particles”, Macromolecules **47**, 6824–6835 (2014).

[148]L. Wu, U. Glebe, and A. Böker, “Synthesis of polystyrene and poly(4-vinylpyridine) mixed grafted silica nanoparticles via a combination of atrp and cui-catalyzed azide-alkyne click chemistry”, Macromolecular Rapid Communications **38**, 1600475 (2017).

[149]S. R. Edgecombe, J. M. Gardiner, and M. W. Matsen, “Suppressing autophobic dewetting by using a bimodal brush”, Macromolecules **35**, 6475–6477 (2002).

[150]D. L. Green and J. Mewis, “Connecting the wetting and rheological behaviors of poly(dimethylsiloxane)-grafted silica spheres in poly(dimethylsiloxane) melts”, Langmuir **22**, PMID: 17073478, 9546–9553 (2006).

[151]L. Yezek, W. Schärtl, Y. Chen, K. Gohr, and M. Schmidt, “Influence of hair density and hair length on interparticle interactions of spherical polymer brushes in a homopolymer matrix”, Macromolecules **36**, 4226–4235 (2003).

[152]M. Matsen and J. Gardiner, “Autophobic dewetting of homopolymer on a brush and entropic attraction between opposing brushes in a homopolymer matrix”, Journal of Chemical Physics **115**, 2794–2804 (2001).

[153]D. Dukes, Y. Li, S. Lewis, B. Benicewicz, L. Schadler, and S. K. Kumar, “Conformational transitions of spherical polymer brushes: synthesis, characterization, and theory”, Macromolecules **43**, 1564–1570 (2010).

[154]P. F. Green, “The structure of chain end-grafted nanoparticle/homopolymer nanocomposites”, Soft Matter **7**, 7914–7926 (2011).

[155]C. Cabane, K. Wong, and R. Duplessix, “Macromolecules for control of distances in colloidal dispersions”, in *Polymer association structures* (American Chemical Society, 1989) Chap. 19, pp. 312–327.

[156]E. Dickinson, “Colloid science of mixed ingredients”, Soft Matter **2**, 642–652 (2006).

[157]J. M. Brader, “Nonlinear rheology of colloidal dispersions”, Journal of Physics: Condensed Matter **22**, 363101 (2010).

[158]P. G. de Gennes, “Conformations of polymers attached to an interface”, Macromolecules **13**, 1069–1075 (1980).

[159]R. Larson and R. Larson, *The structure and rheology of complex fluids*, Topics in Chemical Engineering (OUP USA, 1999).

[160]M. E. Mackay, A. Tuteja, P. M. Duxbury, C. J. Hawker, B. Van Horn, Z. Guan, G. Chen, and R. S. Krishnan, “General strategies for nanoparticle dispersion”, Science **311**, 1740–1743 (2006).

[161]S. Srivastava, P. Agarwal, and L. A. Archer, “Tethered nanoparticle–polymer composites: phase stability and curvature”, Langmuir **28**, PMID: 22439646, 6276–6281 (2012).

[162]U. Yamamoto and K. S. Schweizer, “Theory of nanoparticle diffusion in unentangled and entangled polymer melts”, The Journal of Chemical Physics **135**, 224902 (2011).

[163]A. Tuteja, P. M. Duxbury, and M. E. Mackay, “Polymer chain swelling induced by dispersed nanoparticles”, Phys. Rev. Lett. **100**, 077801 (2008).

[164]R. Krishnamoorti, “Strategies for dispersing nanoparticles in polymers”, MRS Bulletin **32**, 341–347 (2007).

[165]A. Bansal, H. Yang, C. Li, K. Cho, B. C. Benicewicz, S. K. Kumar, and L. S. Schadler, “Quantitative equivalence between polymer nanocomposites and thin polymer films”, Nature Materials **4**, 693–698 (2005).

[166]F. Sciortino, S. Mossa, E. Zaccarelli, and P. Tartaglia, “Equilibrium cluster phases and low-density arrested disordered states: the role of short-range attraction and long-range repulsion”, Phys. Rev. Lett. **93**, 055701 (2004).

[167]P. Akcora, H. Liu, S. K. Kumar, J. F. Moll, Y. B. Li, B. C. Benicewicz, L. Schadler, D. Acehan, A. Z. Panagiotopoulos, V. A. Pryamitsyn, V. Ganesan, J. Ilavsky, P. Thiyagarajan, R. H. Colby, and J. F. Douglas, “Anisotropic self-assembly of spherical polymer-grafted nanoparticles.”, Nature materials **8 4**, 354–9 (2009).

[168]D. Meng, S. K. Kumar, J. M. D. Lane, and G. S. Grest, “Effective interactions between grafted nanoparticles in a polymer matrix”, Soft Matter **8**, 5002–5010 (2012).

[169]J. Shen, J. Liu, Y. Gao, D. Cao, and L. Zhang, “Revisiting the dispersion mechanism of grafted nanoparticles in polymer matrix: a detailed molecular dynamics simulation”, Langmuir **27**, PMID: 22040300, 15213–15222 (2011).

[170]A. Chremos and A. Z. Panagiotopoulos, “Structural transitions of solvent-free oligomer-grafted nanoparticles”, Phys. Rev. Lett. **107**, 105503 (2011).

[171]S. Goyal and F. A. Escobedo, “Structure and transport properties of polymer grafted nanoparticles”, The Journal of Chemical Physics **135**, 184902 (2011).

[172]T. Lafitte, S. K. Kumar, and A. Z. Panagiotopoulos, “Self-assembly of polymer-grafted nanoparticles in thin films”, Soft Matter **10**, 786–794 (2014).

[173]N. K. Hansoge, A. Gupta, H. White, A. Giuntoli, and S. Keten, “Universal relation for effective interaction between polymer-grafted nanoparticles”, Macromolecules **54**, 3052–3064 (2021).

[174]V. Ganesan and A. Jayaraman, “Theory and simulation studies of effective interactions, phase behavior and morphology in polymer nanocomposites”, Soft Matter **10**, 13–38 (2014).

[175]Y.-L. Lin, C.-S. Chiou, S. K. Kumar, J.-J. Lin, Y.-J. Sheng, and H.-K. Tsao, “Self-assembled superstructures of polymer-grafted nanoparticles: effects of particle shape and matrix polymer”, The Journal of Physical Chemistry C **115**, 5566–5577 (2011).

[176]J. Stellbrink, *Soft colloids and gels*, `https://www.fz-juelich.de/jcns/jcns-1/EN/Forschung/Soft-colloids/_node.html`, Accessed: 2019-08-15, 2017.

[177]P. Kumar and K. Mittal, *Handbook of microemulsion science and technology* (Taylor & Francis, 1999).

[178]D. Banerjee, B. A. Lindquist, R. B. Jadrich, and T. M. Truskett, “Assembly of particle strings via isotropic potentials”, The Journal of Chemical Physics **150**, 124903 (2019).

[179]M. J. A. Hore, “Polymers on nanoparticles: structure and dynamics”, Soft Matter **15**, 1120–1134 (2019).

[180]K. Volk, F. Deißenbeck, S. Mandal, H. Löwen, and M. Karg, “Moiré and honeycomb lattices through self-assembly of hard-core/soft-shell microgels: experiment and simulation”, Phys. Chem. Chem. Phys., `10.1039/C9CP03116B` (2019).

[181]B. Hong, A. Chremos, and A. Z. Panagiotopoulos, “Simulations of the structure and dynamics of nanoparticle-based ionic liquids”, Faraday Discuss. **154**, 29–40 (2012).

[182]J.-P. Ryckaert, G. Ciccotti, and H. J. Berendsen, “Numerical integration of the cartesian equations of motion of a system with constraints: molecular dynamics of n-alkanes”, Journal of Computational Physics **23**, 327–341 (1977).

[183] H. Limbach, A. Arnold, B. Mann, and C. Holm, “Espresso—an extensible simulation package for research on soft matter systems”, Computer Physics Communications **174**, 704–727 (2006).

[184] T. Head-Gordon and F. H. Stillinger, “An orientational perturbation theory for pure liquid water”, The Journal of Chemical Physics **98**, 3313–3327 (1993).

[185] Z. Yan, S. V. Buldyrev, P. Kumar, N. Giovambattista, and H. E. Stanley, “Correspondence between phase diagrams of the tip5p water model and a spherically symmetric repulsive ramp potential with two characteristic length scales”, Phys. Rev. E **77**, 042201 (2008).

[186] N. G. Almarza, E. Lomba, and D. Molina, “Determination of effective pair interactions from the structure factor”, Phys. Rev. E **70**, 021203 (2004).

[187] N. M. Barraz, E. Salcedo, and M. C. Barbosa, “Thermodynamic, dynamic, and structural anomalies for shoulderlike potentials”, The Journal of Chemical Physics **131**, 094504 (2009).

[188] S. Plimpton, “Fast parallel algorithms for short-range molecular dynamics”, Journal of Computational Physics **117**, 1–19 (1995).

[189] J. R. Bordin and L. B. Krott, “Confinement effects on the properties of janus dimers”, Phys. Chem. Chem. Phys. **16**, 28740–28746 (2016).

[190] L. B. Krott, C. Gavazzoni, and J. R. Bordin, “Anomalous diffusion and diffusion anomaly in confined janus dumbbells”, J. Chem. Phys. **145**, 244906 (2016).

[191] J. R. Bordin and M. C. Barbosa, “Waterlike anomalies in a two-dimensional core-softened potential”, Phys. Rev. E **97**, 022604 (2018).

[192] E. Salcedo, N. M. Barraz, and M. C. Barbosa, “Relation between occupation in the first coordination shells and widom line in core-softened potentials”, The Journal of Chemical Physics **138**, 164502 (2013).

[193] G. M. Viswanathan, E. P. Raposo, and M. G. E. da Luz, *Perspectives and challenges in statistical physics and complex systems for the next decade* (WORLD SCIENTIFIC, 2014).

[194]M. Szortyka, M. Girardi, V. Henriques, and M. C. Barbosa, “Liquid polimorphism, order-disorder transitions and anomalous behavior: a monte carlo study of the bell-lavis model for water”, J. Chem. Phys. **130**, 184902 (2009).

[195]J. R. Bordin and L. B. Krott, “How competitive interactions affect the self-assembly of confinedjanus dumbbells”, J. Phys. Chem. B **121**, 4308–4317 (2017).

[196]S. Prestipino, F. Saija, and P. V. Giaquinta, “Anomalous phase behavior in a model fluid with only one type of local structure”, J. Chem. Phys. **133**, 144504 (2010).

[197]S. Prestipino, F. Saija, and P. V. Giaquinta, “Hexatic phase in the two-dimensional gaussian-core model”, Phys. Rev. Lett. **106**, 235701 (2011).

[198]G. Malescio and G. Pellicane, “Stripe phases from isotropic repulsive interactions”, Nature materials **2**, 97–100 (2003).

[199]G. Malescio and G. Pellicane, “Stripe patterns in two-dimensional systems with core-corona molecular architecture”, Phys. Rev. E **70**, 021202 (2004).

[200]F. Franks and D. J. G. Ives, “The structural properties of alcohol–water mixtures”, Q. Rev. Chem. Soc. **20**, 1–44 (1966).

[201]F. Franks, *Water: A Matrix of Life* (Royal Society of Chemistry, Cambridge, 2000).

[202]R. Lynden-Bell, S. Morris, J. Barrow, and J. Finney, *Water and life: the unique properties of h2o* (CRC Press, 2010).

[203]K. A. Sharp, “Water: structure and properties”, in *Encyclopedia of life sciences* (American Cancer Society, 2001).

[204]M. Chaplin, *Anomalous properties of water*, `http://www.lsbu.ac.uk/water/anmlies.html`, July 2020.

[205]A. Nilsson and L. Pettersson, “The structural origin of anomalous properties of liquid water”, Nature Communications **6**, 8998 (2015).

[206]P. G. Debenedetti, “Supercooled and glassy water”, J. Phys.: Cond. Matter **15**, 1669 (2003).

[207]P. Gallo, K. Amann-Winkel, C. A. Angell, M. A. Anisimov, F. Caupin, C. Chakravarty, E. Lascaris, T. Loerting, A. Z. Panagiotopoulos, J. Russo, J. A. Sellberg, H. E. Stanley, H. Tanaka, C. Vega, L. Xu, and L. G. M. Pettersson, “Water: A Tale of Two Liquids”, Chemical Reviews **116**, 7463–7500 (2016).

[208]P. H. Handle, T. Loerting, and F. Sciortino, “Supercooled and glassy water: Metastable liquid(s), amorphous solid(s), and a no-man’s land”, Proceedings of the National Academy of Sciences **114**, 13336–13344 (2017).

[209]J. A. Sellberg, C. Huang, T. A. McQueen, N. D. Loh, H. Laksmono, D. Schlesinger, R. G. Sierra, D. Nordlund, C. Y. Hampton, D. Starodub, D. P. DePonte, M. Beye, C. Chen, A. V. Martin, A. Barty, K. T. Wikfeldt, T. M. Weiss, C. Caronna, J. Feldkamp, L. B. Skinner, M. M. Seibert, M. Messerschmidt, G. J. Williams, S. Boutet, L. G. M. Pettersson, M. J. Bogan, and A. Nilsson, “Ultrafast X-ray probing of water structure below the homogeneous ice nucleation temperature”, Nature **510**, 381–384 (2014).

[210]Z. Sun, G. Sun, Y. Chen, and L. Xu, “Liquid-liquid phase transition in water”, Science China Physics, Mechanics & Astronomy **57**, 810–818 (2014).

[211]R. Podgornik, “Water and life: the unique properties of h2o: ruth m. lynden-bell, simon conway morris, john d. barrow, john l. finney and charles harper (eds). crc press; 1 edition, 2010”, Journal of Biological Physics **37**, `10.1007/s10867-011-9217-9` (2011).

[212]G. S. Kellu, “Density, thermal expansivity, and compressibility of liquid water from 0.deg. to 150.deg.. correlations and tables for atmospheric pressure and saturation reviewed and expressed on 1968 temperature scale.”, J. Chem. Eng. Data **20**, 97–105 (1975).

[213]P. Poole, F. Sciortino, U. Essmann, and H. Stanley, “Phase-behavior of metastable water”, Nature **360**, 324–328 (1992).

[214]D. T. Limmer and D. Chandler, “The putative liquid-liquid transition is a liquid-solid transition in atomistic models of water”, The Journal of Chemical Physics **135**, 134503 (2011).

[215]D. T. Limmer and D. Chandler, “The putative liquid-liquid transition is a liquid-solid transition in atomistic models of water. ii”, The Journal of Chemical Physics **138**, 214504 (2013).

[216]P. H. Poole, R. K. Bowles, I. Saika-Voivod, and F. Sciortino, “Free energy surface of st2 water near the liquid-liquid phase transition”, The Journal of Chemical Physics **138**, 034505 (2013).

[217]J. C. Palmer, R. Car, and P. G. Debenedetti, “The liquid–liquid transition in supercooled st2 water: a comparison between umbrella sampling and well-tempered metadynamics”, Faraday Discuss. **167**, 77–94 (2013).

[218]J. C. Palmer, A. Haji-Akbari, R. S. Singh, F. Martelli, R. Car, A. Z. Panagiotopoulos, and P. G. Debenedetti, “Comment on “the putative liquid-liquid transition is a liquid-solid transition in atomistic models of water” [i and ii: j. chem. phys. 135, 134503 (2011); j. chem. phys. 138, 214504 (2013)]”, The Journal of Chemical Physics **148**, 137101 (2018).

[219]F. Caupin, “Escaping the no man’s land: recent experiments on metastable liquid water”, Journal of Non-Crystalline Solids **407**, 7th IDMRCS: Relaxation in Complex Systems, 441–448 (2015).

[220]A. Taschin, P. Bartolini, R. Eramo, R. Righini, and R. Torre, “Evidence of two distinct local structures of water from ambient to supercooled conditions”, Nat. Comm. **4**, 2401 (2013).

[221]N. J. Hestand and J. L. Skinner, “Perspective: crossing the widom line in no man’s land: experiments, simulations, and the location of the liquid-liquid critical point in supercooled water”, The Journal of Chemical Physics **149**, 140901 (2018).

[222]J. C. Palmer, P. H. Poole, F. Sciortino, and P. G. Debenedetti, “Advances in computational studies of the liquid–liquid transition in water and water-like models”, Chemical Reviews **118**, PMID: 30152693, 9129–9151 (2018).

[223]Y. Liu, J. C. Palmer, A. Z. Panagiotopoulos, and P. G. Debenedetti, “Liquid-liquid transition in st2 water”, J. Chem. Phys. **137**, 214505 (2012).

[224]Y. Ni and J. L. Skinner, “Evidence for a liquid-liquid critical point in supercooled water within the e3b3 model and a possible interpretation of the kink in the homogeneous nucleation line”, The Journal of Chemical Physics **144**, 214501 (2016).

[225]R. S. Singh, J. W. Biddle, P. G. Debenedetti, and M. A. Anisimov, “Two-state thermodynamics and the possibility of a liquid-liquid phase transition in supercooled tip4p/2005 water”, The Journal of Chemical Physics **144**, 144504 (2016).

[226]C. A. Angell., “Two phases?”, Nat. Mater. **13**, 673–675 (2014).

[227]G. G. Simeoni, T. Bryk, F. A. Gorelli, M. Krisch, G. Ruocco, M. Santoro, and T. Scopigno, “The widom line as the crossover between liquid-like and gas-like behaviour in supercritical fluids”, Nature Physics **6**, 503–507 (2010).

[228]V. V. Brazhkin, Y. D. Fomin, A. G. Lyapin, V. N. Ryzhov, and E. N. Tsiok, “Widom line for the liquid–gas transition in lennard-jones system”, The Journal of Physical Chemistry B **115**, PMID: 21699267, 14112–14115 (2011).

[229]V. Brazhkin, Y. Fomin, V. Ryzhov, E. Tsiok, and K. Trachenko, “Liquid-like and gas-like features of a simple fluid: an insight from theory and simulation”, Physica A: Statistical Mechanics and its Applications **509**, 690–702 (2018).

[230]I. Zerón, J. Torres-Arenas, E. de Jesús, B. Ramírez, and A. Benavides, “Discrete potential fluids in the supercritical region”, Journal of Molecular Liquids **293**, 111518 (2019).

[231]J. Losey and R. J. Sadus, “The widom line and the lennard-jones potential”, The Journal of Physical Chemistry B **123**, PMID: 31498625, 8268–8273 (2019).

[232]V. Bianco and G. Franzese, “Hydrogen bond correlated percolation in a supercooled water monolayer as a hallmark of the critical region”, Journal of Molecular Liquids **285**, 727–739 (2019).

[233]G. Franzese and H. E. Stanley, “The widom line of supercooled water”, Journal of Physics: Condensed Matter **19**, 205126 (2007).

[234]P. Kumar, G. Franzese, and H. E. Stanley, “Dynamics and thermodynamics of water”, Journal of Physics: Condensed Matter **20**, 244114 (2008).

[235] J. L. F. Abascal and C. Vega, "Widom line and the liquid–liquid critical point for the tip4p/2005 water model", The Journal of Chemical Physics **133**, 234502 (2010).

[236] J. Luo, L. Xu, C. A. Angell, H. E. Stanley, and S. V. Buldyrev, "Physics of the jagla model as the liquid-liquid coexistence line slope varies", The Journal of Chemical Physics **142**, 224501 (2015).

[237] P. Gallo, K. Amann-Winkel, C. A. Angell, M. A. Anisimov, F. Caupin, C. Chakravarty, E. Lascaris, T. Loerting, A. Z. Panagiotopoulos, J. Russo, J. A. Sellberg, H. E. Stanley, H. Tanaka, C. Vega, L. Xu, and L. G. M. Pettersson, "Water: a tale of two liquids", Chemical Reviews **116**, PMID: 27380438, 7463–7500 (2016).

[238] E. Smith, *Basic chemical thermodynamics*, Oxford chemistry series (Imperial College Press, 2004).

[239] D. Sherwood and P. Dalby, *Modern thermodynamics for chemists and biochemists* (Oxford University Press, 2018).

[240] R. Berry, S. Rice, and J. Ross, *Physical chemistry* (Oxford University Press, 2000).

[241] R. Mortimer, *Physical chemistry* (Elsevier Science, 2008).

[242] I. Levine, *Physical chemistry*, McGraw-Hill international edition (McGraw-Hill Education, 2009).

[243] R. Hołyst and A. Poniewierski, *Thermodynamics for chemists, physicists and engineers*, SpringerLink : Bücher (Springer Netherlands, 2012).

[244] P. Atkins and J. de Paula, *Atkins' physical chemistry* (OUP Oxford, 2010).

[245] J. O'Connell and J. Haile, *Thermodynamics: fundamentals for applications* (Cambridge University Press, 2005).

[246] J. Prausnitz, R. Lichtenthaler, and E. de Azevedo, *Molecular thermodynamics of fluid-phase equilibria* (Pearson Education, 1998).

[247] P. J. Benson George C.and D'Arcy and O. Kiyohara, "Thermodynamics of aqueous mixtures of nonelectrolytes ii. isobaric heat capacities of water-n-alcohol mixtures at 25c", Journal of Solution Chemistry **9**, 931–938 (1980).

[248]N. C. Patel and S. I. Sandler, “Excess volumes of the water/methanol, n-heptane/ethyl acetate, n-heptane/n-butyraldehyde, and n-heptane/isobutyraldehyde systems”, Journal of Chemical & Engineering Data **30**, 218–222 (1985).

[249]S. Dixit, J. Crain, W. C. K. Poon, J. L. Finney, and A. K. Soper, “Molecular segregation observed in a concentrated alcohol-water solution”, Nature **416**, 829–832 (2002).

[250]G. S. Kell, “Density, thermal expansivity, and compressibility of liquid water from 0 to 150 degrees. correlations and tables for atmospheric pressure and saturation reviewed and expressed on 1968 temperature scale”, Journal of Chemical & Engineering Data **20**, 97–105 (1975).

[251]A. J. Darnell and J. Greyson, “Effect of structure-making and -breaking solutes on the temperature of maximum density of water”, The Journal of Physical Chemistry **72**, 3021–3025 (1968).

[252]L. G. Hepler, “Thermal expansion and structure in water and aqueous solutions”, Canadian Journal of Chemistry **47**, 4613–4617 (1969).

[253]M. Tariq, J. M. S. S. Esperança, M. R. C. Soromenho, L. P. N. Rebelo, and J. N. C. Lopes, “Shifts in the temperature of maximum density (tmd) of ionic liquid aqueous solutions”, Phys. Chem. Chem. Phys. **15**, 10960–10970 (2013).

[254]G. Wada and S. Umeda, “Effects of nonelectrolytes on the temperature of the maximum density of water. ii. organic compounds with polar groups”, Bulletin of the Chemical Society of Japan **35**, 1797–1801 (1962).

[255]F. Franks, *Water a comprehensive treatise: volume 4: aqueous solutions of amphiphiles and macromolecules*, Water (Springer US, 2013).

[256]F. Franks and B. Watson, “Maximum density effects in dilute aqueous solutions of alcohols and amines”, Trans. Faraday Soc. **63**, 329–334 (1967).

[257]C. Van Oss, *The properties of water and their role in colloidal and biological systems*, Interface Science and Technology (Elsevier Science, 2008).

[258]K. Nishikawa, H. Hayashi, and T. Iijima, “Temperature dependence of the concentration fluctuation, the kirkwood-buff parameters, and the correlation length of tert-butyl alcohol and water mixtures studied by small-angle x-ray scattering”, The Journal of Physical Chemistry **93**, 6559–6565 (1989).

[259]L. Zoranić, F. Sokolić, and A. Perera, “Microstructure of neat alcohols: a molecular dynamics study”, The Journal of Chemical Physics **127**, 024502 (2007).

[260]D. Subramanian, J. Klauda, J. Leys, and M. Anisimov, “Thermodynamic anomalies and structural fluctuations in aqueous solutions of tertiary butyl alcohol”, Vestn. S.-Peterb. Univ., Ser. 4: Fiz., Khim. **4**, 140–153 (2013).

[261]M. Požar and A. Perera, “Evolution of the micro-structure of aqueous alcohol mixtures with cooling: a computer simulation study”, Journal of Molecular Liquids **248**, 602–609 (2017).

[262]B. Kežić and A. Perera, “Aqueous tert-butanol mixtures: a model for molecular-emulsions”, The Journal of Chemical Physics **137**, 014501 (2012).

[263]B. Bagchi, “The amphiphilic effect: the diverse but intimate world of aqueous binary mixtures”, in *Water in biological and chemical processes: from structure and dynamics to function*, Cambridge Molecular Science (Cambridge University Press, 2013), pp. 243–260.

[264]L. Comez, M. Paolantoni, L. Lupi, P. Sassi, S. Corezzi, A. Morresi, and D. Fioretto, “Hydrophobic hydration in water–tert-butyl alcohol solutions by extended depolarized light scattering”, The Journal of Physical Chemistry B **119**, PMID: 25436859, 9236–9243 (2015).

[265]G. Wada and S. Umeda, “Effects of nonelectrolytes on the temperature of the maximum density of water. i. alcohols”, Bulletin of the Chemical Society of Japan **35**, 646–652 (1962).

[266]G. Wada and S. Umeda, “Effects of nonelectrolytes on the temperature of the maximum density of water. ii. organic compounds with polar groups”, Bulletin of the Chemical Society of Japan **35**, 1797–1801 (1962).

[267]F. Franks, *The physics and physical chemistry of water*, Franks, Felix v. 1 (Springer US, 1972).

[268]M. Beretta, "At the source of western science: the organization of experimentalism at the accademia del cimento (1657-1667)", Notes and Records of the Royal Society of London **54**, 131–151 (2000).

[269]H. S. Frank and M. W. Evans, "Free volume and entropy in condensed systems iii. entropy in binary liquid mixtures; partial molal entropy in dilut e solutions; structure and thermodynamics in aqueous electrolytes", J. Chem. Phys. **13**, 507 (1945).

[270]N. Galamba, "Water's structure around hydrophobic solutes and the iceberg model", The Journal of Physical Chemistry B **117**, PMID: 23360515, 2153–2159 (2013).

[271]T. Lilley and S. Murphy, "The temperature of maximum density of aqueous electrolyte solutions and its relation to the temperature derivative of the partial molar volume of the solute", The Journal of Chemical Thermodynamics **5**, 467–470 (1973).

[272]D. Macdonald, B. Dolan, and J. Hyne, "The influence of substituted alcohols on the temperature of maximum density of water", Journal of Solution Chemistry **5**, 405–416 (1976).

[273]E. S. Kim and K. N. Marsh, "Excess volumes for 2-methyl-2-propanol + water at 5 k intervals from 303.15 to 323.15 k", Journal of Chemical & Engineering Data **33**, 288–292 (1988).

[274]S. Chatterjee, H. S. Ashbaugh, and P. G. Debenedetti, "Effects of nonpolar solutes on the thermodynamic response functions of aqueous mixtures", The Journal of Chemical Physics **123**, 164503 (2005).

[275]Z. Su, S. V. Buldyrev, P. G. Debenedetti, P. J. Rossky, and H. E. Stanley, "Modeling simple amphiphilic solutes in a jagla solvent", J. Chem. Phys. **136**, 044511 (2012).

[276] D. González-Salgado, K. Zemánková, E. G. Noya, and E. Lomba, “Temperature of maximum density and excess thermodynamics of aqueous mixtures of methanol”, The Journal of Chemical Physics **144**, 184505 (2016).

[277] A. P. Furlan, E. Lomba, and M. C. Barbosa, “Temperature of maximum density and excess properties of short-chain alcohol aqueous solutions: a simplified model simulation study”, The Journal of Chemical Physics **146**, 144503 (2017).

[278] E. García-Perez, D. González-Salgado, and E. Lomba, “Molecular dynamics simulations of aqueous solutions of short chain alcohols. excess properties and the temperature of maximum density”, to be published (2020).

[279] D. Subramanian and M. A. Anisimov, “Resolving the mystery of aqueous solutions of tertiary butyl alcohol”, The Journal of Physical Chemistry B **115**, PMID: 21671661, 9179–9183 (2011).

[280] F. Aman-Pommier and C. Jallut, “Excess specific volume of water+ tert-butyl alcohol solvent mixtures: experimental data, modeling and derived excess partial specific thermodynamic quantities”, Fluid Phase Equilibria **439**, 43–66 (2017).

[281] “Thermal analysis of the tertiary butyl alcohol-water system and its implications on freeze-drying”, Pharmaceutical Research **12**, 484–490 (1995).

[282] R. Kay, *The physical chemistry of aqueous systems: a symposium in honor of henry s. frank on his seventieth birthday* (Springer US, 2012).

[283] F. H. Stillinger and T. A. Weber, “Computer simulation of local order in condensed phases of silicon”, Phys. Rev. B **31**, 5262–5271 (1985).

[284] V. Molinero and E. B. Moore, “Water modeled as an intermediate element between carbon and silicon”, The Journal of Physical Chemistry B **113**, PMID: 18956896, 4008–4016 (2009).

[285] P. G. Kusalik, A. P. Lyubartsev, D. L. Bergman, and A. Laaksonen, “Computer simulation study of tert-butyl alcohol. 1. structure in the pure liquid”, The Journal of Physical Chemistry B **104**, 9526–9532 (2000).

[286]P. G. Kusalik, A. P. Lyubartsev, D. L. Bergman, and A. Laaksonen, "Computer simulation study of tert-butyl alcohol. 2. structure in aqueous solution", The Journal of Physical Chemistry B **104**, 9533–9539 (2000).

[287]A. H. Nguyen and V. Molinero, "Identification of clathrate hydrates, hexagonal ice, cubic ice, and liquid water in simulations: the chill+ algorithm", J. Phys. Chem. B **119**, 9369–9376 (2014).

[288]V. Molinero, S. Sastry, and C. A. Angell, "Tuning of tetrahedrality in a silicon potential yields a series of monatomic (metal-like) glass formers of very high fragility", Phys. Rev. Lett. **97**, 075701 (2006).

[289]N. I. of Standard and Technology, *2-propanol, 2-methyl*, `https://webbook.nist.gov/cgi/cbook.cgi?ID=C75650&Mask=4`, 2018.

[290]H. L. Pi, J. L. Aragones, C. Vega, E. G. Noya, J. L. Abascal, M. A. Gonzalez, and C. McBride, "Anomalies in water as obtained from computer simulations of the tip4p/2005 model: density maxima, and density, isothermal compressibility and heat capacity minima", Mol. Phys. **107**, 365–374 (2009).

[291]D. T. Bowron, J. L. Finney, and A. K. Soper, "The structure of pure tertiary butanol", Molecular Physics **93**, 531–543 (1998).

[292]Y. Koga, "Excess partial molar enthalpies of water in water-tert-butanol mixtures", Can. J. of Chem. **66**, 3171–3175 (1988).

[293]G. I. Egorov and D. M. Makarov, "Densities and volume properties of (water+tert-butanol) over the temperature range of (274.15 to 348.15)k at pressure of 0.1mpa", J. Chem. Thermod. **43**, 430–441 (2011).

[294]W. G. Hoover, "Canonical dynamics: equilibrium phase-space distributions", Phys. Rev. A **31**, 1695–1697 (1985).

[295]J.-P. Ryckaert, G. Ciccotti, and H. J. Berendsen, "Numerical integration of the cartesian equations of motion of a system with constraints: molecular dynamics of n-alkanes", Journal of Computational Physics **23**, 327–341 (1977).

[296] W. L. Jorgensen, D. S. Maxwell, and J. Tirado-Rives, “Development and testing of the OPLS all-atom force field on conformational energetics and properties of organic liquids”, J. Am. Chem. Soc. **118**, 11225–11236 (1996).

[297] M. A. Gonzalez and J. L. F. Abascal, “A flexible model for water based on tip4p/2005”, J. Chem. Phys. **135**, 224516 (2011).

[298] B. Hess, C. Kutzner, D. van der Spoel, and E. Lindahl, “Gromacs 4: algorithms for highly efficient, load-balanced, and scalable molecular simulation”, J. Chem. Theory Comput. **4**, 435–447 (2008).

[299] M. J. Abraham, T. Murtola, R. Schulz, S. Pall, J. C. Smith, B. Hess, and E. Lindahl, “GROMACS: high performance molecular simulations through multi-level parallelism from laptops to supercomputers”, SoftwareX **1-2**, 19–25 (2015).

[300] H. S. Ashbaugh and H. Bukannan, “Temperature, pressure, and concentration derivatives of nonpolar gas hydration: impact on the heat capacity, temperature of maximum density, and speed of sound of aqueous mixtures”, The Journal of Physical Chemistry B **124**, PMID: 32692557, 6924–6942 (2020).

[301] J. S. Rowlinson and F. L. Swinton, “Chapter 4 - the thermodynamics of liquid mixtures”, in *Liquids and liquid mixtures (third edition)*, edited by J. S. Rowlinson and F. L. Swinton, Third Edition, Butterworths Monographs in Chemistry (Butterworth-Heinemann, 1982), pp. 86–131.

[302] A. Ben-Naim, “Theory of solutions”, in *Statistical thermodynamics for chemists and biochemists* (Springer US, Boston, MA, 1992), pp. 359–457.

[303] C. A. Cerdeiriña, C. A. Tovar, D. González-Salgado, E. Carballo, and L. Romaní, “Isobaric thermal expansivity and thermophysical characterization of liquids and liquid mixtures”, Phys. Chem. Chem. Phys. **3**, 5230–5236 (2001).

[304] K. Zemanková, D. González-Salgado, E. Lomba, and L. Romaní, “Temperature of maximum density for aqueous mixtures of three pentanol isomers”, The Journal of Chemical Thermodynamics **113**, 369–376 (2017).

[305]M.-L. Tan, J. R. Cendagorta, and T. Ichiye, "Effects of microcomplexity on hydrophobic hydration in amphiphiles", Journal of the American Chemical Society **135**, PMID: 23506339, 4918–4921 (2013).

[306]M.-L. Tan, B. T. Miller, J. Te, J. R. Cendagorta, B. R. Brooks, and T. Ichiye, "Hydrophobic hydration and the anomalous partial molar volumes in ethanol-water mixtures", The Journal of Chemical Physics **142**, 064501 (2015).

[307]H. S. Ashbaugh, J. W. Barnett, A. Saltzman, M. Langrehr, and H. Houser, "Connections between the anomalous volumetric properties of alcohols in aqueous solution and the volume of hydrophobic association", The Journal of Physical Chemistry B **122**, PMID: 28968101, 3242–3250 (2018).

[308]H. S. Ashbaugh, J. W. Barnett, A. Saltzman, M. E. Langrehr, and H. Houser, "Stiffening of dilute alcohol and alkane mixtures with water", J. Chem. Phys. **145**, 201102 (2016).

[309]G. Franzese and M. Rubi, *Aspects of physical biology: biological water, protein solutions, transport and replication*, Lecture Notes in Physics (Springer Berlin Heidelberg, 2008).

[310]C. Gray, K. Gubbins, and C. Joslin, *Theory of molecular fluids: volume 2: applications*, International Series of Monographs on Chemistry (OUP Oxford, 2011).

[311]Y. Koga, *Solution thermodynamics and its application to aqueous solutions: a differential approach* (Elsevier Science, 2007).

[312]E. Ruckenstein and I. Shulgin, *Thermodynamics of solutions: from gases to pharmaceutics to proteins*, SpringerLink: Springer e-Books (Springer New York, 2009).

[313]N. K. Hermkens, R. L. Aspers, M. C. Feiters, F. P. Rutjes, and M. Tessari, "Trace analysis in water-alcohol mixtures by continuous p-h2 hyperpolarization at high magnetic field", Magnetic Resonance in Chemistry **56**, 633–640 (2018).

[314]T. V. N. Nguyen, L. Paugam, P. Rabiller, and M. Rabiller-Baudry, "Study of transfer of alcohol (methanol, ethanol, isopropanol) during nanofiltration in water/alcohol mixtures", Journal of Membrane Science **601**, 117907 (2020).

[315]P. Prslja, E. Lomba, P. Gómez-Álvarez, T. Urbic, and E. G. Noya, “Adsorption of water, methanol, and their mixtures in slit graphite pores”, The Journal of Chemical Physics **150**, 024705 (2019).

[316]L. M. Vane, “Review: membrane materials for the removal of water from industrial solvents by pervaporation and vapor permeation”, Journal of Chemical Technology & Biotechnology **94**, 343–365 (2019).

[317]F. Franks, R. S. of Chemistry (Great Britain), and R. S. of Chemistry (Great Britain)., *Water: a matrix of life*, RSC paperbacks (Royal Society of Chemistry, 2000).

[318]N. T. Southall, K. A. Dill, and A. D. J. Haymet, “A view of the hydrophobic effect”, The Journal of Physical Chemistry B **106**, 521–533 (2002).

[319]E. Xi and A. J. Patel, “The hydrophobic effect, and fluctuations: the long and the short of it”, Proceedings of the National Academy of Sciences **113**, 4549–4551 (2016).

[320]M. A. Anisimov, J. V. Sengers, and J. M. [Sengers], “Chapter 2 - near-critical behavior of aqueous systems”, in *Aqueous systems at elevated temperatures and pressures*, edited by D. A. Palmer, R. Fernández-Prini, and A. H. Harvey (Academic Press, London, 2004), pp. 29–71.

[321]H. Stanley, L. Cruz, S. Harrington, P. Poole, S. Sastry, F. Sciortino, F. Starr, and R. Zhang, “Cooperative molecular motions in water: the liquid-liquid critical point hypothesis”, Physica A: Statistical Mechanics and its Applications **236**, Proceedings of the Workshop on Current Problems in Complex Fluids, 19–37 (1997).

[322]O. Mishima and H. Stanley, “The relationship between liquid, supercooled and glassy water”, Nature **396**, `10.1038/24540` (1998).

[323]H. Stanley, S. Buldyrev, O. Mishima, M. Sadr-Lahijany, A. Scala, and F. Starr, “Unsolved mysteries of water in its liquid and glassy phases”, Journal of Physics: Condensed Matter **12**, A403 (2000).

[324] F. Sciortino, E. la Nave, and P. Tartaglia, "Physics of the liquid-liquid critical point", Physical review letters **91**, 155701 (2003).

[325] P. G. Debenedetti, "Supercooled and glassy water", Journal of Physics: Condensed Matter **15**, R1669–R1726 (2003).

[326] P. Debenedetti and H. Stanley, "Supercooled and glassy water", Physics Today **56**, 40–46 (2003).

[327] H. Eugene Stanley, "Liquid and glassy water: two materials of interdisciplinary interest", in *Handbook of materials modeling: methods*, edited by S. Yip (Springer Netherlands, Dordrecht, 2005), pp. 2917–2922.

[328] P. H. Handle, T. Loerting, and F. Sciortino, "Supercooled and glassy water: metastable liquid(s), amorphous solid(s), and a no-man's land", Proceedings of the National Academy of Sciences **114**, 13336–13344 (2017).

[329] H. M. Gibson and N. B. Wilding, "Metastable liquid-liquid coexistence and density anomalies in a core-softened fluid", Phys. Rev. E **73**, 061507 (2006).

[330] J. C. Forman and G. Thodos, "Experimental determination of critical temperatures and pressures of mixtures: the methane-ethane-n-butane system", AIChE Journal **8**, 209–213 (1962).

[331] F. H. Stillinger and E. Helfand, "Critical solution behavior in a binary mixture of gaussian molecules", The Journal of Chemical Physics **41**, 2495–2502 (1964).

[332] J. Levelt Sengers, G. Morrison, and R. Chang, "Critical behavior in fluids and fluid mixtures", Fluid Phase Equilibria **14**, 19–44 (1983).

[333] R. F. Chang and J. M. H. L. Sengers, "Behavior of dilute mixtures near the solvent's critical point", The Journal of Physical Chemistry **90**, 5921–5927 (1986).

[334] Z. Ludmer, R. Shinnar, and V. Yakhot, "Solubility in binary mixtures at the immiscibility critical point", AIChE Journal **33**, 1776–1780 (1987).

[335] J. Jiang and J. M. Prausnitz, "Critical temperatures and pressures for hydrocarbon mixtures from an equation of state with renormalization-group theory corrections", Fluid Phase Equilibria **169**, 127–147 (2000).

[336]J. Pérez-Pellitero, P. Ungerer, G. Orkoulas, and A. D. Mackie, “Critical point estimation of the lennard-jones pure fluid and binary mixtures”, The Journal of Chemical Physics **125**, 054515 (2006).

[337]S. Artemenko, T. Lozovsky, and V. Mazur, “Critical lines in binary mixtures of components with multiple critical points”, in Metastable systems under pressure, edited by S. Rzoska, A. Drozd-Rzoska, and V. Mazur (2010), pp. 217–232.

[338]T. Yamamoto and M. Matsumoto, “Solute effects on supercritical fluid”, Molecular Simulation **37**, 1091–1096 (2011).

[339]I. H. Bell and A. Jäger, “Calculation of critical points from helmholtz-energy-explicit mixture models”, Fluid Phase Equilibria **433**, 159–173 (2017).

[340]M. Meyer and H. E. Stanley, “Liquid–liquid phase transition in confined water: a monte carlo study”, The Journal of Physical Chemistry B **103**, 9728–9730 (1999).

[341]C. E. Bertrand, Y. Zhang, and S.-H. Chen, “Deeply-cooled water under strong confinement: neutron scattering investigations and the liquid–liquid critical point hypothesis”, Phys. Chem. Chem. Phys. **15**, 721–745 (2013).

[342]L. Xu and V. Molinero, “Is there a liquid–liquid transition in confined water?”, The Journal of Physical Chemistry B **115**, PMID: 21923129, 14210–14216 (2011).

[343]L. B. Krott, J. R. Bordin, N. M. Barraz, and M. C. Barbosa, “Effects of confinement on anomalies and phase transitions of core-softened fluids”, The Journal of Chemical Physics **142**, 134502 (2015).

[344]D. G. Archer and R. W. Carter, “Thermodynamic properties of the nacl + h2o system. 4. heat capacities of h2o and nacl(aq) in cold-stable and supercooled states”, The Journal of Physical Chemistry B **104**, 8563–8584 (2000).

[345]R. W. Carter and D. G. Archer, “Heat capacity of nano3(aq) in stable and supercooled states. ion association in the supercooled solution”, Phys. Chem. Chem. Phys. **2**, 5138–5145 (2000).

[346]D. Corradini, S. V. Buldyrev, P. Gallo, and H. E. Stanley, “Effect of hydrophobic solutes on the liquid-liquid critical point”, Phys. Rev. E **81**, 061504 (2010).

[347]D. Corradini, P. Gallo, S. Buldyrev, and H. Stanley, “Liquid-liquid critical point of mixtures of jagla ramp potential particles and hard spheres”, Proceedings of the International School of Physics "Enrico Fermi" **176**, 393–397 (2012).

[348]D. Corradini, Z. Su, H. E. Stanley, and P. Gallo, “A molecular dynamics study of the equation of state and the structure of supercooled aqueous solutions of methanol”, The Journal of Chemical Physics **137**, 184503 (2012).

[349]P. Kumar, Z. Yan, L. Xu, M. G. Mazza, S. V. Buldyrev, S.-H. Chen, S. Sastry, and H. E. Stanley, “Glass transition in biomolecules and the liquid-liquid critical point of water”, Phys. Rev. Lett. **97**, 177802 (2006).

[350]J. Bachler, P. H. Handle, N. Giovambattista, and T. Loerting, “Glass polymorphism and liquid-liquid phase transition in aqueous solutions: experiments and computer simulations”, Phys. Chem. Chem. Phys. **21**, 23238–23268 (2019).

[351]D. Corradini and P. Gallo, “Liquid–liquid coexistence in nacl aqueous solutions: a simulation study of concentration effects”, The Journal of Physical Chemistry B **115**, PMID: 21851078, 14161–14166 (2011).

[352]A. P. Furlan, C. E. Fiore, and M. C. Barbosa, “Influence of disordered porous media on the anomalous properties of a simple water model”, Phys. Rev. E **92**, 032404 (2015).

[353]D. González-Salgado, J. Troncoso, and E. Lomba, “The temperature of maximum density for amino acid aqueous solutions. an experimental and molecular dynamics study”, Fluid Phase Equilibria, 112703 (2020).

[354]J. Troncoso, D. González-Salgado, and L. Romaní, “Temperature of maximum density for binary aqueous solutions of five amino acids”, Journal of Chemical & Engineering Data **64**, 5847–5856 (2019).

[355]J. Troncoso, D. González-Salgado, and L. Romaní, “Temperature of maximum density of proteins in water: α-chymotrypsin and bovine serum albumin”, The Journal of Chemical Thermodynamics **142**, 106008 (2020).

[356] D. Mallamace, S.-H. Chen, C. Corsaro, E. Fazio, F. Mallamace, and H. E. Stanley, “Hydrophilic and hydrophobic competition in water-methanol solutions”, Sci. China Phys. Mech. Astron **62**, 107003 (2019).

[357] D. González-Salgado and I. Nezbeda, “Excess properties of aqueous mixtures of methanol: simulation versus experiment”, Fluid Phase Equilibria **240**, 161–166 (2006).

[358] G. Pálinkás, E. Hawlicka, and K. Heinzinger, “Molecular dynamics simulations of water-methanol mixtures”, Chemical Physics **158**, 65–76 (1991).

[359] M. Martínez-Jiménez and H. Saint-Martin, “A four-site molecular model for simulations of liquid methanol and water–methanol mixtures: meoh-4p”, Journal of Chemical Theory and Computation **14**, PMID: 29566336, 2526–2537 (2018).

[360] M. C. Sanchez, H. Dominguez, and O. Pizio, “Molecular dynamics simulations of the properties of water-methanol mixtures. effects of force fields”, Condensed Matter Physics **22**, 13602 (2019).

[361] M. A. Barbosa, E. Salcedo, and M. C. Barbosa, “Multiple liquid-liquid critical points and density anomaly in core-softened potentials”, Phys. Rev. E **87**, 032303 (2013).

[362] M. Huš, G. Munaò, and T. Urbic, “Properties of a soft-core model of methanol: an integral equation theory and computer simulation study”, The Journal of Chemical Physics **141**, 164505 (2014).

[363] G. Munaò and T. Urbic, “Structure and thermodynamics of core-softened models for alcohols”, The Journal of Chemical Physics **142**, 214508 (2015).

[364] M. Huš, G. Žakelj, and T. Urbič, “Properties of methanol-water mixtures in a coarse-grained model”, Acta Chimica Slovenica **62**, 524–530 (2015).

[365] J. R. Bordin, L. B. Krott, and M. C. Barbosa, “Self-assembly and water-like anomalies in janus nanoparticles”, Langmuir **31**, PMID: 26190234, 8577–8582 (2015).

[366] J. R. Bordin, “Waterlike features, liquid–crystal phase and self-assembly in janus dumbbells”, Physica A: Statistical Mechanics and its Applications **459**, 1–8 (2016).

[367]M. Hus and T. Urbic, "Existence of a liquid-liquid phase transition in methanol", Phys. Rev. E **90**, 062306 (2014).

[368]C. Desgranges and J. Delhommelle, "Communication: existence and control of liquid polymorphism in methanol under shear", The Journal of Chemical Physics **149**, 111101 (2018).

[369]M. S. Marques, V. F. Hernandes, E. Lomba, and J. R. Bordin, "Competing interactions near the liquid-liquid phase transition of core-softened water/methanol mixtures", Journal of Molecular Liquids **320**, 114420 (2020).

[370]G. Munaò and T. Urbic, "Structure and thermodynamics of core-softened models for alcohols", The Journal of Chemical Physics **142**, 214508 (2015).

[371]G. Franzese, "Differences between discontinuous and continuous soft-core attractive potentials: the appearance of density anomaly", Journal of Molecular Liquids **136**, EMLG/JMLG 2006, 267–273 (2007).

[372]A. B. de Oliveira, G. Franzese, P. A. Netz, and M. C. Barbosa, "Waterlike hierarchy of anomalies in a continuous spherical shouldered potential", The Journal of Chemical Physics **128**, 064901 (2008).

[373]A. Kolb and B. Dünweg, "Optimized constant pressure stochastic dynamics", The Journal of Chemical Physics **111**, 4453–4459 (1999).

[374]H. Limbach, A. Arnold, B. Mann, and C. Holm, "Espresso—an extensible simulation package for research on soft matter systems", Computer Physics Communications **174**, 704–727 (2006).

[375]A. Arnold, O. Lenz, S. Kesselheim, R. Weeber, F. Fahrenberger, D. Roehm, P. Košovan, and C. Holm, "Espresso 3.1: molecular dynamics software for coarse-grained models", in Meshfree methods for partial differential equations vi, edited by M. Griebel and M. A. Schweitzer (2013), pp. 1–23.

[376]M. Tuckerman, *Statistical mechanics: theory and molecular simulation*, Oxford graduate texts (Oxford University Press, 2010).

[377] J. R. Errington and P. D. Debenedetti, "Relationship between structural order and the anomalies of liquid water", Nature (London) **409**, 318 (2001).

[378] M. Dzugutov, "Universal scaling law for atomic diffusion in condensed matter", Nature **381**, 137–139 (1996).

[379] J. C. Dyre, "Perspective: excess-entropy scaling", The Journal of Chemical Physics **149**, 210901 (2018).

[380] I. Bell, J. Dyre, and T. Ingebrigtsen, "Excess-entropy scaling in supercooled binary mixtures", English, Nature Communications **2020**, `10.1038/s41467-020-17948-1` (2020).

[381] G. Galliero, C. Boned, and J. Fernández, "Scaling of the viscosity of the lennard-jones chain fluid model, argon, and some normal alkanes", The Journal of Chemical Physics **134**, 064505 (2011).

[382] H. J. Raveché, "Entropy and molecular correlation functions in open systems. i. derivation", The Journal of Chemical Physics **55**, 2242–2250 (1971).

[383] A. Baranyai and D. J. Evans, "Direct entropy calculation from computer simulation of liquids", Phys. Rev. A **40**, 3817–3822 (1989).

[384] R. Sharma, S. N. Chakraborty, and C. Chakravarty, "Entropy, diffusivity, and structural order in liquids with waterlike anomalies", The Journal of Chemical Physics **125**, 204501 (2006).

[385] P. J. Steinhardt, D. R. Nelson, and M. Ronchetti, "Bond-orientational order in liquids and glasses", Phys. Rev. B **28**, 784–805 (1983).

[386] A. B. de Oliveira, P. A. Netz, T. Colla, and M. C. Barbosa, "Structural anomalies for a three dimensional isotropic core-softened potential", The Journal of Chemical Physics **125**, 124503 (2006).

[387] Z. Yan, S. V. Buldyrev, N. Giovambattista, and H. E. Stanley, "Structural order for one-scale and two-scale potentials", Phys. Rev. Lett. **95**, 130604 (2005).

[388]V. Ramasubramani, B. D. Dice, E. S. Harper, M. P. Spellings, J. A. Anderson, and S. C. Glotzer, "Freud: a software suite for high throughput analysis of particle simulation data", Computer Physics Communications **254**, 107275 (2020).

[389]C. H. Rycroft, "Voro++: a three-dimensional voronoi cell library in c++", Chaos: An Interdisciplinary Journal of Nonlinear Science **19**, 041111 (2009).

[390]P. M. Larsen, S. Schmidt, and J. Schiøtz, "Robust structural identification via polyhedral template matching", Modelling and Simulation in Materials Science and Engineering **24**, 055007 (2016).

[391]A. Stukowski, "Visualization and analysis of atomistic simulation data with ovito-the open visualization tool", MODELLING AND SIMULATION IN MATERIALS SCIENCE AND ENGINEERING **18**, `10.1088/0965-0393/18/1/015012` (2010).

[392]E. Salcedo, N. M. Barraz, and M. C. Barbosa, "Relation between occupation in the first coordination shells and widom line in core-softened potentials", The Journal of Chemical Physics **138**, 164502 (2013).

[393]A. B. de Oliveira, P. Netz, and M. C. Barbosa, "An ubiquitous mechanism for water-like anomalies", Europhys. Lett. **85**, 36001 (2009).

[394]P. Vilaseca and G. Franzese, "Softness dependence of the anomalies for the continuous shouldered well potential", The Journal of Chemical Physics **133**, 084507 (2010).

[395]P. Vilaseca and G. Franzese, "Isotropic soft-core potentials with two characteristic length scales and anomalous behaviour", Journal of Non-Crystalline Solids **357**, 419–426 (2011).

[396]M. Huš and T. Urbic, "Core-softened fluids as a model for water and the hydrophobic effect", The Journal of Chemical Physics **139**, 114504 (2013).

[397]M. S. Marques, T. P. O. Nogueira, R. F. Dillenburg, M. C. Barbosa, and J. R. Bordin, "Waterlike anomalies in hard core–soft shell nanoparticles using an effective potential approach: pinned vs adsorbed polymers", Journal of Applied Physics **127**, 054701 (2020).

[398]F. Mallamace, “The liquid water polymorphism”, Proceedings of the National Academy of Sciences **106**, 15097–15098 (2009).